IN 34
40366
P. 123

A Laser Velocimeter Investigation of the Normal Shock-Wave Boundary Layer Interaction

Randall M. Chriss
Lewis Research Center
Cleveland, Ohio

September 1991

NASA

A LASER VELOCIMETER INVESTIGATION OF THE NORMAL SHOCK-WAVE BOUNDARY LAYER INTERACTION

Randall M. Chriss
National Aeronautics and Space Administration
Lewis Research Center
Cleveland, Ohio 44135

Abstract

Non-intrusive three-dimensional measurements have been made of a normal shock wave/turbulent boundary layer interaction. The measurements were made throughout a quadrant of a square test section of a continuous flow supersonic wind tunnel in which a normal shock wave had been stabilized. Two-dimensional measurements were made throughout the interaction region while three-dimensional measurements were made near the corner in the vicinity of the shock where three-dimensional flow effects were expected to be significant.

Laser Doppler velocimetry, surface static pressure measurements and flow visualization techniques were employed for two freestream nominal Mach number test cases: 1.6 and 1.3. No turbulence information was obtained. The mean velocity measurements were converted to Mach number by recording the wind tunnel total temperature.

Some shock oscillation was present during both of the test cases. After startup of the wind tunnel the shock oscillated with an amplitude of approximately ± 1 cm, however, after reaching steady condition the shock oscillation amplitude was greatly reduced, as evidenced by the laser velocimeter results.

The Mach 1.3 test case resulted in a nearly uniform flow without secondary shock waves and with no or very isolated corner separation. The Mach 1.6 test case contained separated flow regions and a system of secondary shock waves. The reported results are believed to accurately describe the flowfield of each case and may find use in the verification of numerical simulations.

Contents

List of Figures

Chapter 1

Introduction

1.1 Overview

The normal shock wave/turbulent boundary layer interaction is found in a wide range of aerodynamic situations. The interaction occurs in both internal and external flows. External interactions can occur in transonic flows over airfoils. Internal interactions occur within turbomachinery as well as in supersonic inlet systems and nozzles. The present investigation is relative to the latter application.

The term shock wave/boundary layer interaction arises from the fact that the subsonic part of the boundary layer is not capable of supporting the step change in pressure associated with a normal shock. Therefore, the increase in pressure must be propagated upstream through the boundary layer. This pressure rise causes the boundary layer to thicken which in turn forces changes in the freestream and hence shock structure. This continuous adjustment of the boundary layer to the freestream and vice versa is termed the shock/boundary layer interaction.

The shock wave/boundary layer interaction in an enclosed duct is of great interest to designers of inlet systems since this phenomena can greatly effect the flowfield downstream of the interaction. The large pressure gradients associated with shock wave/boundary layer interactions have the potential of producing large regions of separated flow. These in turn can cause a substantial degradation of engine performance. Consequently, to design improved high-speed inlets in which normal shocks occur a thorough understanding of the flow physics and the capability to compute

the interaction is necessary. This is made more difficult by the fact that in internal flow applications with the exception of purely axisymmetric flows normal shock wave/boundary layer interactions are three-dimensional.

Aerodynamicists have until recently restricted themselves to flowfields which were thought to be two-dimensional in order to gain an understanding of the fundamental flow physics. This is especially true in regards to computer code validation experiments since the ability to calculate complex three-dimensional flowfields has only recently become feasible.

In most instances, however, normal shock wave/boundary layer experiments were performed in rectangular wind tunnels where sidewall boundary layers were present. In an effort to obtain two-dimensional data the researchers restricted their measurements to the wind tunnel mid-span. However, the effect of the sidewall boundary layers on these flows has probably been greatly underestimated. This was experimentally demonstrated by Lewis [1] in a two-dimensional compression corner and has been reiterated by Rose [2] and many others. This misjudgement has resulted in misunderstanding and confusion relative to the flow physics associated with these flowfields. Moreover, much of the existing data was obtained with pitot pressure probes. The sensitivity of the normal shock to these intrusive measurement techniques has limited the progress in the study of these flows.

In this investigation a normal shock wave was stabilized in a square wind tunnel test section and was allowed to freely interact with the naturally ocurring wind tunnel boundary layers. The emphasis was in making three-dimensional velocity measurements in the corner of the test section in order to determine the flowfield associated with the interaction.

It is well known that a normal shock located in a duct of constant cross sectional area is inherently unstable. Any disturbance in the post shock region of the flowfield will cause large fluctuations in the position of the shock wave. For this reason, the use of pitot tubes, with their accompanying array of actuators, was ruled out as a means of surveying the flowfield. However, Seddon [3] successfully employed an arrangement that involved moving a normal shock wave back and forth over a stationary pitot static tube, but this technique is intrusive and is inefficient as a means of obtaining a large amount of data. Accordingly, it was decided that a laser

velocimeter would provide a better means of obtaining the velocity data.

Two-dimensional measurements (of u and v) were made throughout the flowfield. The third component (w) was measured only in the corner near the shock, where it was expected to be significant, and consequently, where the uncertainty in w was expected to be small.

The results are presented in the form of local Mach number due to the fact that the total temperature could vary considerably from run to run depending on which set of air handlers were used to provide the air. This determination is made on a laboratory wide basis and so is beyond control of the reseacher.

Two separate test cases were examined during this investigation, one at a freestream Mach number of 1.3 and the other at a Mach number of 1.6. During both of these investigations the unit Reynolds number was maintained at 15×10^6/meter. The reason these Mach numbers were selected was because two entirely different flow structures were known to exist for two-dimensional flows. The Mach 1.3 flow was known to be near the onset of separation. The Mach 1.6 flow is known to definitely result in boundary layer separation. The strategy for this experiment was therefore to study the flowfield at these two Mach numbers in order to develop an improved understanding of normal shock wave/boundary layer interaction flow physics and to provide data for assessment of numerical simulations.

1.2   Literature Survey

Initial interest in the shock wave/boundary layer interaction arose in the mid 1940's when aircraft were first capable of high subsonic speeds. Evidence of compressibility effects were first noticed by WWII Hurricane and Spitfire pilots who upon putting their planes into steep power dives reported unexpectedly heavy noses and large forces on their control sticks. Soon after WWII rocket propelled experimental aircraft were employed to explore the "sound barrier." It was found that these aircraft became unstable near sonic speeds. Pilots reported severe vibration and violent jerking of the control column followed by buffeting and general instability. These symptoms were found to be caused by shock waves standing at various locations on the aircraft, most importantly the wings. The shock wave greatly disturbed the

flowfield over the wing (including the control surfaces) and therefore tended to cause the loss of control of the aircraft.

Initially the interest in the shock wave/boundary layer interaction was limited to external flowfields, due to airplane pilot encounters with transonic flow. Later, with the advent of the jet engine, interest arose in these interactions within ducts. The following summarizes the history of the interest in the interaction and outlines much of the previous experimental work concerned with the interaction and its effects.

The first significant investigations of the shock wave/boundary layer interaction were performed on curved surfaces to simulate airfoils. Studies by Liepmann [6], Ackeret, et al., [7], Gadd, et al., [8] and Gadd [9] showed that the shock wave pattern and pressure distribution depend greatly on whether the boundary layer is laminar, turbulent or transitional.

Chapman, et al., [10] developed the concept of the free interaction which states that for any upstream Mach number, regardless of downstream pressure, the upstream pressure rise is virtually identical prior to the appearance of the second shock. This was found to be true for oblique as well as normal shocks and is true for a great number and variety of geometries. This was an important advance because it illuminated how upstream influence is propagated through the boundary layer. In addition, Chapman, et al., found that except near the foot of the shock the pressure gradient across the boundary layer is small.

In the early 1950's supersonic aircraft equipped with jet engines were in production. It was at this time that interest in the interaction in enclosed ducts arose. Seddon [3] provided the first significant study of the interaction over a flat surface. This study was very thorough and included vertical as well as horizontal scaling of the interaction. The experiment was performed at a Mach number of 1.47 in a 25.4 cm by 10.16 cm wind tunnel and included two experimental configurations. These were called the "basic" and "modified" interactions. The modified interaction involved stabilizing the shock at the leading edge of a shock generator plate parallel to the flow. The basic interaction used the generator merely as a blockage so as to cause the shock to stand upstream of the generator. The data included schlieren photographs, wall surface static pressures, total pressure traverses as well as two static pressure traverses. The surveys were obtained by moving the shock

wave past probes fixed in the tunnel. This would cause distortions in the data since the incoming boundary layer thickness at the shock would then change from data point to data point. In addition, Seddon tripped his boundary layers to ensure that they were turbulent. The length Reynolds numbers (based on shock location) varied between 1.3×10^6 and 3×10^6. Seddon's data revealed that the flowfield could be scaled both vertically and horizontally to the size of the incoming boundary layer. Both Mach number contours and velocity profiles were derived throughout the interaction region and through the boundary layer. Seddon's benchmark model of the normal shock wave/boundary layer interaction is shown in Fig. 1.

Green [11] in 1970 provided an important work summarizing and discussing all work up to that time which was available in the open literature for all types of interactions, including oblique and normal shocks. Since Seddon's work at least seven experimental investigations of the normal shock wave/boundary layer interaction have been performed. These studies are summarized in the following:

Using a Ludwieg tube, Vidal, et al., [12] simulated the interaction on an airfoil by imposing an airfoil pressure distribution on a flat plate. They sought to investigate the influence of Reynolds number on normal shock boundary layer interactions since some flight test experimental data differed greatly from wind tunnel tests, e.g., Loving [13]. They investigated the interaction at a Mach number of 1.4 for Reynolds numbers of 9×10^6 and 36×10^6 based on shock location. Their data is composed of high speed schlieren motion pictures' wall static pressure taps, skin friction data, and total and static pressure traverses through the boundary layer.

It was found that both the surface pressure and skin friction data showed large changes with Reynolds number. The data indicates that at the higher Reynolds number the bulk of the compression takes place one boundary layer thickness upstream of the shock whereas at the lower Reynolds number the compression is more gradual. The skin friction data showed that the extent of the separated region decreases greatly with increasing Reynolds number. In addition, the height of the bifurcation decreased markedly with increasing Reynolds number.

Leblanc and Goethals [14] utilized two blow-down rectangular tunnels in conjunction with three shock generator configurations in order to stabilize a normal

shock. Their intent was to affirm the findings of Seddon and to determine the usefulness of the results in analyzing the flow in transonic turbomachinery. The tests were conducted at Mach numbers of 1.43 and 1.75. The qualitative data consisted of schlieren photographs and surface oil flow visualization photographs. Quantitative data consisted of wall static pressure measurements as well as static and total pressure surveys through the boundary layer. Mach number profiles were calculated from this data. They used boundary layer bleed to vary the incoming boundary layer thickness in an attempt to stabilize the interaction. In addition, they used boundary layer suction in the second throat to allow the pressure to recover to the value predicted by inviscid flow theory. The data collected and results obtained agreed with those of Seddon.

East [15] studied a two-dimensional interaction on a flat plate with a two-component laser anemometer in a test section 915 mm wide by 762 mm high. The purpose of the investigation was to demonstrate the performance of the LV system rather than on the interpretation of the fluid mechanics. The details of the LV system can be found in Abbiss, et al., [16]. East studied interactions at Mach numbers of 1.3, 1.4 and 1.54. The velocity and its direction were measured at approximately 1000 points. Schlieren photographs were taken and Mach number contours were calculated. Attempts were made to make measurements in the separation regions, however, the turbulence level was too high to permit reliable measurements of the mean velocity. The unsteady components reached values in excess of 50% of the mean velocity. Measurements were made to within 1 cm of the floor for the Mach 1.3 and 1.4 test cases and down to 5 mm for the Mach 1.54 case by concentrating the seed in the boundary layer. The stagnation conditions were 25 °C (77 °F) and 67 kPa (9.7 psi) which results in a unit Reynolds number of about 10×10^6 per meter.

Mateer, et al., [17], studied an axisymmetric normal shock boundary layer interaction at a Mach number of 1.5. They noted that scale effects persisted to much higher Reynolds numbers than previously thought and that achieving the right combination of Reynolds number, boundary layer thickness and pressure gradient to simulate true flight conditions would require extensive effort. This need ultimately led to the building of the National Transonic Facility [18]. Mateer, et al., sought

the ability to compute this type of flowfield in order to obviate these efforts. Consequently, close attention was paid to turbulent fluctuation measurements using hot wire anemometry in order to guide the development of turbulence models.

Their data is composed of hot-wire surveys of both the mean and fluctuating flow along with wall shear, wall pressure and total temperature surveys. The extent of boundary layer separation and reattachment was determined by the embedded hot-wire technique.

The facility was operated in a blow-down mode where the total pressure varied between 0.35 and 2.7 atm so that the Reynolds number varied from 1.93×10^5 to 1.02×10^6 based on boundary layer thickness (10×10^6 to 80×10^6 based on shock location). Mateer and his co-workers found large increases in turbulent shear, lateral velocity fluctuations and longitudinal mass flux fluctuations through the interaction with a subsequent decay of these quantities to downstream values that were higher than the corresponding upstream values. When comparisons were made with previous experimental results they concluded that above Mach 1.4 an embedded region of supersonic flow appears downstream of the shock wave.

In addition, they found that the length of the separation zone scaled to the upstream boundary layer thickness. They note that separation length was found to be much larger in the experiment than reported previously and that this is probably due to the intrusive techniques that were used previously. Further, they concluded that this may call into question previously reported results concerning separation scaling.

Mateer and Viegas [19, 20] continued to investigate the interaction in the same facility as Mateer, et al., [17] in order to determine the effects of Mach and Reynolds numbers on the flow stucture. They experimented in a test section in which a Mach number gradient existed in the axial direction. The tests were performed at Mach numbers from 1.32 to 1.48 and for Reynolds numbers from 8.5×10^6 to 225×10^6 based on shock location.

The data consisted of wall static pressures and skin friction measurements using the embedded hot-wire technique. No separation was detected in this experiment which is thought to be due to the wind tunnel wall confinement associated with axisymmetric facilities. i.e., the absence of three-dimensional relief.

As Mach number increased there was a reduction in the pressure gradient at the shock and an increase in the downstream pressure ratio. Further increase in Mach number caused a decrease in the minimum value of skin friction and a movement of this minimum downstream. In addition, they found that increasing Reynolds number steepened the pressure gradient at the shock and reduced the downstream pressure ratio. The initial increase in Reynolds number caused a jump in skin friction throughout the interaction while further increase in Reynolds number had little effect on skin friction.

Kooi [21] studied the interaction on a flat plate at a Reynolds number of 2×10^4 based on momentum thickness (18×10^6 based on shock location) and at Mach numbers 1.4, 1.44 and 1.46. This data included wall static pressures, and detailed pitot and static pressure surveys. The integral boundary layer quantities were calculated and skin friction was derived from velocity profiles using Clauser plots. It was found that increasing the Mach number caused rapid growth of the separation bubble along with development of the supersonic tongue. Comparison with other data suggested that Reynolds number has a pronounced effect on separation bubble length.

Om, et al., [22], performed experiments in an axisymmetric facility at freestream Mach numbers of 1.28, 1.37 and 1.48 with a unit Reynolds number of 4.92×10^6/meter. Measurements were also obtained at a Mach number of 1.29 and a Reynolds number of 9.84×10^6/meter. The purpose of this work was to understand the effects of wall confinement on the interaction. Many of the effects were numerically predicted prior to performing the experiment.

Om, et al., found that the interaction depends strongly on Mach number and that the effect of Reynolds number on the flow structure is small. In addition, it was found that the wall confinement present in axisymmetric facilities produces a weaker interaction and a much larger supersonic tongue than is found in planar two-dimensional flows. Wall confinement reduced the downstream pressure and reduces the extent of separation in addition to reducing the maximum buildup of displacement thickness.

Delery [23] studied the interaction in a rectangular test section at Mach numbers of 1.30, 1.45 and 1.37 corresponding to three different flow configurations: incipient

shock induced separation, separated and extensively separated. He sought to investigate the turbulence in the flowfield in order to obtain more accurate turbulence models for use in numerically solving the Navier-Stokes equations. The data obtained consists of mean velocity and Reynolds stress tensor components in addition to turbulent kinetic energy profiles obtained with a two-component laser velocimeter.

The results indicate that turbulence is produced at the beginning of the interaction where the largest decelerations take place and that this turbulence principally affects the streamwise component. Upon separation the flow initially exhibits strong anisotropy, with the streamwise fluctuations larger than the spanwise fluctuations by a factor of three. This anisotropy diminishes downstream so that the normal stress terms in the momentum and turbulence energy equations should not be omitted in the vicinity of the shock. Therefore only turbulence models which rely on one or more transport equations will be required to correctly model the dissipative layer behavior. Care must be taken in order to model the first stage of the interaction in order to obtain accurate predictions of all the Reynolds stresses.

Sajben, et al., [24] and Morris, et al., [25] have studied the two-dimensional normal shock/boundary layer interaction with boundary conditions intended to simulate closely conditions found in inlets. The latter paper studied the interaction with an adverse pressure gradient behind the normal shock while the former paper investigated the interaction with and without boundary layer bleed. A two-component LV system was used to measure the time averaged velocity in addition to obtaining turbulence information.

Two other very recent references that are not yet translated for review are the works of Lian and Jiang [26] and Velichko and Lifshits [27].

Chapter 2

The Laser Velocimeter

2.1 Introduction

Laser velocimetry (LV) is a non-intrusive optical technique for the measurement of instantaneous velocity at a point in a flowfield. The concept of the laser velocimeter was first applied by Yeh and Cummins [28] in 1964 to survey fully developed flow of water in pipes. Measurements were made by observing the Doppler shift in the frequency of laser light scattered by small particles embedded in the flow. Since that time the laser velocimeter technique has matured greatly, taking advantage of other optical arrangements that are much easier to use. In addition, advances in electronic instrumentation have been steadily incorporated into laser velocimeter design.

Laser velocimetry is attractive to aeronautical researchers due to its non-intrusive nature. It is widely used in flowfields where mechanical probes would disturb the flow or where a probe could not survive. In addition, there is no dependence on flowfield pressure, temperature or density, unlike the hot wire anemometer so that no calibration or drift problems exist. In fact under normal circumstances no calibration is necessary in order to obtain measurements with small levels of uncertainty.

The laser velocimeter has been widely used to study turbulent and unsteady flows due to its fast response time. Although it does not have the high frequency response of the hot wire anemometer, valuable turbulence information can be obtained if care is taken. In addition, measurements can be made over a very wide range of velocities: from creeping to supersonic flows.

Several types of laser velocimeters are currently in use. Among them are: reference beam laser-Doppler velocimeters; laser fringe (or dual beam) velocimeters; Fabry-Perot Interferometers; and two-spot velocimeters. Of these the fringe and two spot velocimeters are by far the most common. In the following, the basic phenomena behind the laser velocimeter is presented along with the various optical arrangements of velocimeters.

The Doppler effect is widely used by astronomers to detect the relative motion between the Earth and celestial light sources. "Blue" shifted and "red" shifted sources indicate whether a source is moving toward or away from the Earth. This same phenomena is used in laser Doppler velocimetry. The light scattering particles play the part of the Earth bound observers in that they reflect in all directions the light that they "see." This scattered light is either up shifted or down shifted depending on the relative motion between the particle and the source.

In theory the frequency of shifted light could be detected directly and hence the relative velocity between the particle and source deduced if the wavelength of the laser light is known. However, the frequency of this shifted light is too high to be detected by normal means except by a Fabry-Perot interferometer. The arrangement of this device appears to be similar to other optical configurations, however, its operation is quite different. The resolution of this device is typically on the order of 5 MHz which is too large to be useful, except in very high-speed flows where large frequency shifts exist.

In order to use devices that have better frequency resolution the frequency to be measured must be reduced. This is done by *heterodyning* or mixing two high frequency signals which results in a signal with a frequency that is equal to the difference between the original two. Heterodyning is widely used in radio receivers to reduce the frequencies that must be filtered and amplified.

In the reference beam configuration an unshifted beam from the laser is heterodyned at the surface of the photodetector with laser light scattered from a moving particle. The resulting signal has a frequency equal to the Doppler frequency. The configuration of Yeh and Cummins was of this type. Although conceptually simple, this system is difficult to use since it is difficult to align and is not flexible or portable.

2.2   The Fringe or Dual Beam Velocimeter

The fringe type velocimeter (also called the dual beam velocimeter) is the most popular LV optical arrangement and is commercially widely available. In this type of velocimeter, two laser beams are crossed to produce a "probe volume" at which point the measurements are made. This volume is an ellipsoid when the incoming beams have a circular cross section. As particles pass through the probe volume they scatter light which is collected and focussed onto a photodetector. This photodetector produces an electronic signal which contains the Doppler frequency of the particles. The physical phenomena which gives rise to fringe system measurements can be thought of in two ways, both of which give the same answer mathematically. In the following, the two ways of describing the fringe anemometer are presented, the first is simpler and easier to visualize, the second is more rigorous mathematically.

In the probe volume, i.e., where the two beams overlap, light and dark bands are produced due to the constructive and destructive interference that occurs between the two coherent beams. The fringes are parallel to the optical axis and perpendicular to the plane containing the two beams. As a particle traverses the fringes, sinusoidal pulses of light are emitted in all directions. These sinusoidal pulses have the same frequency as the Doppler frequency. This light is then collected and focussed onto a photodetector to produce an electronic signal which contains the Doppler signal. These fringes are physically present in the probe volume and can be seen if a cross section of the probe volume is magnified and projected on to a screen.

A more rigorous way to describe this arrangement is to consider the interaction of the particle with each of the two beams separately. As a particle traverses the probe volume the scattered light from one beam is mixed with the scattered light from the other beam. The resulting frequency is the Doppler frequency and is not dependent on the position of the observer. In this arrangement the light is said to be heterodyned, not at the photodetector aperture as in the reference beam configuration, but at the point where the light is scattered, i.e., on the surface of the particle.

Since the two beams can emanate from one lens and cross at a probe volume which is easy to locate in a test rig, the fringe velocimeter is very flexible and easy

to align. In addition, large collection aperatures can be used to increase the signal-to-noise ratio since the coherence requirements of the reference beam configuration are not present. For these reasons the fringe type velocimeter is by far the most common system used today.

In fringe type systems the optical setups are classified as either forward scatter or backscatter depending on the location of the receiving optics. If the probe volume is located between the photodetector and the transmitting optics, the setup is called a *forward scatter* arrangement. If the photodetector lies on the same side of the probe volume as the transmitting optics, the system is said to be in *backscatter*. Each of these arrangements has its own set of advantages and disadvantages so that the system is chosen to fit each particular experiment. Backscatter must be used in experiments where optical access to both sides of the facility may be limited, which is common in turbomachinery applications. Forward scatter yields a much higher signal-to-noise ratio and so yields measurements more readily than backscatter systems. However, mechanical and optical access to both sides of a facility is required which is often difficult in large facilities. The advantage of forward scatter over backscatter is due to the fact that the scattered light is typically two to three orders of magnitude more intense forward of the probe volume than behind it since it is easier to deflect photons than to reflect them.

The Doppler shift associated with a particle having a velocity, $\vec{v}$, when illuminated by incident light rays having unit vectors $\hat{k}_i$ and $\hat{k}_j$, where λ is the wavelength of the incident light, is given by:

$$f_D = (\hat{k}_i - \hat{k}_j) \cdot \frac{\vec{v}}{\lambda}. \tag{1}$$

Since $| \hat{k}_i - \hat{k}_j | = 2\sin\kappa$, where κ is the half angle between the beams, and $v_a = | \vec{v} | \cos\alpha$, where α is the angle between the velocity vector and the line (call this axis "a") perpendicular to the optical axis and in the plane of the beams, Eq. (1) reduces to:

$$f_D = v_a \frac{2\sin\kappa}{\lambda}. \tag{2}$$

This can be rewritten as

$$v_a = f_D d_f. \tag{3}$$

where d_f is the fringe spacing and given by

$$d_f = \frac{\lambda}{2 \sin \kappa}. \tag{4}$$

Therefore when the Doppler frequency is known along with the geometrical layout of the LV system, a velocity component can be determined.

2.3 The Two Spot Velocimeter

Another type of laser velocimeter that is widely used is the two-spot velocimeter which has been given several names: the laser transit anemometer (LTA), the time-of-flight (TOF) anemometer, and the laser two focus anemometer (L2F). This technique does not make use of the Doppler effect and so is different in concept and optical layout from the other types of laser velocimeters. There is no crossing of laser beams to obtain fringes, instead, two separate beams are focussed into small beam waists or "spots" so that they lie adjacent to one another. These spots are on the order of 10 μm in diameter. A separate photodetector is trained on each of the spots so that as particulates pass through the spots a train of electronic pulses is generated by each of the photodetectors. Particle speed is then determined in one of two ways: by measuring the transit time of the particle as it travels from one spot to the next or by cross-correlating the two pulse trains. The first approach is discussed by Schodl [29, 30, 31] and the second by Mayo, et al., [32].

The advantage of the two spot velocimeter is that all of the laser power is contained in two variable diameter spots instead of a multitude of fringes so that the intensity in the spots can be two to three orders of magnitude higher than obtainable in a fringe anemometer given equivalent lasers. This results in a theoretical increase in the signal-to-noise ratio.

The effective length of the measurement volume in a two spot system is shorter than in a fringe system which enhances the ability to make measurements near solid surfaces. In addition, the spot intensity can remain high while the spot spacing is variable. These advantages serve to reduce the resolution requirements of the accompanying electronic instrumentation.

The chief disadvantage of the two spot system is that low data rates are obtained

due to the small spot size. This problem increases greatly as the turbulence level increases since the resulting flow angle variations reduce the chance that one particle will pass through both spots. Other disadvantages are that flow reversal cannot be detected and that rotation of the optics is required to align the spots with the flow direction. In addition, the time history of the flow is not obtainable from the data. A more complete discussion can be found in [33].

2.4 Data Acquisition

In Doppler velocimetry the light scattered from particles passing through the probe volume generates individual electronic bursts in the photodetector which are then amplified and transmitted to a signal processor. Several types of processors are available to the laser velocimeter user. Among them are burst correlators, frequency trackers and counter processors. Burst type processors and frequency trackers are limited to a maximum Doppler frequency of about 50 MHz so that their use may be limited in high-speed flows. The output from these processors can be either in digital or analog form; the latter allowing direct storage of data on magnetic tape. In addition, the frequency tracker requires a nearly continuous input signal and so is popular in applications of laser velocimetry to liquid flows where high-seed concentrations can be easily obtained.

The most common type of signal processor is the counter processor. This device measures the elapsed time for a set number of fringe crossings and so has to "count" the number of crossings in the process. This time measurement is made with a high-speed internal clock.

The sensitivity of this type of processor is adjusted by either varying the amplitude of the incoming signal when the processor has a fixed threshold or by varying the threshold when the signal strength is fixed. Each particle burst passes through validation circuitry in an effort to filter electronic noise from the Doppler bursts.

The number of realizations required at each measurement location is determined by the experimenter and is usually set in the acquisition software. This is important since it can impact the statistical significance of the data. A discussion of statistical uncertainty is given in Chapter 3.

Individual particle realizations can be stored in a number of ways in LV systems. In order to hasten the acquisition of the large numbers of realizations that are typically required, the data is not passed through the CPU (central processing unit of the computer); instead, the data is either passed directly into computer memory or is stored in special buffers. The data can then be post-processed and analyzed off-line. Direct storage of data into memory can be accomplished with most computer systems with a DMA (direct memory access) interface card.

The data from each measurement point is often presented in the form of a velocity histogram which is a plot of the number of observed occurrences versus velocity. This gives a direct indication of the distribution of the data and is helpful in recognizing erroneous data.

2.5   The Seed Material

As was stated previously, laser-Doppler velocimetry measures the velocity of particles embedded in the flow. In many situations particulates are inherent in the flow that are suitable for LV seed. This is normally true for water unless it has been filtered to eliminate particulates. For gases, however, the flow normally requires artificial seeding to facilitate LV measurements. In many situations this is the most difficult aspect of making LV measurements and therefore, it is often not treated rigorously by investigators using the technique.

Many types of seed material are available to the laser velocimeter user. Liquid materials are often used in wind tunnel tests or in turbomachinery investigations where solid particulates would destroy the bearings, contaminate instrumentation systems or erode models. Some of the most often used liquids are: water, synthetic oils, olive and other natural oils as well as kerosene. Disadvantages in using these liquids include the fact that some of them will evaporate quickly while the oils tend to accumulate on observation or test section windows which therefore may require frequent cleaning.

Solid particles are required in combusting or high temperature flowfields. Some widely used materials are: titanium dioxide, silicon carbide and aluminum oxide. Polystyrene latex spheres are widely used as a seed material today. They do not

evaporate and are not hard enough to destroy machinery especially when used in the low concentrations required for laser velocimetry. Until recently their cost was prohibitive but Nichols [34] developed an economical means of producing large amounts of the monodisperse seed material.

Some considerations in choosing a seed material/generator combination are: aerodynamic particle size, refractive index of the seed material, degree of monodispersity, toxicity, concentration of seed required and the cost of the seed material. Particle size is described in terms of its aerodynamic diameter which is the true measure of its ability to follow a flowfield. The concept of aerodynamic diameter was first given by Yanta [35] when he built a laser velocimeter to determine particle size by allowing the particles to pass through a large velocity gradient. The aerodynamic diameter is defined as the diameter of a unit density sphere with the same settling velocity as the particle in question. It is a function of density, size and shape of the particle. The smaller the aerodynamic diameter of a particle, the greater its ability to follow the flow.

In general a particle will scatter more light as its refractive index and its diameter increase. However, for a given optical setup the signal may actually decrease with an increase in particle diameter or refractive index. This is due to the complex nature of scattered light which is described by the *Mie theory.*

Since LV systems measure particle velocity, it is critical that these particles follow the flow with integrity. The discrepancy between particle velocity and fluid velocity is not normally significant except in high-speed flows and flows involving shock waves where large velocity gradients are present. In these situations, particle inertia must be taken into account. The seed particles must be small enough and bouyant enough to follow the flow. Detailed accounts can be found in Yanta, et al., [36], Maxwell and Seasholtz [37], Carlson and Hoglund [38], Feller and Meyers [39], and von Stein and Pfeifer [40].

The amount of light a particle will scatter decreases greatly with its diameter and the resulting signal strength from the photodetector is proportional to the intensity of the light that strikes it. Since the signal processing equipment of the LV system requires a certain minimum threshold signal, some minimum error due to particle lag must be accepted. Stated another way: minute particles that would follow the

flow exactly would not produce usable signals. In addition, as particle size increases the associated signal goes up disproportionately so that the data taken by the LV system will be biased toward the largest particles. In practice then, the objective is to seed the flow with the smallest particles that will produce usable signals while making sure to eliminate signals from any large particles.

Meyers and Walsh [41] have written a computer program which will predict the performance of a fringe velocimeter for a range of flow velocities, seed particle sizes and materials, given the optical and electronic characteristics of the velocimeter. Another way to predict laser velocimeter performance is to estimate the system signal-to-noise ratio. A method for accomplishing this has been given by Adrian [42] which is based on the Mie theory of scattered light.

In some wind tunnels naturally occurring particulates are sufficient as seed for LV work, however, these particles were deemed to be too large to be used as LV seed in the current investigation. The data rate obtainable from naturally occurring particles is usually too small to make efficient use of a large facility.

An evaporation-condensation aerosol generator was built for the current investigation due to its capacity to produce large amounts of the monodisperse aerosol desired. This type of generator was first developed by Liu, et al., [43] for aerosol research and has been used successfully in LV work by Yanta [44]. A lengthy discussion of this type of generator can be found in [45] and is given in the next chapter.

2.6 Laser Velocimeter Bias

Several types of bias or error can enter into laser velocimeter measurements which must be carefully considered. Two important parameters that effect bias are the particle concentration and the turbulence level of the flow. A brief description of the various types of bias is given in the following.

Most signal processors require a minimum number of fringe crossings in order to validate a realization. Therefore, in the absence of frequency shifting, the probe volume has some maximum acceptance angle which places a restriction on the acceptable particle trajectory. This restriction results in *fringe bias*, however, frequency shifting can be used to expand this acceptance angle. If the frequency shift

is great enough the acceptance angle can be expanded to include all possible particle trajectories.

Gradient bias is due to the finite size of the probe volume that is inevitable in all laser velocimeters. Because of this, velocity gradients in the flowfield can cause multiple velocities to exist in the probe volume at the same time. Because of the built-in preference of laser velocimeters to measure slower particles over faster particles, bias can result. This is distinguished from other types of bias because of the fact that it can arise in steady flow, i.e., it is not caused by velocity fluctuations.

All fringe velocimeters must filter noise from the incoming electronic signals, but, in so doing, limit the frequency bandwidth of the velocimeter. This would not normally be of concern except in velocimeters whose signal-to-noise ratio is near the limit of the signal processor. In this case the filter settings that will allow valid measurements may restrict the frequency bandwidth to a large degree. In addition, the frequency response characteristics of the photodetection system can cause misleading results. These two effects are grouped together and are called *filter bias*.

Another type of bias arises due to the fact that in general the arrival rate of measureable particles is not statistically independent of the flow velocity. As a result of this, ensemble averaging of the realizations may not result in a true time averaged value of velocity. This error is a function of several parameters which include particle concentration and processor settings. Because this type of bias is normally the most significant and is controversial, it will be discussed in some detail in the following.

In 1973, McLaughlin and Teidermann [46] showed that velocity sampling was not random but was biased due to a greater probability of sensing faster particles than slower particles. This supposition came well after the advent of laser velocimetry and remains controversial; some researchers believing that bias is relevent and some researchers believing that it is not relevent or that it does not exist at all. McLaughlin and Teidermann proposed that this bias could be eliminated by weighting the individual velocity measurements correctly. This takes a general form given by

$$\overline{U}_{corrected} = \frac{\sum_{j=1}^{N} \omega_j U_j}{\sum_{j=1}^{N} \omega_j},$$ (5)

where ω is a weighting function, and N is the total number of realizations in the sample. It was suggested that the measurements could be weighted according to the inverse of the magnitude of the total velocity vector, i.e.,

$$\overline{U}_{corrected} = \frac{\sum_{j=1}^{N} |\vec{V_j}|^{-1} U_j}{\sum_{j=1}^{N} |\vec{V_j}|^{-1}} \tag{6}$$

To correctly implement this equation all three components of velocity are required simultaneously. Since three-component measurements are too difficult and costly to obtain in many instances, they suggested using estimates of the velocity magnitude from one or two component measurements. However, these "corrections" often produced errors much greater than the effects of velocity bias, especially at turbulence levels above 20%. This method of correcting for velocity bias has therefore fallen from favor.

Since the work of McLaughlin and Teidermann much work has been done in this area, however, much debate and misunderstanding still exists. In an effort to clarify the situation, Edwards [47] chaired a special panel to investigate the current understanding of bias which resulted in some consensus as to which correction schemes were useful and where they should be applied. The panel stated that data "rate" in itself has no meaning unless it is compared to the time scale of the turbulence. The more appropriate parameter is called the *data density* and is given by $N_v T_\lambda$, where N_v is the *validation rate* of the signal processor and T_λ is the *Taylor time microscale*. The Taylor time microscale is described as the maximum time over which there is no significant change in the energy of a turbulent eddy. Data density therefore is an indication of how well the laser velocimeter is tracking the flow. Some of the work that has been done in the area of velocity bias correction is discussed in the following.

Barnett and Bentley [48] demonstrated that bias is negligible under very sparse seeding conditions. Under these circumstances the measurements are made from particles from different flow eddies thereby ensuring no statistical bias of the data.

Stevenson, et al., [49], Johnson, et al., [50] and Edwards and Jensen [51] showed that LV systems with finite speed data buffers will generate data without velocity bias as long as the data density is high. This was shown experimentally by Stevenson, et al. [49].

Durao, et al., [52, 53] postulated that since faster moving particles scatter fewer photons and produce weaker signals than slower particles there is an inherent preference in LV systems to measure slower moving particles over faster particles. They have shown experimentally that this effect can either partially or totally eliminate the effects of velocity bias. However, as has been pointed out by Meyers [72], these fewer photons strike the receiver in a proportionately shorter period of time so that the amplitude of the analog signal is unchanged. In fact, Meyers pointed out that depending on the specific application, the signal-to-noise ratio may increase with speed.

Buchave [54] suggested measuring the amount of time the particle resides in the probe volume, in addition to the particle velocity. Using the inverse of the residence time as the weighting function in the McLaughlin-Teidermann correction will give the time averaged velocity. Another method first suggested by Dimotakis [55] is to record the elapsed time between realizations. Then, using a simple trapezoidal fit between the points, the time history of the flow can be reconstructed. These methods will give the correct time history of the flow so long as the data density is great enough to capture the true fluid motion. Variations on this idea have been given by Edwards and Jensen [51] and Adrian and Yao [56], whereby a continuous signal is created by holding the previous measurement in a buffer until a new measurement is obtained. Others have proposed the control of the signal processor which gives similar results [57].

Many researchers have tried to verify experimentally the existence of velocity bias. Unfortunately, the turbulence levels at which velocity bias begins to corrupt laser velocimeter measurements will also impede the accuracy of other measurement techniques such as hot wire anemometry and the pitot tube. This has delayed the experimental verification of velocity bias. However, a few attempts have been made.

Quigley and Teidermann [58] attempted to experimentally verify the existence of bias by measuring the viscous sublayer in a two-dimensional fully developed flow in a water channel. They assumed that the slope of the velocity profile and the wall shear stress could be determined from the streamwise pressure gradient. They used this as their standard for comparing the laser velocimeter measurements and went on to verify the existence of bias. However, Bogard and Teidermann [59] were unable to

reproduce these results. Apparently, the assumption that this was a two-dimensional flowfield was erroneous.

Stevenson, et al., [49] did not compare LV results with another instrument. Instead they made measurements in a two-dimensional flow with a variety of particle arrival rates and and sampling rates. They found that bias error was directly dependent on the method in which the data from the counter processor is sampled. They concluded that unbiased data can be obtained when the sampling rate is much less than the particle arrival rate. In this way the data is sampled at nearly equal time intervals. In addition, they found that the McLaughlin-Teidermann correction was valid below a turbulent intensity of 20%.

The approach of Johnson, et al., [50] was to use a laser velocimeter to produce a standard for comparing other laser velocimeter results. They make the assumption that the results from a laser velocimeter are unbiased when the particle concentration is high enough to ensure that there are always at least several particles in the probe volume at any time. They call this *continuous-wave* (CW) velocimetry as apposed to *individual-realization* (IR) velocimetry. They compared the two techniques by making measurements in a shear layer and concluded that velocity bias does exist and that it is independent of sampling rate. However, they found that bias is only important where the turbulent intensity is above 20% and that below this other types of experimental uncertainty would dominate.

In the following chapter the experimental apparatus and the experimental procedures are given in some detail. In addition, details of the flow visualization investigation, the surface pressure measurements and the LV flowfield surveys are discussed.

Chapter 3

Experimental Apparatus and Techniques

3.1 The Wind Tunnel

All tests were performed at the NASA-Lewis Research Center's 1 foot by 1 foot supersonic wind tunnel located in the Engine Research Building. The tunnel test section has nominal cross-sectional dimensions of 30.5 cm by 30.5 cm (1 ft by 1 ft). This is a continuously operable, open-circuit supersonic facility which is capable of nominal test section Mach numbers of 1.3, 1.6, 2.0, 2.5, 3.0, 3.5 and 4.0. The tunnel is depicted in Fig. 2. The discrete Mach numbers are obtained by installing an appropriate converging-diverging nozzle "block" prior to each test session. The nozzle block contour has been designed to account for boundary layer growth to ensure that uniform flow exists in the test section. In the following the various components of the wind tunnel are briefly discussed.

The tunnel is of a push-pull design where air handling machinery resides both upstream and downstream of the test section. Air is delivered to the plenum at high-pressure by compressors and pulled through the diffuser by exhausters. Various air handlers are used and are shared by several other test cells at the laboratory.

Compressors provide inlet air to the tunnel at a pressure of 379 kPa (55 psia) at an approximate dew point of -28.9°C (-20°F). After passing through control valves the air enters a 1.83 m (6 ft) diameter plenum. The valves set the stagnation

pressure and are controlled by the tunnel operator. The flow then passes through a honeycomb staightener along with several turbulence reducing screens before passing into the converging-diverging nozzle.

The geometry of the nozzle blocks is such that throughout the converging-diverging section, the vertical dimension remains constant at 30.5 cm (1 ft) while the horizontal dimension varies. Therefore, the development and thickness of the boundary layers on the sidewalls will differ from those on the ceiling and floor. This will cause asymmetry to exist in the boundary layer structure around the wind tunnel test section. Alignment problems can be significant between the nozzle and the main test section if care is not taken during the nozzle installation. The nozzle and main test sections are held together hydraulically as are the nozzle block components. The nozzles are 2.24 meters (88 in.) in length.

The test section has a total length of 122 cm (4 ft) which is composed of a forward test section, located in the final 61 cm (2 ft) of the nozzle block, and the main test section. Access to the flowfield is made available at several locations along the facility. These ports are used to mount test models, shock generators, etc., in addition to providing access for various types of instrumentation systems. These ports are available in the forward test section, i.e., the nozzle, the main test section, and the diffuser and allow a wide variety of models, instrumentation and actuation systems to be used without facility modifications.

The main test section measures 66 cm long, 30.5 cm high and 31 cm wide (26 in. × 12 in. × 12.2 in.). The main test section can be rotated 90 degrees about the tunnel centerline in order to allow flexibility in the orientation of the instrumentation relative to the model or flowfield. This flexibility can be especially important when a test program requires the use of one of the naturally occurring tunnel boundary layers, as mentioned, since the boundary layers on the floor and ceiling differ from those on the sidewalls. Schlieren quality windows can be mounted in place of the main test section sidewalls to allow optical access to the entire main test section. Windows can also be installed in the forward test section ports to allow limited optical access to this part of the test section. Plexiglass windows can also be installed.

An external bleed system can be used that will allow suction of the main test section boundary layers. This system can be compartmentalized so that distributed

bleed systems are possible.

The exhausters are capable of lowering the pressure in the test section to approximately 6.9 kPa (1 psia) with no flow in the tunnel. The tunnel total temperature is not controllable and varies between 10 and 26.7°C (50 and 80°F) depending on the outdoor ambient air temperature and which air handlers are in use at the time. The Reynolds number can therefore be controlled only by adjusting the tunnel total pressure. The range of unit Reynolds number achievable (based on a total temperature of 21.1°C (70°F)) is depicted in Fig. 3. The low end of the range depends on the point at which the tunnel unstarts, and, therefore, is very dependent on the size and geometry of the test model.

3.2 Test Setup and Operating Conditions

Plenum (or stagnation) pressure is set by the tunnel operator and is continuously variable to 379 kPa (55 psia). During the Mach 1.6 investigation the plenum pressure was maintained at 103.4 kPa (15.0 psia); during the Mach 1.3 test it was maintained at 97.9 kPa (14.2 psia). This was done in an effort to hold the unit Reynolds number constant throughout both tests although the total temperature was not controllable and varied from 15 to 24°C (60 to 75°F). The unit Reynolds number for the two tests was maintained at 15×10^6 per meter.

The normal shock generator consisted of a 60 degree cone mounted on the centerline of the tunnel downstream of the test section in the diffuser. The tip of the cone was approximately 1.5 meters downstream of the test section. The cone choked the flow in the diffuser thereby preventing the "swallowing" of the normal shock wave that constitutes the "starting" of a supersonic wind tunnel. A supersonic wind tunnel is said to be started when supersonic flow resides in the test section; if subsonic flow resides in the test section the tunnel is said to be unstarted. The cone was mounted on a hydraulic cylinder so that it could be moved fore and aft by remote control from the control room. It was in this manner that the shock location was adjusted. The effective cone size could be adjusted by adding or removing additional "skirts" so that the amount of blockage could be adjusted for each of the two test conditions. The shock location was continuously monitored with static pressure

measurements acquired along the centerline of the tunnel floor.

3.3 Schlieren Photography

A hybrid schlieren system was used to take photographs of each of the test conditions. The system consisted of a video camera/monitor system in conjunction with a 35 mm still camera photographic system. A standard black and white system was used in the preliminary investigation prior to taking laser velocimeter measurements. Later, "color" schlieren photographs were taken. The color system is similar to standard black and white systems except that a color transparency is installed in place of the knife edge. The transparency is composed of thin strips of transparent color plastic such that a tiny straight "rainbow" image is positioned in place of the knife edge. As in a standard black and white system this arrangement is sensitive to density gradients in only one direction depending on the orientation of the transparency.

3.4 Surface Oil Flow Visualization

A surface flow visualization technique was used in a preliminary investigation before the laser velocimeter data was taken. This technique served to demonstrate that symmetry existed in each quadrant of the test section as well as to detect the extent of separation. This, along with the schlieren photographs provided valuable insight into the flow physics.

The technique used involves mixing blue fluorescent dye with heavy oil which is then applied in a very thin coat to the test section walls and floor. The tunnel is then run at test conditions for approximately 15 minutes to allow the flow pattern to form. The tunnel is then quickly shut down and opened up to allow photographs to be taken with a 35 mm camera while using ultraviolet "black" lights to illuminate the test section. The ultraviolet light highlights the fluorescing blue dye and therefore emphasizes the streaks created at the surface by the flowfield. This procedure was repeated several times for each of the test conditions. This procedure required plugging of the static pressure lines in order to prevent contamination of the sensitive pressure measurement system. Therefore, the shock location had to be monitored

visually using a video camera system during the oil flow visualization runs.

3.5   Static Pressure Measurement

The pressure measurement system consisted of a Pressure Systems, Inc. model 780B electronically scanned pressure measurement system together with a Hewlett-Packard model 9245 minicomputer. This system is well suited to large facilities which have high operational costs where increased data rates can reduce run times. Accuracy was maintained by frequent (every twenty minutes) on-line calibrations of all transducers. Calibration ensured accuracy of 0.1%. The pressure measurement modules are capable of measuring up to 1024 pressures at scan rates of up to 20,000 measurements per second. For the present investigation the pressure measurement system measured time smoothed or time averaged values.

The test section floor was instrumented with surface static pressure taps across the span of the tunnel at 72 locations. The first row of static pressure taps were located along the z axis (i.e., x = 0). The static pressure lines were bundled together and routed along the diffuser floor and out of the tunnel through an access port in the diffuser. These access ports exist on either side of the diffuser and are about 0.5 meters downstream of the tunnel test section. These steel static pressure lines were exposed to the flowfield before leaving the diffuser.

The static pressure measurements were used to check that flow symmetry was maintained throughout the investigation. In addition, the static pressure measurements along the centerline were used to monitor and maintain the shock location during the laser velocimeter surveys.

3.6   The Laser Velocimeter

The LV system obtained data in a non-orthogonal coordinate system depicted in Fig. 4. The x-direction is the streamwise direction, the y-direction is the floor-to-ceiling direction, and the z-direction is the sidewall-to-sidewall direction. Velocity components u, v and w lie in the x, y and z directions respectively. The laser velocimeter data was taken along the three directions denoted by v_1, v_2, and v_3. A

single component laser velocimeter was used with the photodetector close to, but not directly on, the optical axis. This is termed an off-axis forward scatter system. This arrangement was used to avoid collecting large amounts of reflected light from the oil buildup on the test section windows that occurred during the lengthy test runs. The oil buildup would over time greatly reduce the signal-to-noise ratio of the LV system. The x and y velocity components (u and v) were obtained by rotating the beams about the optical axis. The z component (w) was obtained by rotating the entire LV system about the y axis, i.e., in the horizontal plane. The LV system had an angle θ of 30° and an angle ϕ of approximately 28°.

The LV system had a fringe spacing of 6.4 μm with a probe volume diameter of 67 μm and length of 1.67 mm. A 350 mm focal length transmitting lens was used with a 600 mm focal length receiving lens. The beam spacing leaving the transmitting lens was approximately 22 mm.

The system was mounted on a computer controlled 4-axis table and the measurements were monitored with a real time graphics display that included velocity histograms. This capability is considered important in maintaining the accuracy of the velocity measurements.

Since the flow in the tunnel was quarter symmetric, as demonstrated in the flow visualization results, the LV measurements were acquired in only one quadrant of the test section. The measurements were performed in the upper half of the test section due to the tendency of the seed oil to deposit on the lower half of the windows much faster than on the upper half. For clarity, however, the measured values are presented in terms of the right hand coordinate system shown in Fig. 5. The flowfield was investigated in detail by surveying along both the axial and cross section planes. Each survey plane contained on the order of 1000 individual measurement locations. The complete set of data for each freestream Mach number contained approximately 10,000 individual velocity measurement locations.

The data rate was normally maintained at 1000 realizations per second. At startup with clean windows, the data rate could be adjusted up to 10,000 realizations per second without affecting the accuracy of the data. During the tests, the windows of the test section gradually became fogged with seed oil. For the Mach 1.6 tests, the tunnel could normally be run from 2 to 4 hours before the windows required

cleaning. For the Mach 1.3 case, the rate of contamination was greatly reduced so that 5 to 8 hour runs were typical.

The LV data acquisition system consisted of a PDP 11/34 Digital computer, a model 1990B TSI, Inc. counter signal processor and an Anorad Corp. 4-axis positioning table. The PDP 11/34 acquired the LV data from the signal processor via a DMA (direct memory access) card which bypasses the CPU (central processing unit) and thereby greatly enhances the speed at which the computer could aquire the LV data. In addition, the computer controlled the probe volume location via the 4-axis traverse table. The probe volume location and LV data were monitored on-line with velocity histograms along with velocity and flow angle plots which were continually updated during the lengthy surveys.

The data were reduced on a VAX 11/750 computer and transferred to a Silicon Graphics, Inc. IRIS workstation to make use of three-dimensional computer graphics software.

3.7   The Aerosol Generator

An evaporation-condensation aerosol generator was built for this investigation due to its capacity to produce large amounts of the monodisperse aerosol desired. This type of generator was first developed by Liu, et al., [43] for aerosol research and has been used successfully in LV work by Yanta [44]. The details of the generator used in this investigation can be found in [45].

Seed particles were injected just downstream of the wind tunnel filters in a mixing region about twenty meters upstream of the plenum chamber. This ensured seeding of the entire test section.

In this type of generator an oil-alcohol mixture is first atomized and then vaporized. Upon vaporization small residue nuclei are created due to inherent impurities in the mixture. The vapor is then slowly cooled whereupon the oil condenses out onto the residue nuclei. This creates a monodisperse aerosol whose mean diameter can be controlled by varying the oil to alcohol concentration. A synthetic oil known as dioctal phthalate (DOP) was selected for use as the seed material due to its low vapor pressure. In this way the evaporation of the oil prior to its reaching the test

section was minimized. The alcohol used was methanol.

In this investigation the concentration of oil to alcohol was maintained at 20% by volume and the oil-alcohol flow rate was maintained at 25 milliliters per minute. A Sonicore 035H ultrasonic nozzle was used to atomize the oil-alcohol mixture. Nitrogen was used as the carrier gas and was supplied at a constant flow rate of approximately 18 liters per minute (0.64 ft^3/minute) through a 6.3 mm (0.25 in.) copper tube at approximately 620 kPag (90 psig). The pressure in the nitrogen line supplying the nozzle was maintained at 450 kPag (65 psig). Heat tape was used to maintain the temperature inside the generator at approximately 175°C (347°F), the corresponding outside temperature of the tube was about 285 °C (545°F).

The aerosol generator was equipped with solenoid valves and thermocouples so that it could be remotely controlled from the tunnel control room at all times. Pressures in the generator were monitored via a video camera/monitor system.

The output of the aerosol generator was measured during a preliminary test and the results of these measurements are presented in the following.

3.8   Aerosol Size Validation

In an effort to validate the LV measurements the size of the seed particles was measured *in situ* during a preliminary investigation. Air samples were collected along the tunnel centerline using a 9.5 mm diameter (3/8 in.) pitot probe. The samples were then passed through a TSI, Inc. Aerodynamic Particle Sizer [60]. The results of these measurements are given in Fig. 6.

Detailed measurements of the particle size used during laser velocimeter testing is critical to the validity and reliablity of the data. This is true in many circumstances where the existence of a problem may not be obvious. An example occurs in the study of shear layers where strong vortices at relatively low speeds may induce centrifugal forces sufficient to force the particles from the vortex core. In a situation such as this the vortex may not even appear in the laser velocimeter data. The question of particle lag is especially important in high-speed gas flows where large velocity gradients may exist in the flowfield.

Figure 6 shows that the particulate concentration with seed added is nearly

two orders of magnitude above that of the background tunnel ambient air. The concentration, with seed particles added, peaked at nearly 400 particles per cm^3. As a check on the efficiency of the LV system, an estimate of the number of realizations per cm^3 can be checked against the aerosol concentration computed. This can be described by

$$c_{real.} = \frac{N_v}{A_{pv} v_a}. \tag{7}$$

where N_v is the actual signal processor validation rate, A_{pv} is the cross sectional area of the probe volume, v_a is the flow velocity component sensed by the laser velocimeter and $c_{real.}$ is the effective concentration of the aerosol.

With a maximum mean velocity of 500 meters per second and a validation rate of 1000 realizations per second along with the probe volume projected area (see Chapter 2), Eq. (7) gives a concentration of 30 realizations per cm^3. With particle concentrations on the order of 400 particles/cm^3, this results in an efficiency under 10%. This is regarded to be efficient when compared to most laser velocimeter systems.

Laser velocimeter measurements obtained near the shock also served as a secondary check of the aerosol distribution. Measurements were obtained by the laser velocimeter near the shock wave as it oscillated back and forth across the probe volume. The histograms from these measurements indicate the velocity distribution. Although they do not indicate particle size distribution, given the assumptions that the data rate is great enough to completely capture the shock motion, and that the shock motion was limited, the strongly bi-modal nature of these histograms does give a "feel" for how well the particles followed the steep velocity gradient at the shock front. Two such histograms are presented in Fig. 7. These results tend to support the results of the Aerodynamic Particle Sizer measurements.

Chapter 4

Experimental Approach and Data Analysis

In this investigation a normal shock wave was stabilized in a square wind tunnel test section and was allowed to freely interact with the naturally occurring tunnel boundary layers. The emphasis was in making non-intrusive three-dimensional measurements in the corner of the test section in order to determine the flowfield associated with the interaction.

Two separate test cases were examined during this investigation, one at a freestream Mach number of 1.3 and the other at a Mach number of 1.6. During both of these investigations the unit Reynolds number was maintained at 15×10^6/meter. The reason these Mach numbers were selected was because two entirely different flow structures were known to exist for two-dimensional flows. The Mach 1.3 flow was known to be near the onset of separation. The Mach 1.6 flow is known to definitely result in boundary layer separation. The strategy for this experiment was therefore to study the flowfield at these two Mach numbers in order to develop an improved understanding of normal shock wave/boundary layer interaction flow physics and to provide data for assessment of numerical simulations.

The information gathered consists of schlieren and surface oil flow visualization photographs and wall static pressure measurements as well as laser velocimeter measurements. The laser velocimeter measurements were limited to only one quadrant of the test section due to flowfield symmetry. This was done in order to maximize

the effectiveness of the measurement effort.

Phenomena considered in this study include: the shock induced strong pressure gradient on the growth of the boundary layer, the existence or extent of any separated flow, and the influence of freestream Mach number on three-dimensionality of the flow. This required detailed measurements of both the magnitude and the direction of the flow through much of the interaction region. In addition, attention was given to the documentation of the upstream and downstream flows in order to provide boundary conditions for numerical simulations. The schlieren and the oil flow visualization photographs were obtained during a preliminary investigation which is described further in the next section.

4.1   The Preliminary Investigation

A preliminary investigation was made in order to assess the qualitative nature of the two flowfields as well as to prepare for the detailed laser velocimeter measurements. Some preliminary laser velocimeter measurements were taken at this time in order to determine if the system worked properly, in addition to obtaining the approximate turbulence levels and maximum flow turning angles which existed for each of the flows. The task, however, was to use the schlieren photographic system to size the blockage cones. This was required due to the sensitivity of the shock to very slight changes in cone diameter.

The blockage cones were mounted on a hydraulic actuation system that allowed fine tuning of the mean shock location, once the proper cone size was determined. In addition to sizing the cones the schlieren photographs were valuable in indicating the shock wave structure as well as the growth of the boundary layer. The schlieren video monitor system also indicated that the normal shock waves in both cases were unsteady at startup, i.e., they oscillated with an amplitude of about ± 1 cm randomly about a mean position. However, the size of the oscillation decreased with time so that the mean location was stable and controllable during the acquisition of the LV data.

After completion of the schlieren investigations, further qualitative tests were conducted using a surface oil flow visualization technique. These investigations

revealed the extent of separation in addition to confirming the existence of symmetry. This was important since it eliminated the need to survey the entire test section.

Because of the massive amount of data that is acquired through the use of a laser velocimeter, great care must be given to the acquisition, handling and processing of this information. Thus, in the following the procedure used to acquire the LV data is presented in detail. In addition, a detailed discussion of the experimental uncertainty and error analysis is provided.

4.2   LV Data Acquisition

Two-dimensional measurements (of u and v) were made throughout the flowfield. The third component (w) was measured only in the corner near the shock, where it was expected to be significant, i.e., where the uncertainty in w could be expected to be small.

The laser velocimeter data was acquired in a non-orthogonal coordinate system which is shown in Fig. 4. A single-component LV system was used so that it had to be rotated into the proper orientation to obtain measurements in each of the three directions, v_1, v_2 and v_3. The LV data was acquired in a two step program. First, the flowfield was surveyed completely to obtain the v_1 and v_2 velocity components. These measurements consisted of 1000 realizations each. The u and v components can be determined from these measurements. Then, using flow angle and turbulence information obtained in these measurements, uncertainty estimates were made to determine where the w component should be measured. This was done to prevent wasted effort in acquiring statistically insignificant measurements of w. A discussion of uncertainty and how it is related to the flow structure will be given shortly.

In the second part of the program, measurements of v_3 were obtained in order to determine w. These measurements consisted of 8000 realizations per ensemble.

For each realization two computer "words" of information were recorded. The first was the time word, which together with the fringe spacing and number of fringes required, determines the speed of the particle. The second word of information was the time-between-data word, which is the elapsed time between the last measurement and current measurement. The time-between-data information can be used

to reconstruct the time history of the flow at that point. This is a standard TSI counter processor configuration [61]. Other configurations are available to the LV user.

The speed information for each measurement was determined by ensemble averaging. The time history information was used only at a few points in the flowfield so as to determine the approximate frequency of the shock oscillations.

The probe volume location and the LV data were monitored on-line with velocity histograms along with velocity and flow angle plots which were continually updated during the lengthy tests.

The data was stored on tape in two formats: the first was the raw data format which consisted of probe position information and tunnel conditions along with the time word and the time-between-data word for each realization; the second format consisted of probe position and tunnel conditions along with a velocity ensemble average and standard deviation information. Each data point was stored as an individual record. This facilitates searching and cataloging of the data during post processing. In this way the data can be searched and plotted by spatial position and is not dependent on when the data was taken. Thus, data can be sorted so that plots could be made easily from data that was taken at different times.

The mean velocity estimate and the estimate of the variance in each measurement direction were computed by ensemble averaging the data which can be expressed as

$$\overline{v_i} = \frac{1}{N} \sum_{j=1}^{N} v_{i,} \quad , i = 1, 2, 3 \tag{8}$$

$$s_i^2 = \frac{1}{N} \sum_{j=1}^{N} (v_{i,} - \overline{v_i})^2 \quad , i = 1, 2, 3. \tag{9}$$

This formulation does not consider the effects of velocity bias since it is strictly valid only when statistical biasing of the data is not present. However, it has been shown [47] that bias is not significant where turbulence levels are below 20% or where the data density (the number of realizations made in each eddy of the flow) is very low. Both of these criterion were met in this study. Therefore bias was not considered in the data reduction.

The local Mach number throughout the entire flowfield was computed from

$$M^2 = \left\{\frac{V}{a_t}\right\}^2 \left\{1 - \frac{\gamma - 1}{2}\left[\frac{V}{a_t}\right]^2\right\}^{-1} \tag{10}$$

where a_t is the speed of sound calculated at the total temperature, V is the total velocity, and γ is ratio of specific heats. This equation is valid for thermally and calorically perfect gases undergoing adiabatic processes.

The post processing was performed on a VAX 11/750. The collated data was then transferred to a Silicon Graphics, Inc. "IRIS" graphics workstation in order to make use of three-dimensional computer graphics software.

4.3 Uncertainty Analysis

After an introduction to the transformation matrix an uncertainty analysis is given which is divided into three parts. In the first, an analysis is made to determine how the uncertainty in each of the LV measurements $(\Delta v_i/v_i)$ propagates into the calculated results. In the second part, an analysis is made to determine $\Delta v_i/v_i$. In the third, these results are combined to ascertain the uncertainty expected in the experimental results.

4.3.1 The Transformation Matrix

For the coordinate system shown in Fig. 4. it can be shown that the velocity components u, v and w can be written in terms of v_1, v_2 and v_3 (the velocity components as measured by the LV system) as follows

$$\begin{aligned} u &= \frac{v_1 + v_2}{2\cos\theta} \\ v &= \frac{v_1 - v_2}{2\sin\theta} \\ w &= -\frac{u}{\tan\phi} + \frac{v_3}{\sin\phi} \end{aligned} \tag{11}$$

where θ is the angle in the x-y plane between the x axis and measurement directions 1 and 2, and ϕ is the angle in the x-z plane between the x axis and measurement direction 3. Snyder, et al., [62] have pointed out that this set of equations, for a

generalized three-dimensional LV system, can be expressed in matrix form as

$$\left\{ \begin{array}{c} u \\ v \\ w \end{array} \right\} = \left\{ \begin{array}{ccc} a_{11} & a_{12} & a_{13} \\ a_{21} & a_{22} & a_{23} \\ a_{31} & a_{32} & a_{33} \end{array} \right\} \left\{ \begin{array}{c} v_1 \\ v_2 \\ v_3 \end{array} \right\}. \tag{12}$$

Therefore Eq. (12) can be rewritten as

$$\left\{ \begin{array}{c} u \\ v \\ w \end{array} \right\} = \left\{ \begin{array}{ccc} \frac{1}{2\cos\theta} & \frac{1}{2\cos\theta} & 0 \\ \frac{1}{2\sin\theta} & -\frac{1}{2\sin\theta} & 0 \\ -\frac{1}{2\cos\theta\tan\phi} & -\frac{1}{2\cos\theta\tan\phi} & \frac{1}{\sin\phi} \end{array} \right\} \left\{ \begin{array}{c} v_1 \\ v_2 \\ v_3 \end{array} \right\}. \tag{13}$$

4.3.2 Formulations for Uncertainty Propagation

Uncertainty analysis in multiple sample experimental work is discussed at length in a manual by the American Society of Mechanical Engineers [63] and is discussed in some length by Schenck [64]. Similar work for single sample experiments was first published in 1953 by Kline and McClintock [65]. This discussion was extended by Moffat [66] in 1982.

Formulations are given in the literature to assess the propogation of uncertainty through complete experiments. The two formulations given are called the "constant odds" estimate and the "worst case" estimate. Both of these equations are given below. Most useful in engineering situations is the constant odds formulation which is obtained by a Taylor series expansion and requires equal confidence in each of the uncertainty levels as well as independence of the independent variables. The resulting uncertainty calculated from this formulation can then be used with the same confidence. When conservative estimates are required the worst case estimate is used. Monte Carlo methods have shown [66] that the worst case method gives bounds on uncertainty that capture the true value 99% of the time while the constant odds formulation does so 95% of the time.

The worst case formulation is written

$$\Delta R = \left| \frac{\partial R}{\partial x_1} \Delta x_1 \right| + \left| \frac{\partial R}{\partial x_2} \Delta x_2 \right| + \left| \frac{\partial R}{\partial x_3} \Delta x_3 \right| + \cdots. \tag{14}$$

The constant odds formulation will be used throughout this thesis since it gives estimates which are more useful in an engineering situation, for three variables it

can be written as

$$\Delta R = \left\{ \left[\frac{\partial R}{\partial x_1} \Delta x_1 \right]^2 + \left[\frac{\partial R}{\partial x_2} \Delta x_2 \right]^2 + \left[\frac{\partial R}{\partial x_3} \Delta x_3 \right]^2 \right.$$
$$\left. + 2 \left[\frac{\partial R}{\partial x_1} \frac{\partial R}{\partial x_2} \Delta x_1 \Delta x_2 + \frac{\partial R}{\partial x_1} \frac{\partial R}{\partial x_3} \Delta x_1 \Delta x_3 + \frac{\partial R}{\partial x_2} \frac{\partial R}{\partial x_3} \Delta x_2 \Delta x_3 \right] \right\}^{1/2} . \tag{15}$$

However, in the case where the variables are independent, e.g., a non-simultaneous LV system the $\Delta x_i \Delta x_j$ fluctuation terms tend to zero. These equations can be expanded to give the relative uncertainty in R as a function of the relative uncertainty in each of the variables. Equation (14) can be rewritten as

$$\frac{\Delta R}{R} = \left| \frac{x_1}{R} \frac{\partial R}{\partial x_1} \frac{\Delta x_1}{x_1} \right| + \left| \frac{x_2}{R} \frac{\partial R}{\partial x_2} \frac{\Delta x_2}{x_2} \right| + \left| \frac{x_3}{R} \frac{\partial R}{\partial x_3} \frac{\Delta x_3}{x_3} \right| + \cdots . \tag{16}$$

If no correlation exists between the variables, i.e, if independence of the variables is assumed, Eq. (15) can be written as

$$\frac{\Delta R}{R} = \frac{1}{R} \left\{ \left[x_1 \frac{\partial R}{\partial x_1} \frac{\Delta x_1}{x_1} \right]^2 + \left[x_2 \frac{\partial R}{\partial x_2} \frac{\Delta x_2}{x_2} \right]^2 + \left[x_3 \frac{\partial R}{\partial x_3} \frac{\Delta x_3}{x_3} \right]^2 + \cdots \right\}^{1/2} . \tag{17}$$

4.3.3 Uncertainty Propagation in LV Measurements

The equations in the previous section provide a means of calculating how the uncertainty in the original LV measurements propagate into the calculated results, namely, the velocity components, the velocity magnitude and the Mach number.

In this section a methodology is presented which allows estimation of uncertainty in any of the calculated quantities for any generalized LV system having an architecture similar to that used in this study. As will be shown, the uncertainty in these quantities is a function of the uncertainty in the original LV measurements (denoted $\Delta v_i / v_i$), the LV system geometry, and the flow conditions.

To determine the uncertainty in u, v, and w Eqs. (12) and (17) can be combined to give:

$$\left\{ \frac{\Delta u}{u} \right\}^2 = \left\{ \frac{1}{u} \right\}^2 \left\{ \left[a_{11} v_1 \frac{\Delta v_1}{v_1} \right]^2 + \left[a_{12} v_2 \frac{\Delta v_2}{v_2} \right]^2 + \left[a_{13} v_3 \frac{\Delta v_3}{v_3} \right]^2 \right\}$$
$$\left\{ \frac{\Delta v}{v} \right\}^2 = \left\{ \frac{1}{v} \right\}^2 \left\{ \left[a_{21} v_1 \frac{\Delta v_1}{v_1} \right]^2 + \left[a_{22} v_2 \frac{\Delta v_2}{v_2} \right]^2 + \left[a_{23} v_3 \frac{\Delta v_3}{v_3} \right]^2 \right\} \tag{18}$$

$$\left\{\frac{\Delta w}{w}\right\}^2 \;=\; \left\{\frac{1}{w}\right\}^2 \left\{\left[a_{31}v_1\frac{\Delta v_1}{v_1}\right]^2 + \left[a_{32}v_2\frac{\Delta v_2}{v_2}\right]^2 + \left[a_{33}v_3\frac{\Delta v_3}{v_3}\right]^2\right\}.$$

Substituting in the matrix elements and solving in terms of u, v and w, and using the assumption that $\Delta v_i/v_i = \Delta v_1/v_1 = \Delta v_2/v_2 = \Delta v_3/v_3$, will give after rearranging:

$$\left\{\frac{\Delta u}{u}\right\}^2 \;=\; \left\{\frac{\Delta v_i}{v_i}\right\}^2\left\{\frac{1}{2}+\frac{1}{2}\left[\frac{v}{u}\tan\theta\right]^2\right\} + \left\{\frac{\Delta\theta}{\theta}\right\}^2\{\theta\tan\theta\}^2 \tag{19}$$

$$\left\{\frac{\Delta v}{v}\right\}^2 \;=\; \left\{\frac{\Delta v_i}{v_i}\right\}^2\left\{\frac{1}{2}+\frac{1}{2}\left[\frac{1}{\frac{v}{u}\tan\theta}\right]^2\right\} + \left\{\frac{\Delta\theta}{\theta}\right\}^2\left\{\frac{\theta}{\tan\theta}\right\}^2 \tag{20}$$

$$\left\{\frac{\Delta w}{w}\right\}^2 \;=\; \left\{\frac{\Delta v_i}{v_i}\right\}^2\left\{1 + 2\left[\frac{u/w}{\tan\phi}\right] + \left[\frac{u/w}{\tan\phi}\right]^2\left[\frac{3}{2}+\frac{1}{2}\left(\frac{v}{u}\tan\theta\right)^2\right]\right\}$$

$$+\; \left\{\frac{\Delta\theta}{\theta}\right\}^2\left\{\theta\tan\theta\left[\frac{u/w}{\tan\phi}\right]\right\}^2$$

$$+\; \left\{\frac{\Delta\phi}{\phi}\right\}^2\phi^2\tan^2\phi\left\{\frac{1}{\tan^2\phi}-\frac{u/w}{\tan\phi}\right\}^2. \tag{21}$$

In order to more readily estimate LV system uncertainty, these expressions can be broken down and subsequently plotted in pieces. The expressions for the uncertainty of the u and v components are particularly simple:

$$\left\{\frac{\Delta u}{u}\right\}^2 \;=\; A\left(\frac{\Delta v_i}{v_i},\frac{v}{u}\tan\theta\right) + B\left(\frac{\Delta\theta}{\theta},\theta\right) \tag{22}$$

$$\left\{\frac{\Delta v}{v}\right\}^2 \;=\; C\left(\frac{\Delta v_i}{v_i},\frac{v}{u}\tan\theta\right) + D\left(\frac{\Delta\theta}{\theta},\theta\right) \tag{23}$$

$$\left\{\frac{\Delta w}{w}\right\}^2 \;=\; \left\{\frac{\Delta\phi}{\phi}\right\}^2 E\left(\frac{u/w}{\tan\phi},\phi\right)$$

$$+\; \left\{\frac{\Delta v_i}{v_i}\right\}^2 F\left(\frac{u/w}{\tan\phi},\frac{v}{u}\tan\theta\right)$$

$$+\; \left\{\frac{\Delta\theta}{\theta}\right\}^2 G\left(\frac{u/w}{\tan\phi},\theta\right) \tag{24}$$

Due to their simplicity the expressions for $\Delta u/u$ and $\Delta v/v$ are plotted differently than that for $\Delta w/w$. Plotting Eqs. (22) and (23) in terms of A, B, C and D allows direct determination of the uncertainties in u and v (Figs. 8 and 9). In Fig. 10, E, F and G from Eq. (24) are plotted against the appropriate variables so that given an estimate of the input uncertainties, and LV system geometry, an estimate of the uncertainty in w can be made.

An expression for the uncertainty in the total velocity magnitude can be written out as

$$\left\{\frac{\Delta V}{V}\right\}^2 = \left\{\frac{\Delta u}{u}\right\}^2 \left\{\frac{u}{V}\right\}^4 + \left\{\frac{\Delta v}{v}\right\}^2 \left\{\frac{v}{V}\right\}^4 + \left\{\frac{\Delta w}{w}\right\}^2 \left\{\frac{w}{V}\right\}^4 \tag{25}$$

or

$$\left\{\frac{\Delta V}{V}\right\}^2 = \left\{\frac{\Delta u}{u}\right\}^2 H(\alpha,\beta) + \left\{\frac{\Delta v}{v}\right\}^2 I(\alpha,\beta) + \left\{\frac{\Delta w}{w}\right\}^2 J(\alpha,\beta) \tag{26}$$

where

$$H(\alpha,\beta) = \left\{\frac{u}{V}\right\}^4 = \left\{\frac{1}{\sqrt{1+\tan^2\alpha+\tan^2\beta}}\right\}^4$$

$$I(\alpha,\beta) = \left\{\frac{v}{V}\right\}^4 = \left\{\frac{\tan\alpha}{\sqrt{1+\tan^2\alpha+\tan^2\beta}}\right\}^4 \tag{27}$$

$$J(\alpha,\beta) = \left\{\frac{w}{V}\right\}^4 = \left\{\frac{\tan\beta}{\sqrt{1+\tan^2\alpha+\tan^2\beta}}\right\}^4 .$$

To simplify evaluation of Eq. (25), H, I and J are plotted in Fig. 11.

To calculate the uncertainty in the Mach number, Eq. (10) can be combined with Eq. (17) to get

$$\left\{\frac{\Delta M}{M}\right\}^2 = \left\{\frac{\Delta T}{T}\right\}^2 \left\{-\frac{1}{2} - \frac{(\gamma-1)M^2}{4}\right\}^2 + \left\{1 + \frac{(\gamma-1)M^2}{2}\right\}^2 \times$$
$$\left\{\left[\frac{\Delta u}{u}\right]^2\left[\frac{u}{V}\right]^4 + \left[\frac{\Delta v}{v}\right]^2\left[\frac{v}{V}\right]^4 + \left[\frac{\Delta w}{w}\right]^2\left[\frac{w}{V}\right]^4\right\} \tag{28}$$

which after inspection gives:

$$\left\{\frac{\Delta M}{M}\right\}^2 = \left\{1 + \frac{(\gamma-1)M^2}{2}\right\}^2 \left\{\left[\frac{\Delta V}{V}\right]^2 + \frac{1}{4}\left[\frac{\Delta T}{T}\right]^2\right\}. \tag{29}$$

The above analysis is intended to facilitate uncertainty estimation for LV systems having similar geometry to the system used in this investigation. Great care must be taken to pursue minimizing the uncertainty of only the quantities of interest. As an example, in the present investigation, had only the flow Mach number been of interest, pursuing the w component would have been very costly. This is true because of the small impact of w on the calculated Mach number, due to the relatively small flow angles involved.

4.3.4 Determination of $\Delta v_i / v_i$

As previously mentioned, the uncertainty in each of the measurements v_1, v_2 and v_3 is assumed to be the same and is denoted by $\Delta v_i / v_i$. Determination of this value will enable the uncertainty in u, v, w, V and Mach number to be calculated from the previous analysis.

The uncertainty in v_i is divided into two parts. The first part is due to the stochastic nature of LV measurements. The second is due to the fixed or systematic limitations in making the LV measurements (i.e., bound systematic uncertainty). These two analyses will be carried out separately and combined using each of the two methods recommended in the literature.

The uncertainty due to the stochastic nature of a measurement will be discussed first. The uncertainty attributed to a measurement due to statistical considerations is given by estimation theory to be

$$\Delta v = \frac{z_c}{\sqrt{N}} s_v \tag{30}$$

where s_v is an estimate of the standard deviation calculated from N samples and z_c is the confidence coefficient, taken from Student's t distribution. The relative uncertainty is then given by

$$\frac{\Delta v}{v} = \frac{z_c}{\sqrt{N}} \frac{s_v}{v} \tag{31}$$

where s_v / v is an estimate of the turbulence level calculated from N measurement samples. For a normal distribution and a confidence level of 95%, z_c is 1.96. This equation allows determination of the uncertainty in each of the LV components due to turbulence.

The theoretical expression for velocity is given by

$$v = \frac{\lambda}{2 \sin \kappa} \frac{N_f}{t} = \frac{N_f d_f}{t} \tag{32}$$

where t is the ensemble average of the time measurements. The other quantities, κ (one-half the beam crossing angle), N_f (the number of fringes required), and λ, (the laser light wavelength) were held fixed during the LV surveys.

However, to derive an expression for uncertainty due to randomness, another source of uncertainty must be included which is not obvious from the theoretical

development. This added complication is to account for the slight divergence of probe volume fringes in real LV systems. Theoretically, for the fringes to be parallel the two incoming laser beams must be imaged precisely at the beam crossing point (i.e., the beam waists must coincide at the location of the probe volume). Since this is very difficult to ascertain, the fringe divergence must be included in the uncertainty analysis. It is included as the second term of Eq. (33 below. Since κ and λ are fixed, combining Eqs. (17) and (32) gives

$$\frac{\Delta v_i}{v_i}\bigg|_r = \sqrt{\left\{\frac{t}{v_i}\frac{\partial v_i}{\partial t}\frac{\Delta t}{t}\right\}^2 + \left\{\frac{d_f}{v_i}\frac{\partial v_i}{\partial d_f}\frac{\Delta d_f}{d_f}\right\}^2} \tag{33}$$

which reduces to

$$\frac{\Delta v_i}{v_i}\bigg|_r = \sqrt{\left\{\frac{\Delta t}{t}\bigg|_r\right\}^2 + \left\{\frac{\Delta d_f}{d_f}\right\}^2} \tag{34}$$

To evaluate the uncertainty in the time measurement, the quantity $\Delta t/t$ is divided into three pieces:

$$\left\{\frac{\Delta t}{t}\bigg|_r\right\}^2 = \left\{\frac{\Delta t}{t}\bigg|_{flow}\right\}^2 + \left\{\frac{\Delta t}{t}\bigg|_{timer}\right\}^2 + \left\{\frac{\Delta t}{t}\bigg|_{wordlength}\right\}^2. \tag{35}$$

The first term concerns the statistical nature of the flow itself. The second concerns the limitation of the clock speed of the signal processor, which is a fixed value for a single measurement, but is mitigated by taking multiple measurements. The third factor is caused by the limit on word length in the transfer of data from the processor to the computer. It is also mitigated by taking multiple measurements. These three terms as well as the $\Delta d_f/d_f$ term will be discussed in the following.

Since

$$\frac{\Delta t}{t}\bigg|_{flow} = -\frac{\Delta v}{v} \tag{36}$$

the first term of Eq. (35) can be written

$$\left\{\frac{\Delta t}{t}\bigg|_{flow}\right\}^2 = \left\{\frac{\Delta v}{v}\right\}^2$$

$$= \left\{\frac{z_c}{\sqrt{N}}\frac{s_v}{v}\right\}^2. \tag{37}$$

Thus, this term can be determined providing the flow turbulence level is known.

The second term can be written

$$\frac{\Delta t}{t}\bigg|_{timer} = \frac{1}{\sqrt{N}} r_t \tag{38}$$

where r_t is the resolution of the timer. With a signal processor clock resolution of 2 nanoseconds and a minimum fringe crossing time of approximately 100 nanoseconds (6.4μm $\times$ 8 fringes $\div$ 500 m/s), this results in an uncertainty of 1 part in 50. This is the uncertainty in one measurement. However, with large N the uncertainty due to clock resolution is very small and will be neglected.

Similarly, the third term can be written

$$\frac{\Delta t}{t}\bigg|_{wordlength} = \frac{1}{\sqrt{N}} r_w \tag{39}$$

where r_w is the resolution limit on the word length in the transfer of time information from the counter processor to the computer. In this study, a TSI, Inc. 1990A counter processor was used which transfers the time data with a 16 bit word composed of a 12 bit mantissa and a 4 bit exponent, giving a resolution of 1 part in 8194 (2^{13}). The uncertainty due to wordlength limitation is therefore very small and will be neglected.

It is well known that the laser velocimeter is not usable in low turbulence flows when turbulence information is required since most large scale laser velocimeters are known to give an apparent minimum turbulence level of approximately 0.3% no matter how low the flow turbulence level. Therefore, for many LV systems, it must be assumed that over the length of the probe volume the fringes diverge approximately 0.3%. Using the assumptions above the expression for the uncertainty due to randomness can then be given as

$$\frac{\Delta v_i}{v_i}\bigg|_r = \sqrt{\left\{\frac{z_c}{\sqrt{N}}\frac{s_v}{v}\right\}^2 + \left\{\frac{3}{1000}\right\}^2}. \tag{40}$$

The bound systematic uncertainty can be obtained by combining Eqs. (17) and (32) which results in:

$$\frac{\Delta v_i}{v_i}\bigg|_s = \sqrt{\left\{\frac{\kappa}{v_i}\frac{\partial v_i}{\partial \kappa}\frac{\Delta \kappa}{\kappa}\right\}^2 + \left\{\frac{t}{v_i}\frac{\partial v_i}{\partial t}\frac{\Delta t}{t}\bigg|_s\right\}^2 + \left\{\frac{\lambda}{v_i}\frac{\partial v_i}{\partial \lambda}\frac{\Delta \lambda}{\lambda}\right\}^2}. \tag{41}$$

This reduces to

$$\frac{\Delta v_i}{v_i}\bigg|_s = \sqrt{\left\{\frac{\kappa}{\tan\kappa}\frac{\Delta\kappa}{\kappa}\right\}^2 + \left\{\frac{\Delta t}{t}\bigg|_s\right\}^2 + \left\{\frac{\Delta\lambda}{\lambda}\right\}^2}. \tag{42}$$

In this experiment κ was determined by projecting the two crossing laser beams onto a far wall that was perpendicular to the optical axis of the LV system. This was done with one window in place and the other removed to allow direct access to the probe volume. Measurements were then made of the distance between the two beam spots (B) and the distance from the wall to the probe volume (R) so that κ is given by

$$\kappa = \tan^{-1}\frac{B}{2R}. \tag{43}$$

The first term in Eq. (42) can then be written

$$\frac{\kappa}{\tan\kappa}\frac{\Delta\kappa}{\kappa} = \frac{1}{\tan\kappa}\sqrt{\left\{B\frac{\partial\kappa}{\partial B}\frac{\Delta B}{B}\right\}^2 + \left\{R\frac{\partial\kappa}{\partial R}\frac{\Delta R}{R}\right\}^2}. \tag{44}$$

Using Eq. (43) this reduces to

$$\frac{\kappa}{\tan\kappa}\frac{\Delta\kappa}{\kappa} = \frac{\sqrt{\left\{\frac{\Delta B}{B}\right\}^2 + \left\{\frac{\Delta R}{R}\right\}^2}}{1 + \left(\frac{B}{2R}\right)^2}. \tag{45}$$

The systematic uncertainties in the time measurement and in laser wavelength can be assumed to be very small so that Eq. (42) reduces to

$$\frac{\Delta v_i}{v_i}\bigg|_s = \frac{\sqrt{\left\{\frac{\Delta B}{B}\right\}^2 + \left\{\frac{\Delta R}{R}\right\}^2}}{1 + \left(\frac{B}{2R}\right)^2}. \tag{46}$$

The measurements used to determine this beam crossing angle provide the information necessary to estimate the systematic uncertainty. R was measured to be 4.78 m (188 in.) with a ΔR estimated to be 5 cm (2 in.). B was 13.8 cm ($15\frac{7}{16}$ in.) with a ΔB estimated to be 1.5 mm (1/16 in.). This results in an uncertainty $\Delta v_i/v_i$ of approximately 1 part in 88 due to systematic uncertainty:

$$\frac{\Delta v_i}{v_i}\bigg|_s = \frac{1}{88}. \tag{47}$$

The random and systematic uncertainties can be combined using either Eq. (16) or Eq. (17). Both methods are recommended in the literature. However, it has

recently been suggested [67] that it is unimportant which method is used so long as estimates for each of the terms is provided separately. Using Eq. (16) results in:

$$\frac{\Delta v_i}{v_i} = \left|\frac{\Delta v_i}{v_i}\right|_r + \left|\frac{\Delta v_i}{v_i}\right|_s$$

$$= \frac{z_c}{\sqrt{N}}\frac{s_{v_i}}{v_i} + \frac{3}{1000} + \frac{1}{88}. \qquad (48)$$

The formulation given by Eq. (17) produces

$$\frac{\Delta v_i}{v_i} = \sqrt{\left\{\frac{\Delta v_i}{v_i}\Big|_r\right\}^2 + \left\{\frac{\Delta v_i}{v_i}\Big|_s\right\}^2}$$

$$= \sqrt{\left\{\frac{z_c}{\sqrt{N}}\frac{s_{v_i}}{v_i}\right\}^2 + \left\{\frac{3}{1000}\right\}^2 + \left\{\frac{1}{88}\right\}^2} \qquad (49)$$

The following table contains estimates of the uncertainty in v_i using the constant odds assumption with the worst case estimates given in parentheses. The sample size N was fixed at 1000 for all measurements of u and v. The sample size was increased to 8000 for the measurements of w. The maximum turbulence level encountered in the Mach 1.3 study was approximately 10%; during the Mach 1.6 test the maximum level was approximately 20%.

Case↓ Regime→	u,v	w
Mach 1.3	1.3%(2.1%)	1.2%(1.7%)
Mach 1.6	1.7%(2.7%)	1.3%(1.9%)

Table 1. Maximum estimated uncertainty $\Delta v_i/v_i$,

given by the constant odds formulation. In parenthesis

are the worst case estimates.

4.3.5   Statistically Correlated Data

For completeness the following section discusses the advantage in obtaining multiple component LV measurements simultaneously.

When realizations are obtained by all of the LV components simultaneously, i.e., each set of realizations can be attributed to the same particle, there is a statistical correlation present in the data. This correlation serves to enhance the statistical significance of the data.

Simultaneous measurements are possible in multi-component LV systems where the probe volumes overlap precisely and when the system is setup to require simultaneity. However, this is not normally possible in real LV systems for a variety of reasons. Probe volumes rarely overlap exactly due to small probe volume size and the lack of sufficient mechanical stability of the optical train. Even when this is possible, LV systems suffer a severe reduction in data acquisition rate, thereby greatly prolonging time required to complete an experiment. This is not normally feasible in large scale experimental facilities. However, when simultaneous measurements are possible, the correlation inherent in the data can serve to significantly reduce the resulting statistical uncertainty. The magnitude of this reduction is dependent on the LV system geometry. This was shown experimentally by Orloff and Snyder [68].

If the ensemble average is taken to be the time average, then Eq. (15) can be rewritten to give

$$
\begin{Bmatrix} s_u^2 \\ s_v^2 \\ s_w^2 \end{Bmatrix} = \begin{Bmatrix} a_{11}^2 & a_{12}^2 & a_{13}^2 \\ a_{21}^2 & a_{22}^2 & a_{23}^2 \\ a_{31}^2 & a_{32}^2 & a_{33}^2 \end{Bmatrix} \begin{Bmatrix} s_1^2 \\ s_2^2 \\ s_3^2 \end{Bmatrix} + 2 \begin{Bmatrix} a_{11}a_{12} & a_{11}a_{13} & a_{12}a_{13} \\ a_{21}a_{22} & a_{21}a_{23} & a_{22}a_{23} \\ a_{31}a_{32} & a_{31}a_{33} & a_{32}a_{33} \end{Bmatrix} \begin{Bmatrix} \overline{v_1' v_2'} \\ \overline{v_1' v_3'} \\ \overline{v_2' v_3'} \end{Bmatrix}
$$
(50)

where

$$
\overline{v_x' v_y'} = \frac{1}{N} \sum_{j=1}^{N} \left\{ v_{x_j} - \overline{v_x} \right\} \left\{ v_{y_j} - \overline{v_y} \right\}
$$
(51)

represents the covariance.

For uncorrelated data, i.e., measurements of v_1, v_2 and v_3 made from different particles, Eq. (50) reduces to the results obtained in section 4.3.2:

$$
\begin{Bmatrix} s_u^2 \\ s_v^2 \\ s_w^2 \end{Bmatrix} = \begin{Bmatrix} a_{11}^2 & a_{12}^2 & a_{13}^2 \\ a_{21}^2 & a_{22}^2 & a_{23}^2 \\ a_{31}^2 & a_{32}^2 & a_{33}^2 \end{Bmatrix} \begin{Bmatrix} s_1^2 \\ s_2^2 \\ s_3^2 \end{Bmatrix}.
$$
(52)

4.3.6 Uncertainty Summation

The uncertainty estimates resulting from the analysis of the previous two sections are combined and summarized in this section. The system geometry and input uncertainty parameters used in this section are given in the following table.

Parameter	Value	Comments
$\Delta v_i / v_i$	1.7%	u and v Measurements
$\Delta v_i / v_i$	1.3%	w Measurements
$\Delta \theta / \theta$	1/60	All Measurements
$\Delta \phi / \phi$	1/60	All Measurements
θ	30°	All Measurements
ϕ	28°	All Measurements

Table 2. Parameters used to determine the uncertainty in the results.

The resulting uncertainty in u, v, w, V and M for each of the test cases are shown in Figs. 12 through 17.

Figures 12 and 13 show the uncertainty in u and v as a function of the flow angle in the x-y plane, α. Figure 14 gives the uncertainty in w as a function of α and β; the uncertainty in w is a very weak function of α and so has been replotted in Fig. 15 as a function of $\Delta v_i / v_i$. As can be seen, for small values of β the uncertainty in w becomes very high.

The uncertainty in V is shown in Fig. 16 and can be seen to be less than 2% for all the flow angles that would be encountered in this flowfield. The uncertainty in Mach number (Fig. 17) is seen to be slightly larger due to the uncertainty in the total temperature, but is still less than 3%.

From the measurements of u and w an analysis was made to determine where it would be feasible to measure the w component; the criterion being the level of uncertainty in w. From Fig. 15 it can be seen that the uncertainty in w is a strong function of the flow angle β, as well as the uncertainty in v_i. The number of realizations required for each LV ensemble was increased from 1000 to 8000 in an attempt to reduce the statistical "jitter" in w to the level found in u and v.

To achieve a reasonable level of uncertainty, w measurements were restricted for both test cases to regions where the flow angle β was expected to be greater than approximately 5°. The well behaved results tend to support this analysis.

As noted by Orloff and Snyder [68], great care must be exercised in determining the elements in Eq. (12) when ϕ is small. Otherwise, large systematic uncertainty can result in w.

Chapter 5

Results and Discussion

5.1   Introduction

In this chapter the results of the surface oil flow visualization, the schlieren photography and the wall static pressure as well as the laser velocimeter measurements will be presented and discussed.

5.2   Flow Visualization Results

Schlieren photography has proven to be very valuable in analyzing and interpreting flowfields where density gradients exist. However, it must be kept in mind that schlieren photographs present information that is integrated across the span of the flow.

The interpretation of surface flow visualization results in complicated three-dimensional flows has recently received greater attention than in the past. The mathematics was given early in this century but has only recently been resurrected and discussed [69, 70, 71].

The oil flow visualization technique is very controversial in the aerospace research community at this time for a variety of reasons. Some researchers believe that these techniques are applicable only to two-dimensional steady flows and that their use in unsteady flows only disrupts the progress in the study of these flows. This is because the technique presents a time averaged "footprint" of the flow at the surface that

appears similar to those found in steady two-dimensional flows when in fact the flow physics may be quite different. In addition, it has been shown that coating the surface with a foreign substance will change the shear rate at the wall and can alter the flow away from the wall significantly.

Care must therefore be taken in interpretating flow visualization results in three-dimensional flows. Nevertheless, important information can be obtained about the flowield structure and physics.

The video monitor system indicated that for both test cases at startup the shock wave oscillated randomly with an amplitude of ± 1 cm about the mean shock location. However, this amplitude decreased with time as evidenced by the results.

5.2.1 The Mach 1.3 Flow Visualization Results

For the Mach 1.3 case, the schlieren photographs, shown in Fig. 18 reveals that the shock gradually vanishes as it approaches the boundary layer. Weak compression waves can be seen that sweep forward of the main shock and terminate in the boundary layer. This may be taken to be a precursor of the lambda shock which appears at higher Mach numbers. A large increase in the boundary layer thickness can also be seen in the photo.

The oil flow visualization photograph shown in Fig. 19 indicates that there is either no separation or very isolated corner separation in the Mach 1.3 test case. The surface flow appears to be very uniform although there is some very slight buildup of oil in the vicinity of the shock. This indicates a decrease in the shear rate near the shock which is expected due to the adverse pressure gradient present.

5.2.2 The Mach 1.6 Flow Visualization Results

For the Mach 1.6 case the schlieren photograph shown in Fig. 20 indicates that the shock becomes bifurcated as it approaches the boundary layer. The shock structure, which is known to occur at Mach numbers above 1.4 in the two-dimensional case, is called the lambda shock configuration. A large increase in the boundary layer thickness can also be seen. Reflections arise from the rear leg of the lambda shock

which cross near the tunnel centerline. This phenomena has not been seen in the two-dimensional case. A slip line is observable extending downstream of the bifurcation point and is due to the flow on either side of the primary shock passing through different shock systems.

The surface oil flow visualization photograph of Fig. 21 indicates that large separation regions exist in each of the four corners. The flow in the corners is highly three-dimensional and an accumulation of oil can be seen in the vicinity of the shock wave. This is due to the adverse pressure gradient as in the Mach 1.3 case. No reattachment occurs over the length of the test section. The image shown in the figure was mirrored on each of the other surfaces in the test section, indicating a high degree of symmetry.

5.3   Surface Static Pressure Measurements

The floor static pressure distributions for the two test cases were normalized to the upstream mid-span wall static pressure and are plotted in Figs. 22 and 23. The reference pressures were measured and were found to be equal to the pressures given by isentropic flow relations. The first row of static pressure taps corresponded to the z axis, i.e., along x = 0.

The plot for the Mach 1.3 case indicates that a nearly uniform pressure gradient exists across the span of the tunnel. Some sweeping forward of the pressure ratio contours near the corners is indicated in Fig. 22 along with a high degree of symmetry. The pressure recovery ratio given by the normal shock relations at a Mach number of 1.28 is $p_2/p_1 = 1.745$. The pressure ratio as the flow leaves the test section is just under 1.45.

The static pressure results for the Mach 1.6 case indicate a much more three-dimensional flow than the previous case. There is a much more pronounced sweeping forward of the pressure ratio contours near the sidewalls for this case which indicates a sweeping forward of the front legs of the lambda shock near the sidewalls. This was later confirmed in the LV data.

The expected pressure ratio given by the normal shock relations is $p_2/p_1 = 2.82$. At the exit of the test section the pressure ratio indicated by Fig. 23 is just under

2.1. A symmetric flow is also indicated by the contours.

The centerline pressure ratio for the Mach 1.3 and 1.6 cases is plotted in Fig. 24, and is compared to previous two-dimensional cases having similar Mach numbers.

5.4 Laser Velocimeter Results

For both the test cases the mean shock location was maintained at $x = 10$ cm. There was some unsteadiness in the shock position as stated previously, however, the time-mean location was steady. In the Mach 1.6 case the oscillations appeared in the cross sectional data at $x = 10$ cm. Because of this the LV data at this location is not useful and is not included in the results.

All the laser velocimeter measurements presented herein were determined by ensemble averaging of the individual realizations at each point. Since the turbulence levels for these flows was never greater than 20%, velocity bias has not been considered in the reduction of the data [47]. The data are presented in terms of local Mach number because the total temperature varied from test run to test run depending on the air handlers that were in use at the time. In the following the laser velocimeter results for the Mach 1.3 test case will be presented followed by the Mach 1.6 test case.

5.4.1 The Mach 1.3 Results

The results of the Mach 1.3 investigation indicate a less dynamic, less complicated and more uniform flowfield than was found in the Mach 1.6 test case. The results for the mid-span laser velocimeter survey is given in Fig. 25 and is convenient for comparison with the schlieren photographic results. As expected, there is no indication of a lambda shock which is known to occur at Mach numbers above 1.4. Instead, the shock gradually vanishes as it extends into the boundary layer. The growth of the boundary layer through the interaction region is also indicated. The flow along the tunnel centerline, shocks down as predicted from one-dimensional normal shock relations but then immediately begins to reaccelerate to sonic speed.

Cross sectional surveys for the Mach 1.3 case are given in Figs. 26-34. The

flow entering the test section is very uniform and no indication of disruptions of the incoming flow are evident. The shock wave was located at x = 10 cm, and, in the Mach 1.3 case, very little indication of the interaction occurs upstream of this point. There is a region of high-speed flow in the corner that extends downstream of the shock. This appears to be a superonic "tongue" similar to that described by Seddon's two-dimensional model of the shock wave/boundary layer interaction. This supersonic region remains isolated near the corner and becomes smaller and smaller downstream. At the exit of the test section, this region of supersonic flow nearly vanishes, while the remainder of the flowfield is choked at Mach 0.99.

The secondary flow vectors are also shown in Figs. 26-34. The plots indicate very little secondary flow. The slight flow turning is near the limit of the resolution of the LV system. This resolution is a function of the flowfield turbulence along with the turning angle of the flow. There is some indication of a tendency of the flow to turn away from the corner.

5.4.2   The Mach 1.6 Results

The results of the Mach 1.6 investigation show that the flow follows the one-dimensional normal shock relationships only in the center of the tunnel, and then, only immediately downstream of the shock. The flow then reaccelerates to become supersonic and then experiences two weaker secondary shocks. This is shown in Fig. 35. As in the previous case this figure lends itself to comparison with the schlieren results.

The lambda shock is clearly indicated in the figure as is the growth of the boundary layer due to the adverse pressure gradient. Just downstream of the bifurcation point a slip line is present which has been seen in previous two-dimensional investigations. The slip line is obscured further downstream due to the reacceleration in the freestream and the secondary shocks associated with the three-dimensionality of the flow.

Although LV surveys were made near the corner, as close as 1.5 cm (0.4 in.) from the sidewall and floor, no reverse flow was ever detected. However, extensive separation was indicated in the flow visualization results so the extent of separation

away from the wall could not be determined. The smallest velocity measured in this region corresponded to an approximate Mach number of 0.3 (100 m/s). The LV data acquired in the y-z plane survey stations for the Mach 1.6 case are plotted in Figs. 36-44 in the form of local total Mach number contours and secondary flow vectors. A sweeping forward of the front legs of the lambda shock near the corner and a sweeping back of the rear legs are evident. Just downstream of the shock the flow is subsonic in the freestream, but remains supersonic near the corner. The supersonic corner region extends downstream where it interacts with the reaccelerating freestream flow and secondary shocks where it becomes indistinguishable. At $x = 24$ cm (9.4 in.), the flowfield has just passed through the secondary shock, i.e., the flow in the freestream is slightly slower than that nearer the corner. At $x = 30$ cm (11.8 in.), the flow is about to experience another weak normal shock. At $x = 35$ cm (13.8 in.), the flow is nearly uniform in the freestream and about to exit the test section. At this point the boundary layer has become very large so that the sonic line is approximately 4 cm (1.6 in.) from each of the walls.

The secondary flow vectors given in terms of Mach number are also shown in Figs. 36-44 for the Mach 1.6 case. The plots show the that the flow turns away from the walls under the lambda shock structure. Since the region where the w component was surveyed is limited, little else can be determined about the secondary flow structure outside the region of the lambda shock. However, it does appear that even 2 cm downstream of the shock the strength of the secondary flow has greatly diminished.

5.5 Shock Wave Spectral Analysis

In order to estimate the frequency at which the shock oscillated during this investigation, direct measurements were made of the u velocity component in the vicinity of the shock wave near the tunnel centerline. The probe volume of the LV system was positioned such that the shock wave oscillated back and forth across it while measurements were being made. The velocity upstream of the shock was on the order of 500 m/s (1640 ft/s) while the velocity downstream was only approximately 280 m/s (920 ft/s). The histogram for a typical data point is shown in Fig. 45.

Since the velocity gradient at a shock wave occurs over a very small distance, the time history of the flow will give a direct indication of shock location and when transformed into the frequency domain, will indicate shock frequency. The time history was constructed from the time-between-data (TBD) information which is recorded as part of the LV data. A time history for the same data point above is shown in Fig. 46. When tranformed into the frequency domain, the bandwidth of the spectral analysis is limited, due to the record length limit of 1000 realizations per measurement. However, some indication of oscillation frequency can be obtained.

The spectral analysis indicates that the shock oscillation frequency is relatively low, in that most of the energy in the shock oscillation is contained between 10 and 100 Hz. This is shown in Fig. 47.

The velocity bias is thought to be due to the fact that more high speed particles will pass through the probe volume than lower speed particles, thereby inducing statistical bias in the data. This would cause the time between realizations to go down as particle speed increases. However, this is not observed in the present investigation for LV data near the shock wave. The data point above is replotted with the time-between-data information in Fig. 48. The reason increase in the time between realizations with greater speed for this case is not clear. It has been argued that as the particle speed goes up the number of photons striking the receiver goes down linearly, thereby reducing the signal-to-noise ratio at higher speeds. This would tend to support the results in the figure. However, as has been pointed out by Meyers [72], these fewer photons strike the receiver in a proportionately shorter period of time so that the analog signal and therefore the signal-to-noise ratio should not change. The results in the figure may be caused by the breakup of the oil droplets as they pass through the shock wave.

Chapter 6

Conclusions and Remarks

6.1   Conclusions

Two separate test cases were examined during this investigation, one at a freestream Mach number of 1.3 and the other at a Mach number of 1.6. During both of these investigations the unit Reynolds number was maintained at 15×10^6/meter. The reason these Mach numbers were selected was because two entirely different flow structures were known to exist for two dimensional flows. The Mach 1.3 flow was known to be near the onset of separation. The Mach 1.6 flow is known to definitely result in boundary layer separation. The strategy for this experiment was therefore to study the flowfield at these two Mach numbers in order to develop an improved understanding of normal shock wave/boundary layer interaction flow physics and to provide data for assessment of numerical simulations.

The test results reveal that the structure of the shock system, the three dimensionality and the extent of separation are all highly dependent on the Mach number. The flowfield associated with the Mach 1.3 interaction is much more uniform than that found in the Mach 1.6 case. The extensive separation and hence, three-dimensionality in the Mach 1.6 case caused regions of strong acceleration behind the initial shock, thereby inducing a complicated set of secondary shock waves.

The separated flow regions along with the thickening boundary layer in the 1.6 case contribute to the three-dimensional nature of the interaction which serves to

affect an area change akin to a converging-diverging nozzle which causes the reacceleration in the freestream behind the shock.

The superposition of the boundary layers from the floor and sidewall enhance the boundary layer thickness in the corner region. This causes the front legs of the lambda shock in the 1.6 case to sweep forward near the corner and thereby create an increasingly oblique shock structure. This gives rise to the supersonic flow in the corner region, behind the front leg. This higher speed flow then forces back the rear leg of the lambda shock near the corner.

The secondary shock system and the occurrence of separation causes an erosion of the energy contained in the flow and causes strong non-uniformities to exist across the span of the tunnel. In addition, large turbulent structures are generated in a separated flow which serve to further dissipate the energy in the flow. Therefore these tests tend to confirm the general rule of inlet design wherein normal shocks are intended to occur only at Mach numbers of 1.3 and below.

6.2   Remarks

Until relatively recently, it was thought that an understanding of three-dimensional flows would require an understanding of the "underlying" two-dimensional flow physics. However, it is a now widely held belief that three-dimensional flows are vastly different from two-dimensional flows, and that the resulting "mindset" from thinking in two dimensions may impede the progress in the study of these "more complex" flows. This realization has resulted in an increased interest in the study of three-dimensional flows. This push to understand three-dimensional flows is also due to the enhanced computing capability widely available today, so that three-dimensional numerical simulations are becoming feasible. All this has resulted in an increase in the demand for three-dimensional unsteady non-intrusive flowfield instumentation. However, even the most sophisticated instumentation will not provide the answers without expertise and insight into the complex nature of the flow physics.

Detailed understanding of the flow phenomena occurring in these complicated flows is not possible with the completion of only one experimental investigation.

Virtually all of the simplest and most ubiquitous flows are not yet well understood, much less the more complicated flowfields. Therefore, the purpose of this investigation was not to unravel the three-dimensional flow physics but to provide a complete data set on which a knowledge base can be built.

Appendix A

Nomenclature

a_{ij}	elements of a 3 × 3 matrix used to convert the non-orthogonal LV component measurements into the orthogonal coordinate components
A_{pv}	projected frontal area of the probe volume
a_t	speed of sound based on the total temperature
$c_{real.}$	concentration of "realizations" as opposed to particles used to quantify LV system efficiency
d_f	fringe spacing
f	frequency
M	Mach number
N	number of LV realizations per measurement
N_f	number of fringes required per LV realization
N_v	validation rate indicated by the signal processor
r_t	signal processor timer or "clock" resolution
r_w	signal processor computer "word" resolution
s	estimate of the standard deviation
t	ensemble average of the LV time measurements
T	temperature
T_λ	Taylor time microscale
u, v, w	x, y, z components of fluid velocity
v_1, v_2, v_3	the three non-orthogonal ensemble averaged

	LV system velocity measurements
v_i	any one of the three non-orthogonal ensemble averaged LV measurements v_1, v_2, or v_3
$\vec{V}, \vec{v}$	fluid velocity vector
V, v	fluid velocity magnitude
z_c	confidence coefficient from Student's t distribution
α	flow angle in the x-y plane
β	flow angle in the x-z plane
γ	ratio of specific heats
Δ	absolute uncertainty in the quantity
δ	boundary layer thickness upstream of the interaction
θ	angle in the x-y plane between the x axis and LV components 1 and 2
κ	half angle between the laser beams of the LV system
λ	laser light wavelength
ϕ	angle in the x-z plane between the x axis and LV component 3
ω	weighting function

superscripts

$-$	average value
$\hat{}$	unit vector
$\rightarrow$	vector quantity

subscripts

D	Doppler shifted
$corrected$	corrected for velocity bias
est	estimate of the variable
i	any one of the LV components
r	random quantity
s	systematic or fixed quantity
u, v, w	refers to the x,y or z velocity components
$1, 2, 3$	refers to the original non-orthogonal LV components

References

[1] Lewis, J.E., "Experimental Investigation of Supersonic Laminar, Two-Dimensional Boundary Layer Separation in a Compression Corner With and Without Cooling," Ph.D. Thesis, Calif. Inst. Technol., 1967.

[2] Rose, W. C., "The Behavior of a Compressible Turbulent Boundary Layer in a Shock Wave Induced Pressure Gradient," NASA TN-D-7092, Washington, D.C., March, 1973.

[3] Seddon J., "Flow Produced by Interaction of a Turbulent Boundary Layer with a Normal Shock Wave of Strength Sufficient to Cause Separation," Brit. Aero. Res. Council Rept. and Memo. No. 3502, March 1960.

[4] Schlichting, H., *"Boundary-Layer Theory,"* McGraw-Hill Book Company, Seventh Edition, 1979, p. 365.

[5] Fage, R. and Sargent, R. F., "Shock Wave and Boundary Layer Phenomena Near a Flat Surface," *Proc. Roy. Soc.* Series A, Vol. 190, June, 1947.

[6] Liepmann, H.W., "The Interaction Between Boundary Layers and Shock Waves in Transonic Flow," *Journal of Aeronautical Sciences*, Vol. 13 No. 12, 1946, pp. 623-637.

[7] Ackert, J., Feldmann, F. and Rott, N., "Investigations of Compression Shocks and Boundary Layers in Gases Moving at High Speed," NACA TM 1113, Washington, D.C., January 1947.

[8] Gadd, G. E., Holder, D. W., and Regan, J. D., "An Experimental Investigation of the Interaction Between Shock Waves and Boundary Layers," *Proc. Roy. Soc.* Series A, Vol. 226, pp. 227-253, 1954.

[9] Gadd, G. E., "Interactions Between Normal Shock Waves and Turbulent Boundary Layers," A.R.C. 22559, R & M 3262, 1961.

[10] Chapman, D.R., Kuehn, D.M., and Larson, H.K., "Investigation of Separated Flows in Supersonic and Subsonic Streams with Emphasis of the Effect of Transition," NACA Rept. 1356, 1958.

[11] Green, J.E., "Interactions Between Shock Waves and Turbulent Boundary Layers," Royal Aircraft Establishment Technical Report 69098, May 1969.

[12] Vidal, R.J., Wittliff, C.E., Catlin, P.A. and Sheen, B.H., "Reynolds Number Effects on the Shock Wave/Turbulent Boundary Layer Interaction at Transonic Speeds," AIAA Paper No. 73-661, 6th Fluid and Plasma Dynamics Conference, Palm Springs, California, July 1973.

[13] Loving, D.L., "Wind-Tunnel-Flight Correlation of Shock Induced Separated Flow," NASA TN-D-3580, September, 1966.

[14] LeBlanc, R. and Goethals, R., "Study of Normal Shock Wave Turbulent Boundary Layer Interaction Phenomena in View of Application to Transonic Turbomachines," NASA Technical Translation F-16698, Washington, D.C., December 1975.

[15] East, L.F., "Application of a Laser Anemometer to the Investigation of Shock Wave Boundary Layer Interactions," RAE Technical Memorandum Aero. 1666, February, 1976 and AGARD CP-193, *Applications of Non-Intrusive Instrumentation in Fluid Flow Research*, September, 1976.

[16] Abbiss, J.B., East, L.F., Nash, C., Parker, P., Pike, P. and Sawyer, W.G., "A Study of the Interaction of a Normal Shock Wave and a Turbulent Boundary Layer Using a Laser Anemometer," RAE Technical Report 75141, December 1975.

[17] Mateer, G.G., Brosh, A. and Viegas, J.R., "A Normal Shock Wave Turbulent Boundary Layer Interaction at Transonic Speeds," AIAA Paper No. 76-161, January 1976.

[18] Bruce, W., "The U.S. National Transonic Facility," AGARD Report No. 722 Parts 1 and 2, 1985.

[19] Mateer, G.G. and Viegas, J.R., "Effect of Mach Number and Reynolds Number on a Normal Shock Wave/Turbulent Boundary Layer Interaction," AIAA Paper No. 79-1502, 1979.

[20] Mateer, G.G. and Viegas, J.R., "Mach and Reynolds Number Effects on a Shock-Wave Boundary Layer Interaction," *AIAA Journal*, Vol. 18, No. 8, August 1980, pp. 1016-1018.

[21] Kooi, J.W., "Experiment on Transonic Shock Wave Boundary Layer Interaction," AGARD CP-168, *Flow Separation*, Nov. 1975.

[22] Om, D., Childs, M.E. and Viegas, J.R., "An Experimental Investigation and Numerical Prediction of a Transonic Normal Shock/Wave Turbulent Boundary Layer Interaction," AIAA Paper No. 82-0990, 1982.

[23] Délery, J.M., "Experimental Investigation of Turbulence Properties in Transonic Shock/Boundary Layer Interactions," *AIAA Journal*, February 1983, pp. 180-185.

[24] Sajben, M., Morris, M.J., Bogar, T.J. and Kroutil, J.C., "Confined Normal Shock/Turbulent Boundary Layer Interaction Followed by an Adverse Pressure Gradient," AIAA Paper No. 89-0354, Jan. 1989.

[25] Morris, N.J., Sajben, M. and Kroutil, J.C., "Experimental Investigation of Normal Shock/Turbulent Boundary Layer Interactions With and Without Mass Removal," To be Presented at AIAA 28th Aerospace Sciences Meeting, Reno, NV Jan. 1990.

[26] Lian, X. and Jiang, P., "The Interaction Between a Normal Shock and a Turbulent Boundary Layer in Transonic Flow Over a Curved Wall," *Acta Aerodynamica Sinica*, Vol. 6, June, 1988, pp. 237-240.

[27] Velichko, S. A., and Lifshits, I. B., "The Interaction Between a Turbulent Boundary Layer and a Shock Wave at Transonic Flow Velocities," Akademiia Naak SSSR, Izvestiia, Mekhanika Zhidkosta i Gaza (ISSN 0568-5281), March-April 1983, pp. 32-38.

[28] Yeh, Y. and Cummins, H. Z., "Localized Fluid Flow Measurements with an He-Ne Laser Spectrometer," *Appl. Phys. Letters*, Vol. 4, p. 176.

[29] Schodl, R., "On the Extension of the Range of Applicability of LDA by Means of the Laser-Dual-Focus (L2F) Technique," Proceedings of the LDA Symposium at Copenhagen, 1975, pp. 480-489.

[30] Schodl, R., "A Laser-Two-Focus (L2F) Velocimeter for Automatic Flow Vector Measurements in the Rotating Components of Turbomachines," *ASME Journal of Fluids Engineering*, Vol. 102, December, 1980, pp. 412-419.

[31] Schodl, R., "Laser Two Focus Velocimetry," AGARD CP-399, Advanced Instrumentation for Aero Engine Components, 1986.

[32] Mayo, W.T., Woodward, R.P., Boland, A., and Smart, A.E., "Correlex: A Multiplexed Correlation Processor," Proceedings from the 4th International Conference of Photon Correlation Techniques in Fluid Mechanics, Stanford University, Stanford, CA, August 25-27, 1980.

[33] Strazisar, A.J., The Fluid Dynamics of Turbomachinery, Lecture No. 18, ASME Advanced Short Course presented by the ASME Turbomachinery Institute, July, 21-31, 1986.

[34] Nichols, C. E., Jr., "Preparation of Polystyrene Microspheres For Laser Velocimetry in Wind Tunnels," NASA TM-89163, June, 1987.

[35] Yanta, W.J., "Measurements of Aerosol Size Distributions with a Laser-Doppler Velocimeter," National Bureau of Standards Special Publication 412, May 1974.

[36] Yanta, W.J., Gates, D.F., and Brown, F.W., "The Use of a Laser Doppler Velocimeter in Supersonic Flow," Naval Ordnance Laboratory, NOLTR 71-169, August, 1971.

[37] Maxwell, B.R. and Seasholtz, R.G., "Velocity Lag of Solid Particles in Oscillating Gases and in Gases Passing Through Shock Waves," NASA TN D-7490, March 1974.

[38] Carlson, D.J. and Hoglund, R.F., "Particle Drag and Heat Transfer in Rocket Nozzles," *AIAA Journal*, Vol. 2, No. 11, November, 1964, pp. 1980-1983.

[39] Feller, W.V. and Meyers, J.F., "Development of a Controllable Particle Generator for LV Seeding in Hypersonic Wind Tunnels," Presented at the University of Minnesota Symposium on Laser Anemometry, Oct. 22-24, 1975.

[40] von Stein, H.D. and Pfeifer, H.J., "Investigation of the Velocity Relaxation of Micron Sized Particles in Shock Waves Using Laser Radiation," *Applied Optics*, Vol. 11, No. 2, February 1972.

[41] Meyers, J.F. and Walsh, M.J., "Computer Simulation of a Fringe Type Laser Velocimeter," Second International Workshop on Laser Velocimetry, Purdue University, 1974.

[42] Adrian, R.J., "Estimation of LDA Signal Strength and Signal-to-Noise Ratio," *TSI, Quarterly*, February/March, 1978.

[43] Liu, B.Y.H., Whitby, K.T. and Yu, H.H.S., "A Condensation Aerosol Generator for Producing Monodisperse Aerosols in the Size Range $0.036\mu m$ to $1.3\mu m$," *Journal de Recerches Atmospheriques*, 1966.

[44] Yanta, W.J., "The Use of the Laser Doppler Velocimeter in Aerodynamic Facilities," AIAA Paper No. 80-0435-CP, March 1980.

[45] Chriss, R.M., Keith, T.G. and Hingst, W.R., "An Evaporation-Condensation Aerosol Generator for LDA Seeding in a Supersonic Wind Tunnel," *Particulate and Multiphase Processes*, ed. Arimen, T. and Veziroglu, T., Vol. 2, p. 347.

[46] McLaughlin, D.K., and Teidermann, W.G., "Biasing Correction for Individual Realization of Laser Anemometer Measurements in Turbulent Flows," *The Physics of Fluids*, Vol. 16, No. 12, December, 1973, pp. 2082-2088.

[47] Edwards, R.V., editor, "Report of the Special Panel on Statistical Particle Bias Problems in Laser Anemometry," *Journal of Fluids Engineering*, Vol. 109, No. 2, June, 1987, pp. 89-93.

[48] Barnett, D.O., and Bentley, H.T., "Bias of Individual Realization Laser Anemometers," Proceedings of the Second International Workshop on Laser Velocimetry, Purdue University, Vol. 1, March 1974.

[49] Stevenson, W.H., Thompson, H.D., and Roesler, T.C., "Direct Measurement of Laser Velocimeter Bias Errors in a Turbulent Flow," *AIAA Journal*, Vol. 20, No. 12, December, 1982, pp. 1720-1723.

[50] Johnson, D.A., Modarress, D., and Owen, F.K., "An Experimental Verification of Laser Velocimeter Sampling Bias and its Correction," International Symposium on Applications of Laser Anemometry to Fluid Mechanics, Lisbon Portugal, July, 1988.

[51] Edwards, R.V. and Jensen, A.S., " Particle Sampling Statistics in Laser Anemometers: Sample and Hold Systems and Saturable Systems," *Journal of Fluid Mechanics*, Vol. 133, 1983,pp. 397-411.

[52] Durão, D.F.G., Laker, J., and Whitelaw, J.H., "Bias Effects in Laser Anemometry," *J. Phys. E:Sci. Instrum.*, Vol. 13, 1980, pp. 442-445.

[53] Durão, D.F.G., and Whitelaw, J.H., "Relationship Between Velocity and Signal Quality in Laser Doppler Anemometry," *J. Phys. E: Sci. Instrum.*, Vol. 12, 1979, p. 47.

[54] Buchave, P., "The Measurement of Turbulence with the Burst Type Laser Doppler Anemometer–Errors and Correction Methods," Report TRL-106, State University of New York at Buffalo, 1979.

[55] Dimotakis, P.E., "Single Scattering Particle Laser Doppler Measurements of Turbulence," *Applications of Non-Intrusive Instrumentation in Fluid Flow Measurement*, AGARD CP-193, 1976.

[56] Adrian, R.J. and Yao, Y.S., "Power Spectra of Fluid Velocities Measured by Laser Doppler Velocimetry," Experiments in Fluids, Vol. 5, 1987.

[57] Erdmann, J.C. and Tropea, C., "Turbulence Induced Statistical Bias in Laser Anemometry," *Proceedings of the Seventh Symposium on Turbulence*, University of Missouri-Rolla, September, 1981.

[58] Quigley, M. and Teidermann, W., "Experimental Evaluation of Sampling Bias in Individual Realization Laser Anemometry," *AIAA Journal*, Vol. 15, February, 1977, pp. 266-268.

[59] Bogard, D. and Teidermann, W., "Experimental Evaluation of Sampling Bias in Naturally Seeded Flows," *Laser Velocimetry and Particle Sizing*, Hemisphere Publishing Corp., Washington, D.C., 1979.

[60] TSI, Inc. Aerodynamic Particle Sizer Instruction Manual.

[61] TSI, Inc. Model 1990B Counter Signal Processor Instruction Manual.

[62] Snyder, P.K., Orloff, K.L. and Reinath, M.S., "Reduction of Flow Measurement Uncertainties in Laser Velocimeters with Non-Orthogonal Channels," *AIAA Journal*, Vol. 22, August 1984.

[63] ASME Committee MFFCC SCI, "Fluid Flow Measurement Uncertainty; Draft of 26 March, 1980," ASME, Codes and Standards Dept.

[64] Schenck, H., *Theories of Engineering Experimentation*, McGraw-Hill, 1968.

[65] Kline, S.J. and McClintock, F.A., "Describing Uncertainties in Single-Sample Experiments," *Mechanical Engineering*, Jan. 1953.

[66] Moffat, R.J., "Contributions to the Theory of Single-Sample Uncertainty Analysis," *Journal of Fluids Engineering*, June, 1982.

[67] National Bureau of Standards Postscript to Special Publication 300, NBS Communication Manual for Scientific and Public Information, Nov., 1980.

[68] Orloff, K.L. and Snyder, P.K., "Laser-Doppler Anemometer Measurements Using Non-Orthogonal Velocity Components: Error Estimates," *Applied Optics*, Vol. 21, January 1982.

[69] Chapman, G.T., "Topological Classification of Flow Separation on Three-Dimensional Bodies," AIAA Paper No. 86-0485, January, 1986.

[70] Peake, D.J., and Tobak, M., ed. *Three-Dimensional Interactions and Vortical Flows with Emphasis on High Speeds*, AGARD No. 252, July, 1980.

[71] Délery, J. and Marvin, J.G., ed., *Shock Wave Boundary Layer Interactions*, AGARDograph No. 280, February, 1986.

[72] Meyers, J.F., Private communication.

[73] Neti, S. and Clark, W., "On-Axis Velocity Component Measurement with Laser Velocimeters," *AIAA Journal*, Vol. 17, No. 9, September 1979, pp. 1013-1015.

[74] Delery, J., ed., *Turbulent Shear-Layer/Shock Wave Interactions*, Symposium of the International Union of Theoretical and Applied Mechanics, Palaiseau, France September 9-12, 1985.

[75] *International Symposium on Applications of Laser-Doppler Anemometry to Fluid Mechanics*, Lisbon, Portugal, July 5-7, 1982.

[76] Klemm, W.J., *A Prediction of the Interaction of a Normal Shock Wave with a Separating, Turbulent Boundary Layer*, Ph.D. Dissertation, Dartmouth College, 1978.

[77] Mathews, Childs and Paynter, "Use of Coles' Universal Wake Function for Compressible Turbulent Boundary Layers," *Journal of Aircraft*, Vol. 7, No. 2, March-April 1970, pp. 137-140.
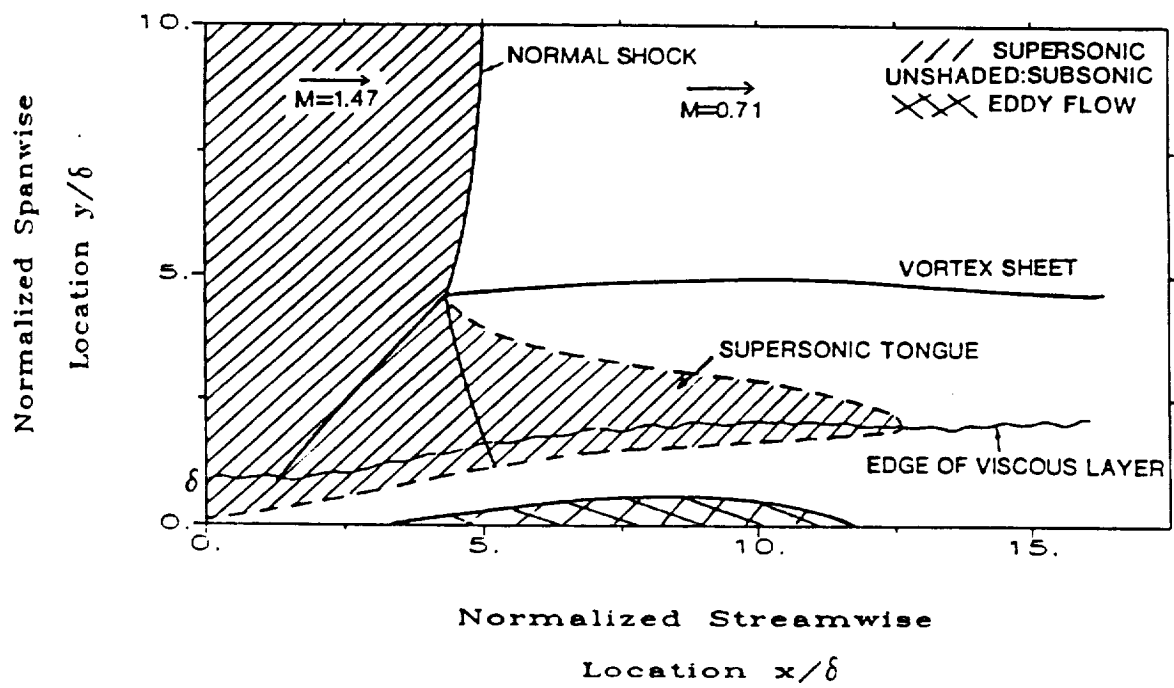
Figure 1: Seddon's Model of a Two-Dimensional Normal Shock Wave/Boundary Layer Interaction.

**Nozzle Block
(interchangeable)**

Test Section

Plenum

Diffuser
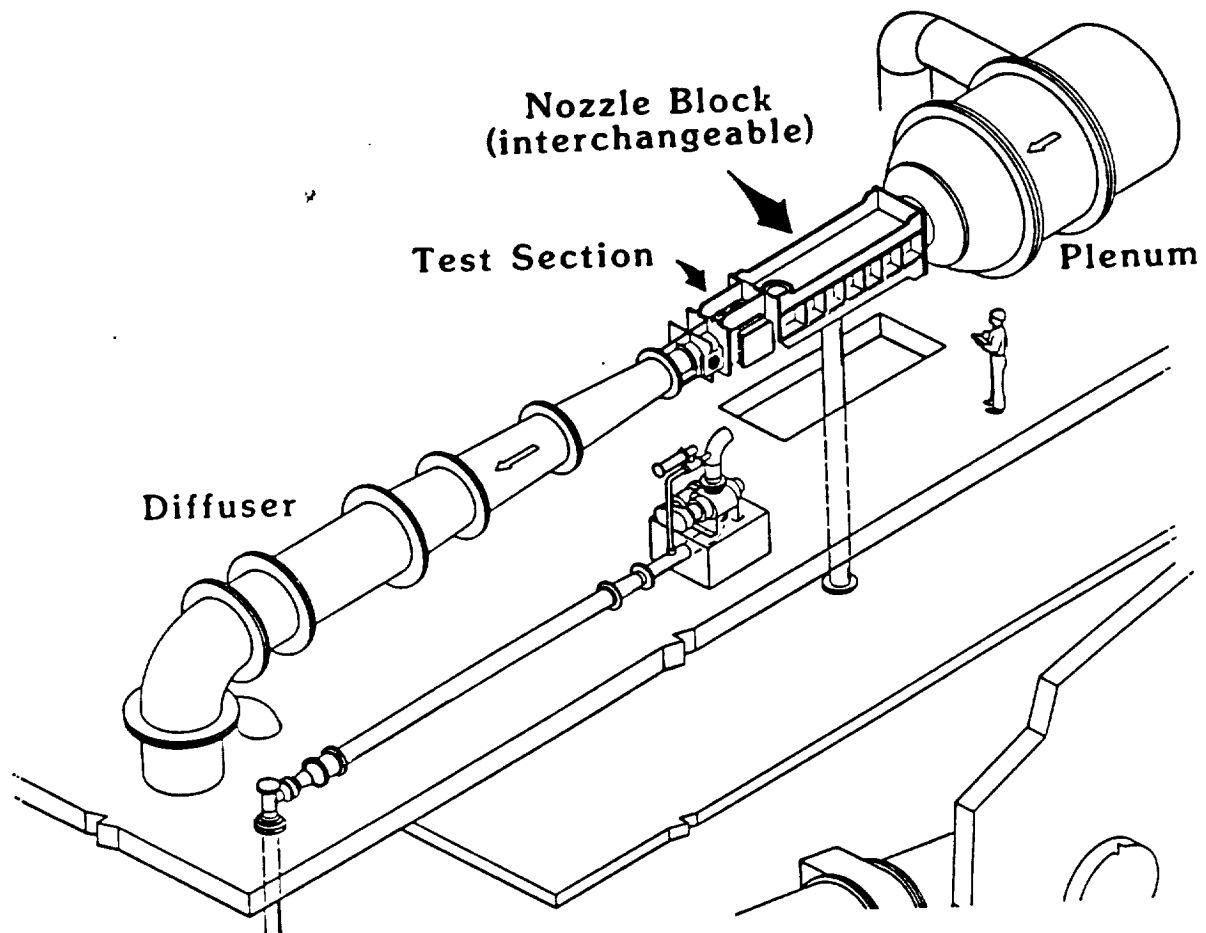
Figure 2: The Nasa Lewis Research Center's 1 ft by 1 ft Supersonic Wind Tunnel.
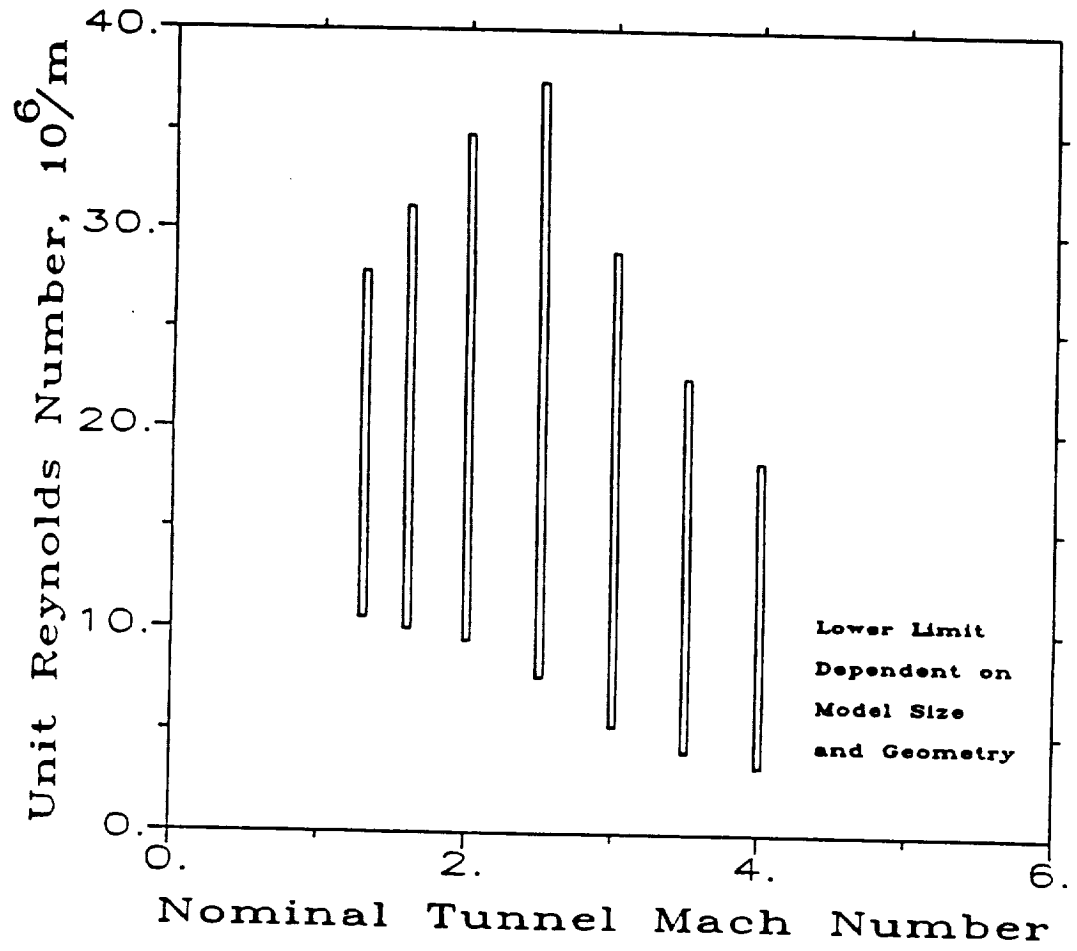
Figure 3: Reynolds Number Range for the 1 ft by 1 ft Supersonic Wind Tunnel.
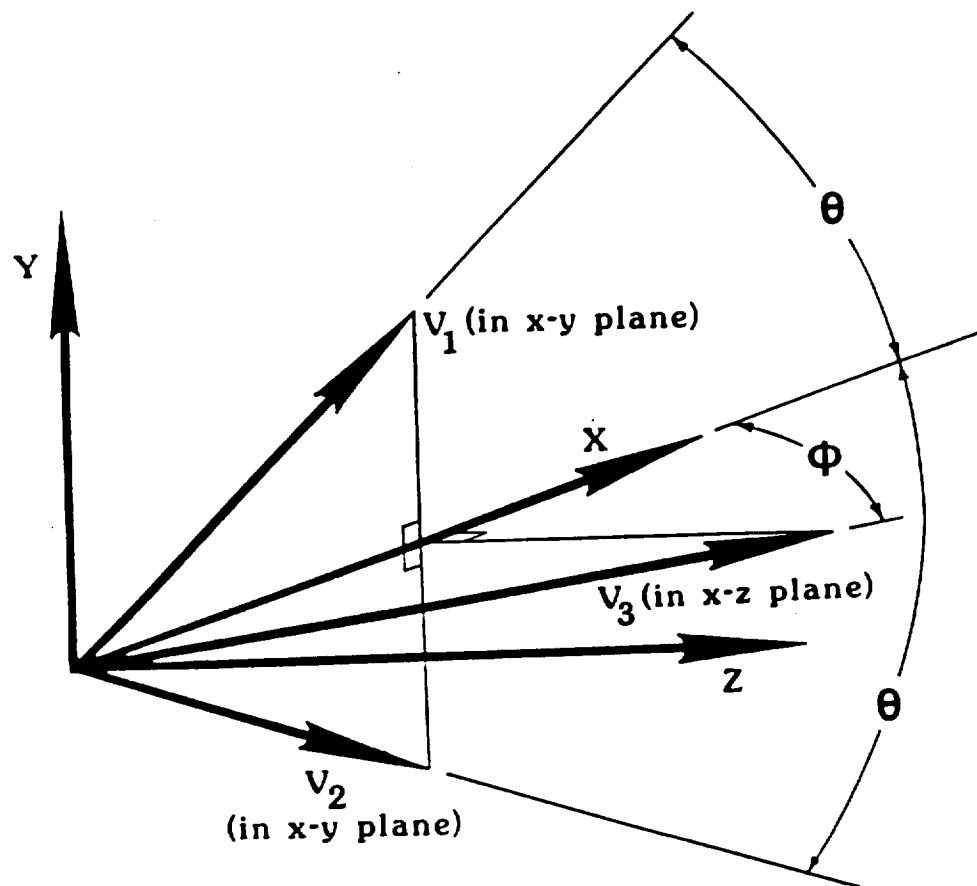
Figure 4: Non-Orthogonal Laser Velocimeter Coordinate System.
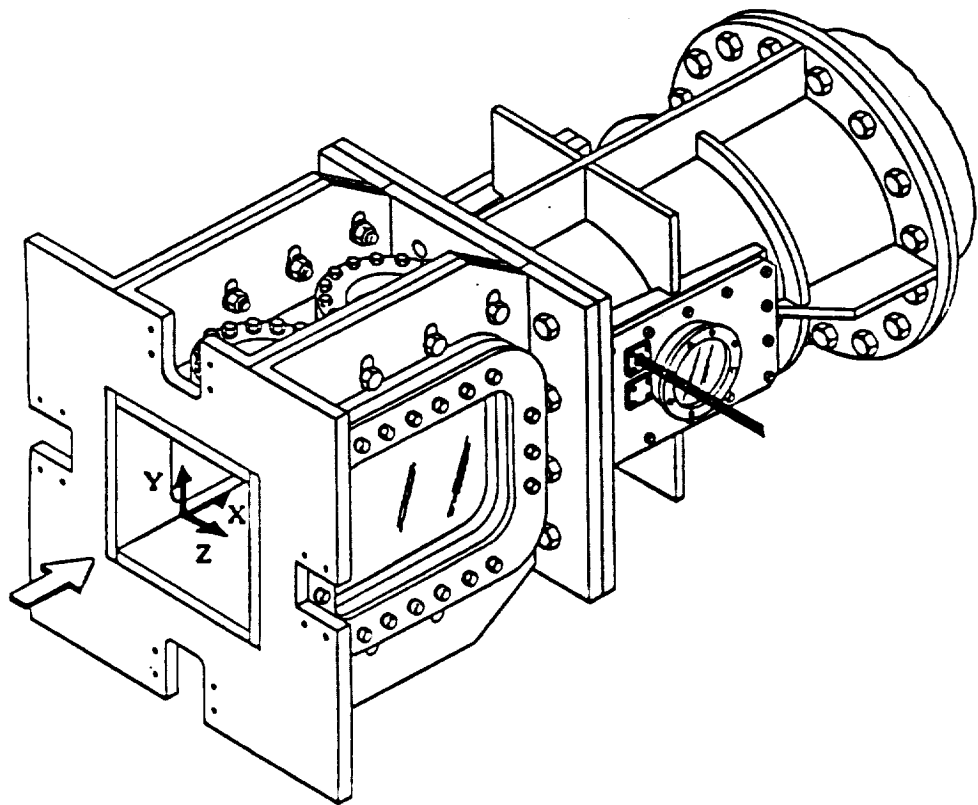
Figure 5: Test Section Coordinate System.
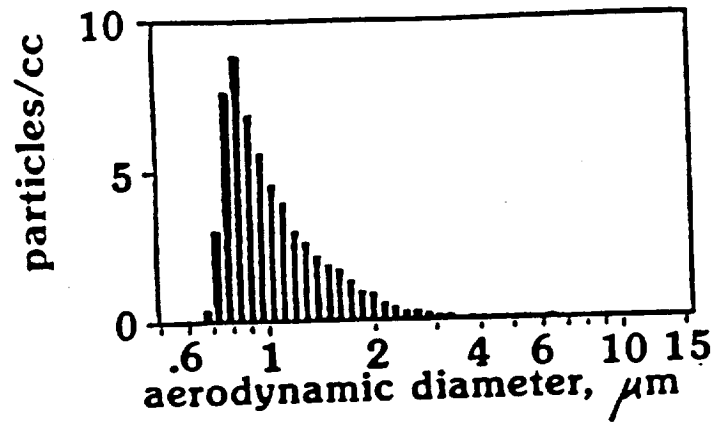
(a) Tunnel Ambient (no seed)
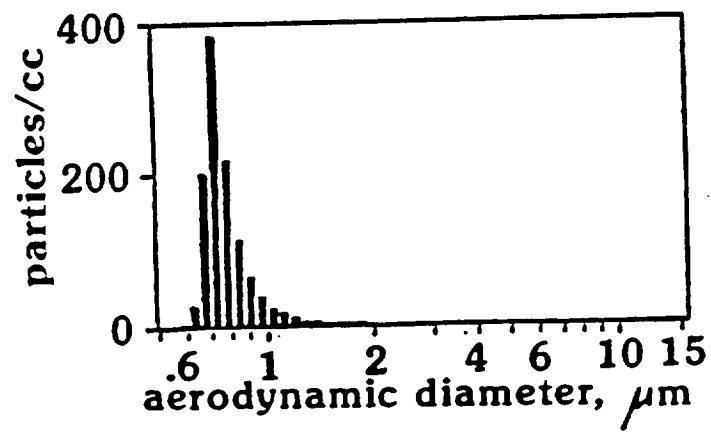
(b) With Seed Added

Figure 6: Test Section Aerosol Size Distribution.
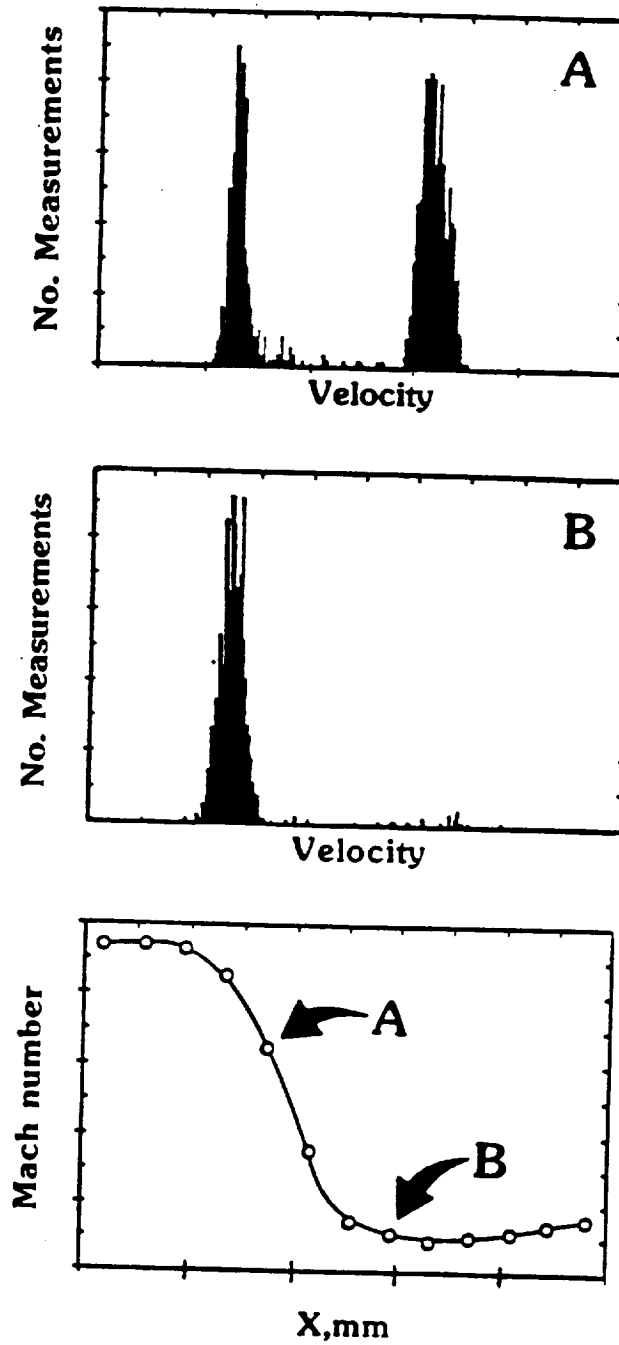
Figure 7: Laser Velocimeter Histograms Near the Shock Front; Mach 1.59.
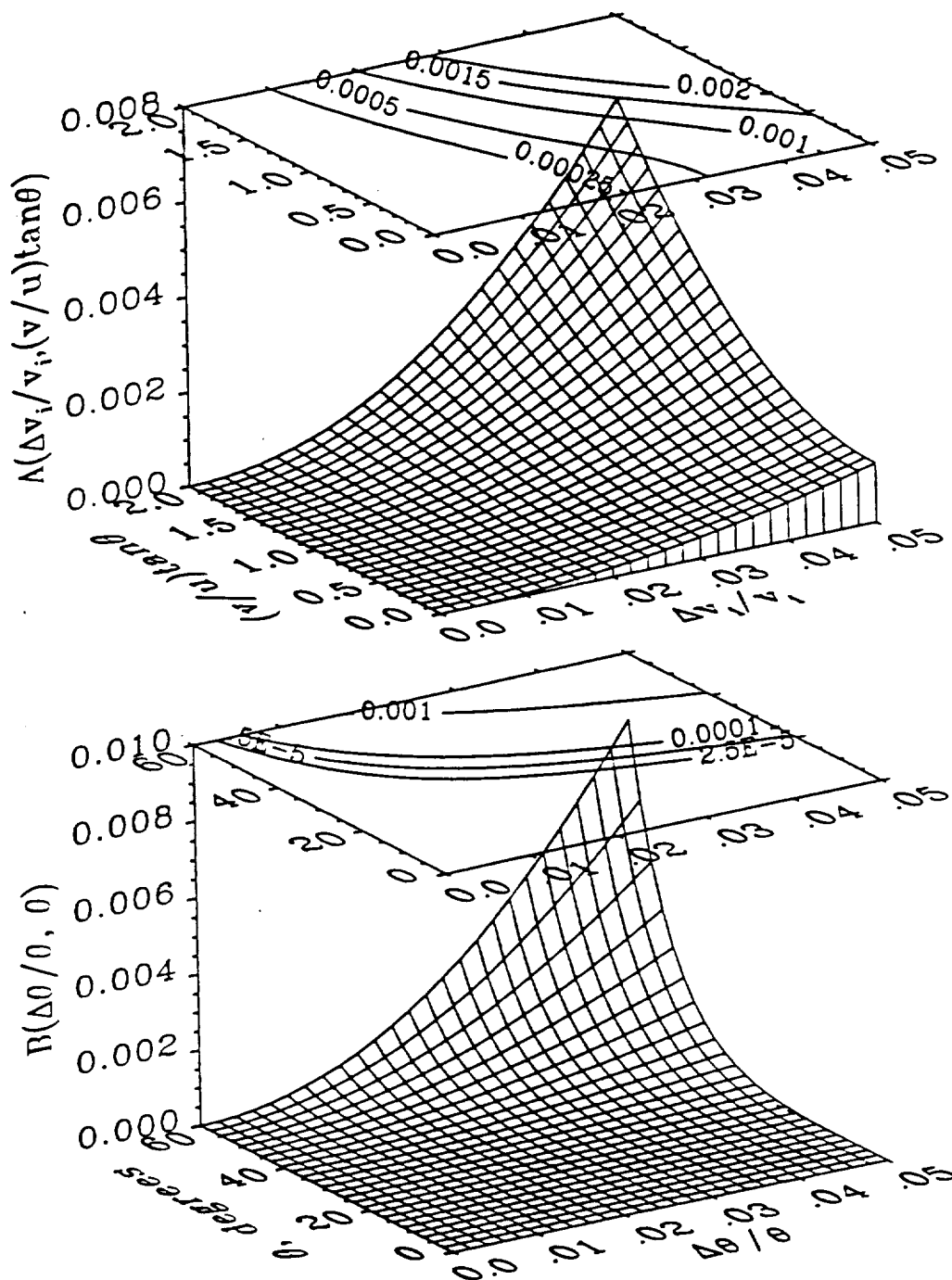
Figure 8: Parameters A and B to Determine $\Delta u/u$.
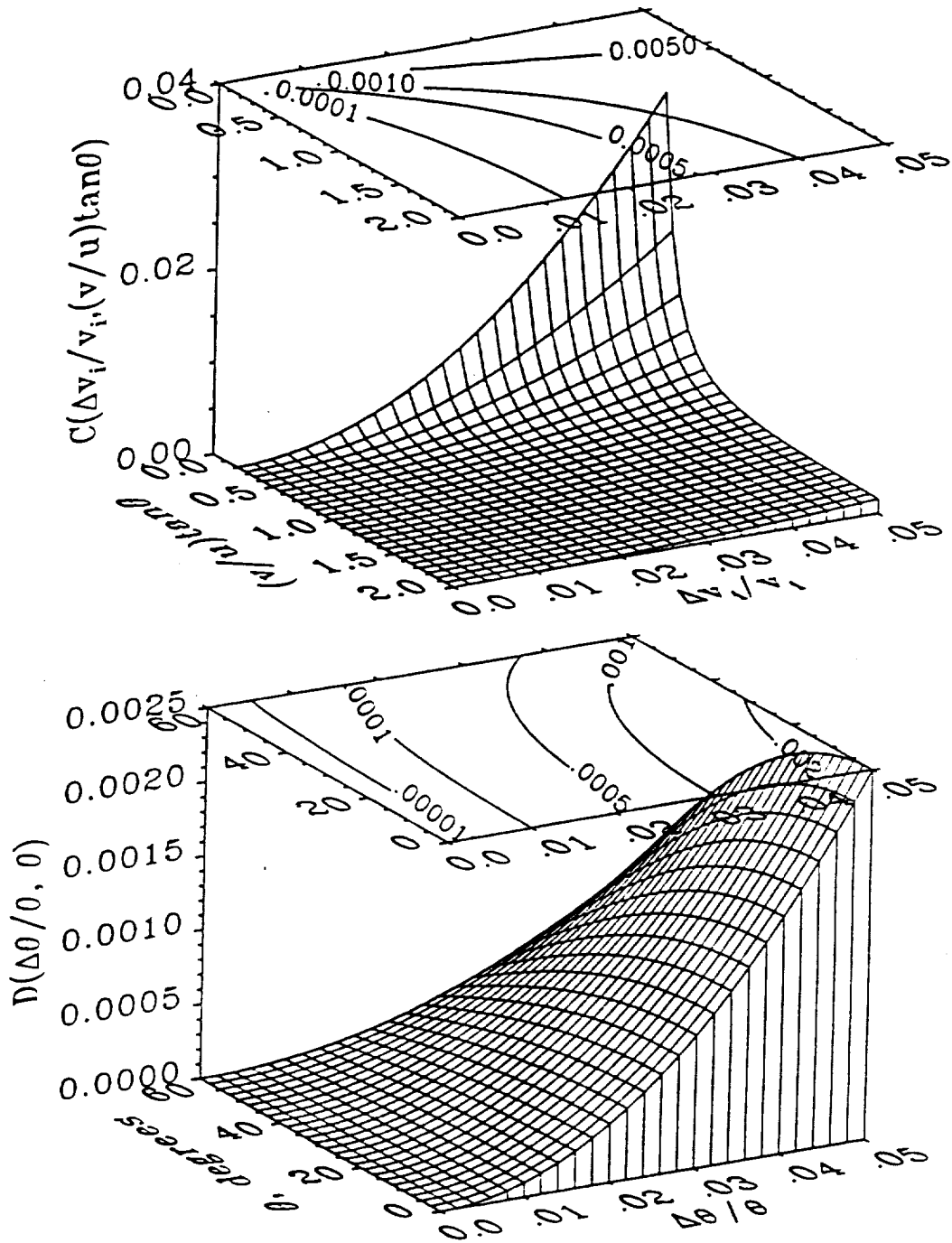
Figure 9: Parameters C and D to Determine $\Delta v/v$.
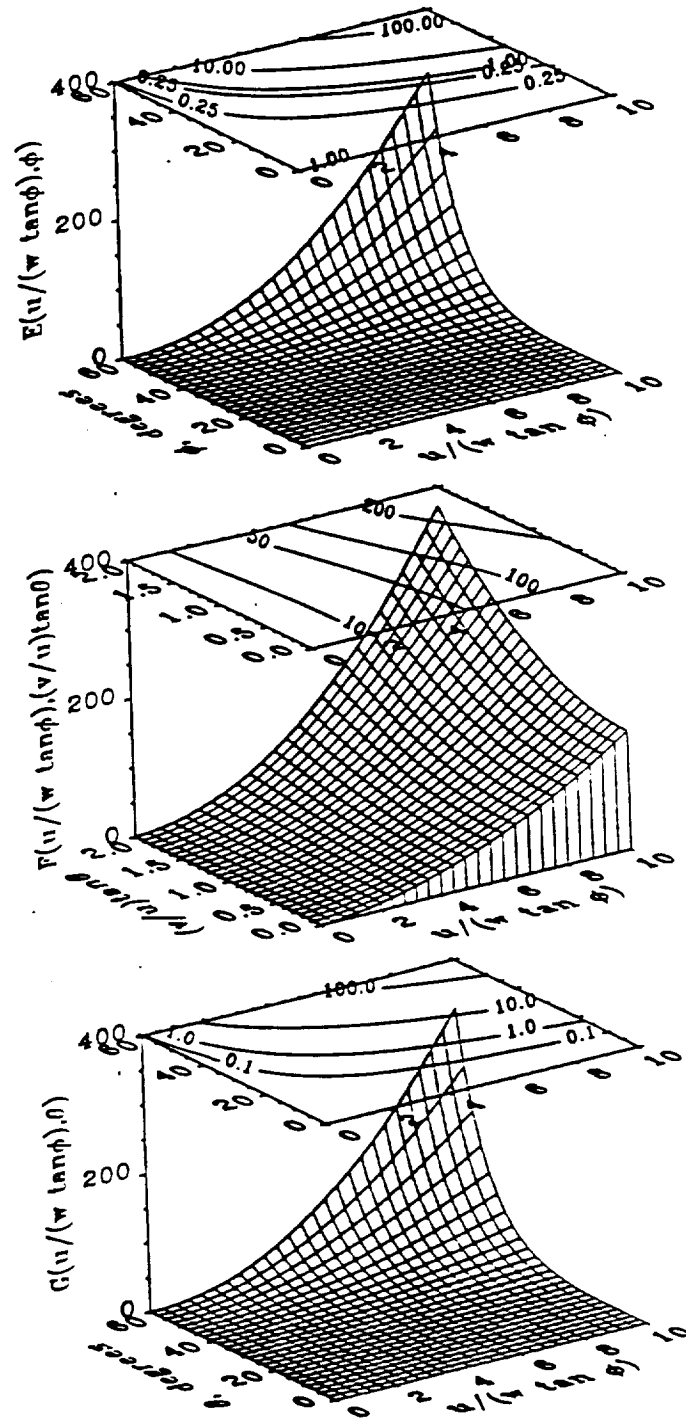
Figure 10: Parameters E, F and G to Determine $\Delta w/w$.
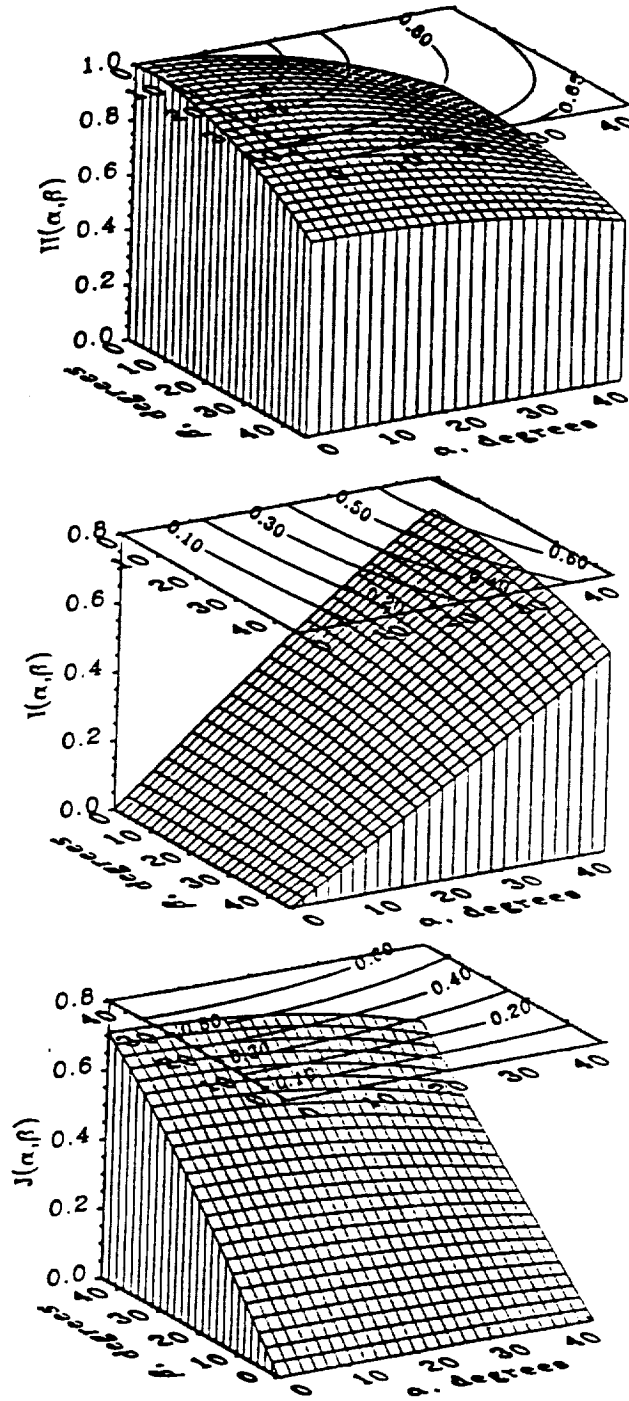
Figure 11: Parameters H. I and J to Determine $\Delta V/V$.
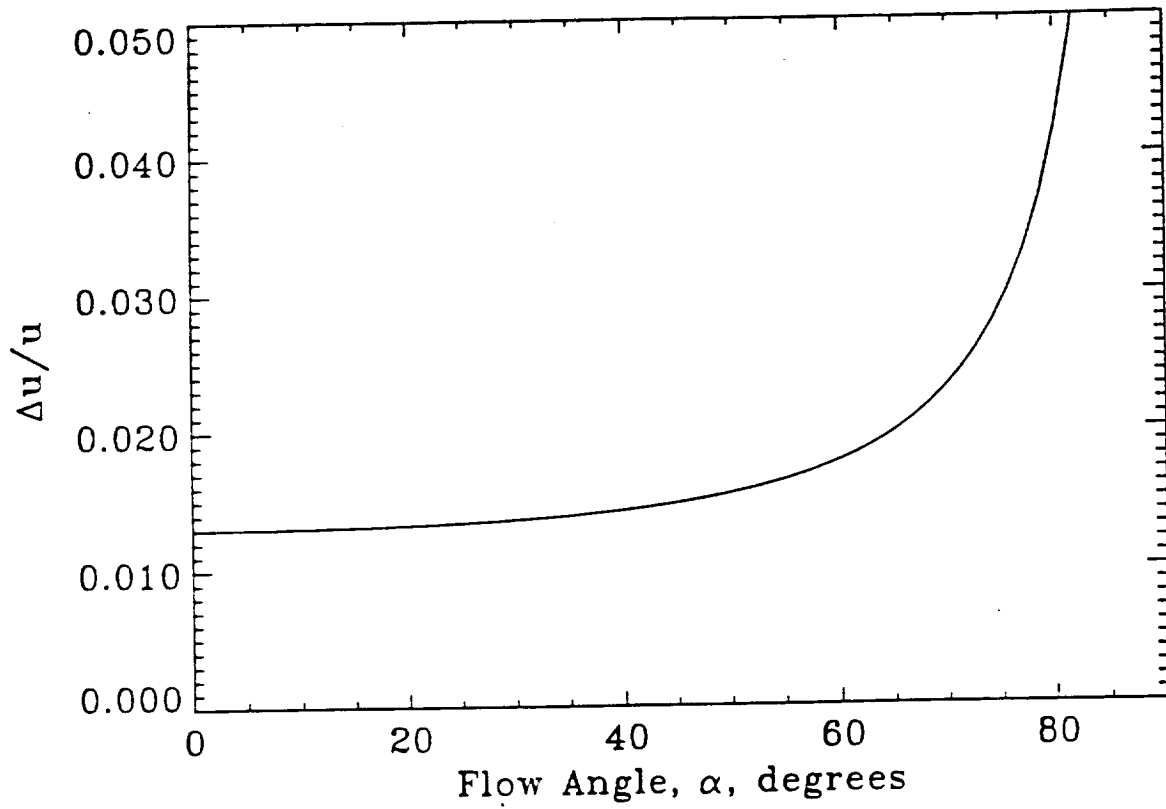
Figure 12: Uncertainty in u ($\theta = 30°$, $\Delta v_i / v_i = 1.7\%$, and $\Delta\theta/\theta = 1/60$).
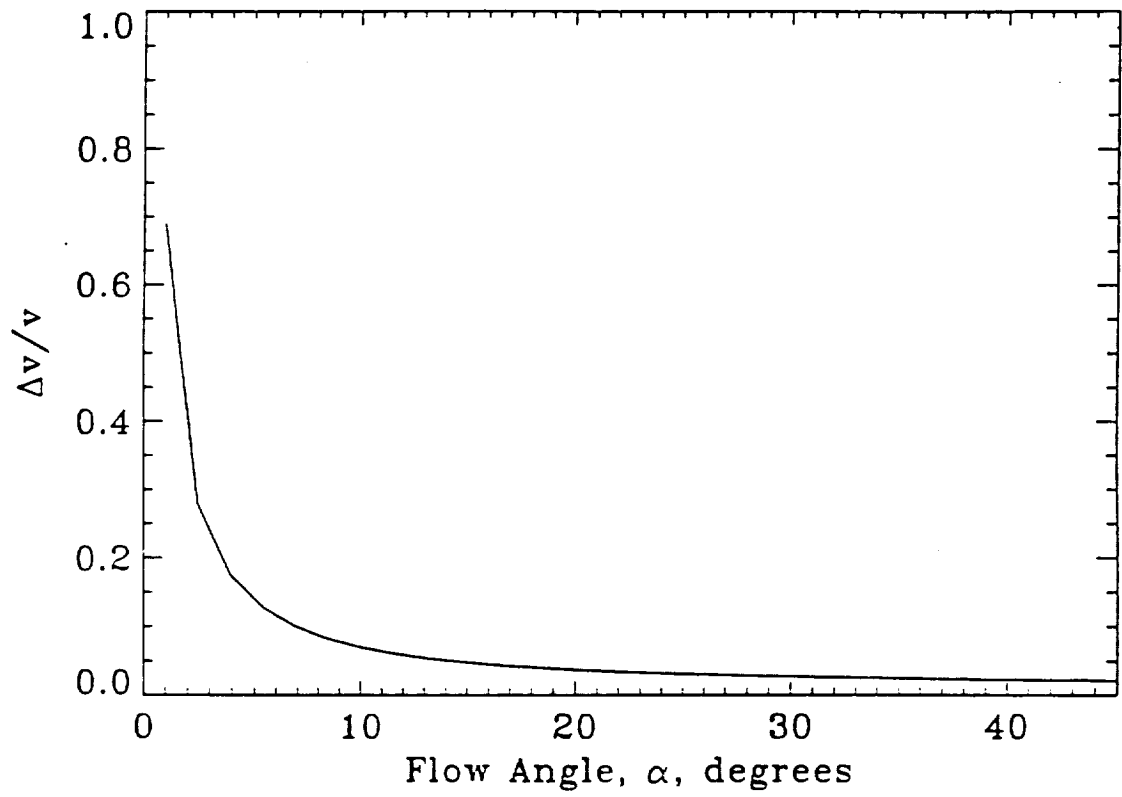
Figure 13: Uncertainty in v ($\theta = 30°$, $\Delta v_i/v_i = 1.7\%$, and $\Delta\theta/\theta = 1/60$).
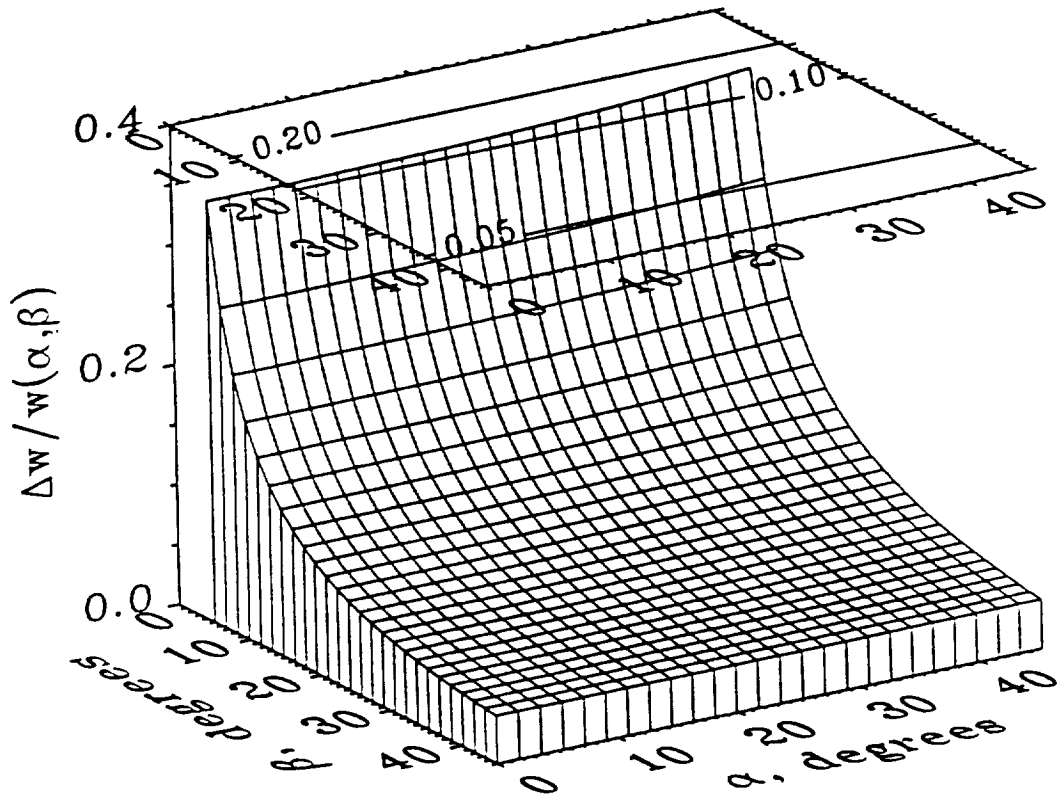
Figure 14: Uncertainty in w ($\theta = 30°$, $\phi = 29°$, $\Delta v_i/v_i = 1.3\%$, $\Delta\theta/\theta = 1/60$, and $\Delta\phi/\phi = 1/60$).
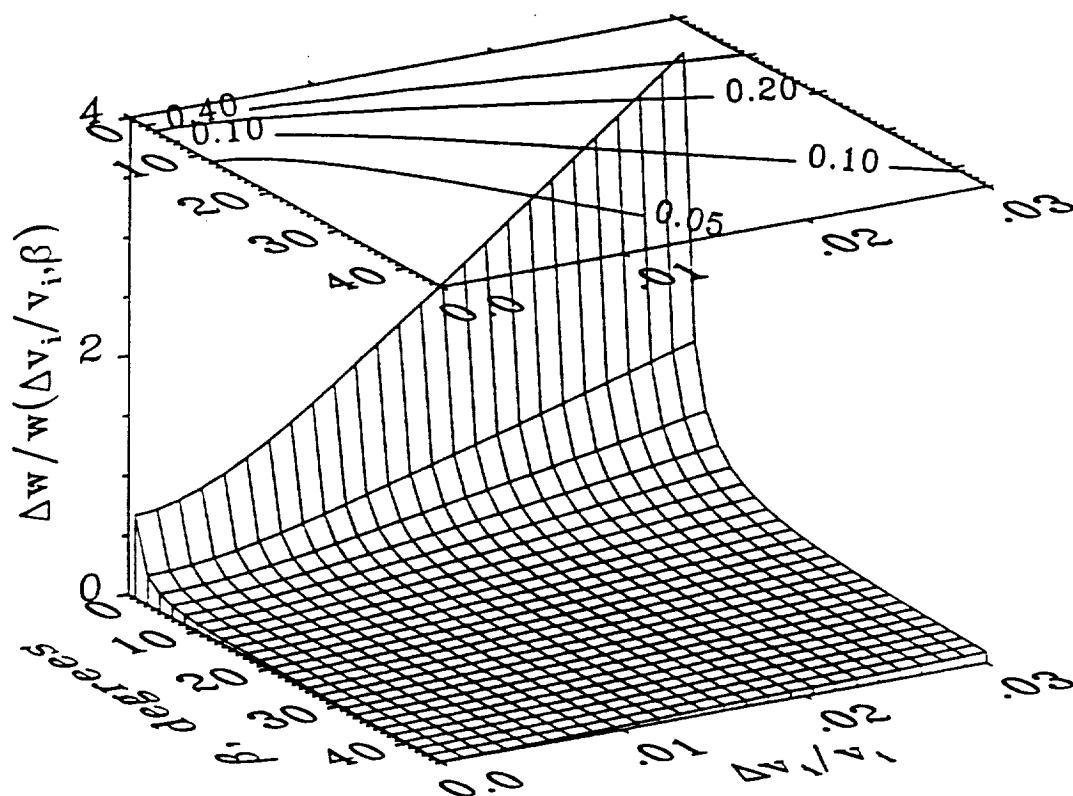
Figure 15: Uncertainty in w ($\alpha = 10°$, $\theta = 30°$, $\phi = 29°$, $\Delta\theta/\theta = 1/60$, and $\Delta\phi/\phi = 1/60$).
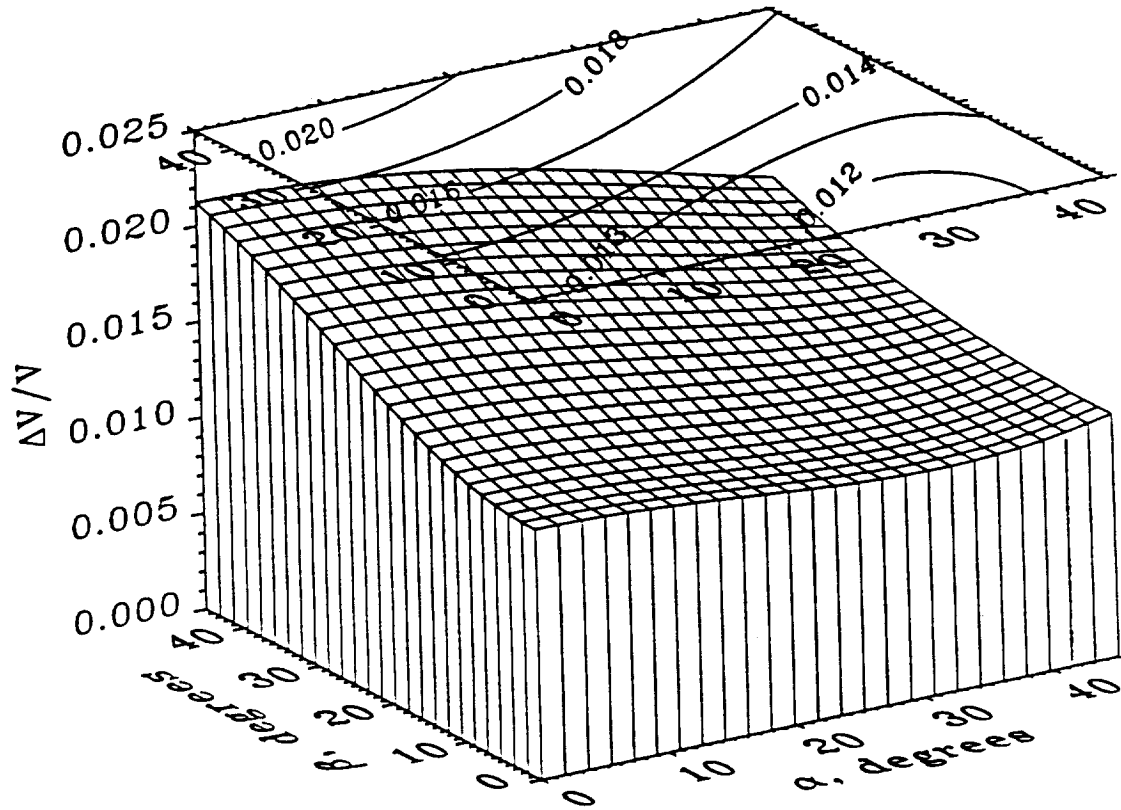
Figure 16: Uncertainty in V ($\theta = 30°$, $\phi = 29°$, $\Delta v_i / v_i = 1.3\%$ and 1.7%, $\Delta\theta/\theta = 1/60$, $\Delta\phi/\phi = 1/60$, and $\Delta T/T = 1/100$).
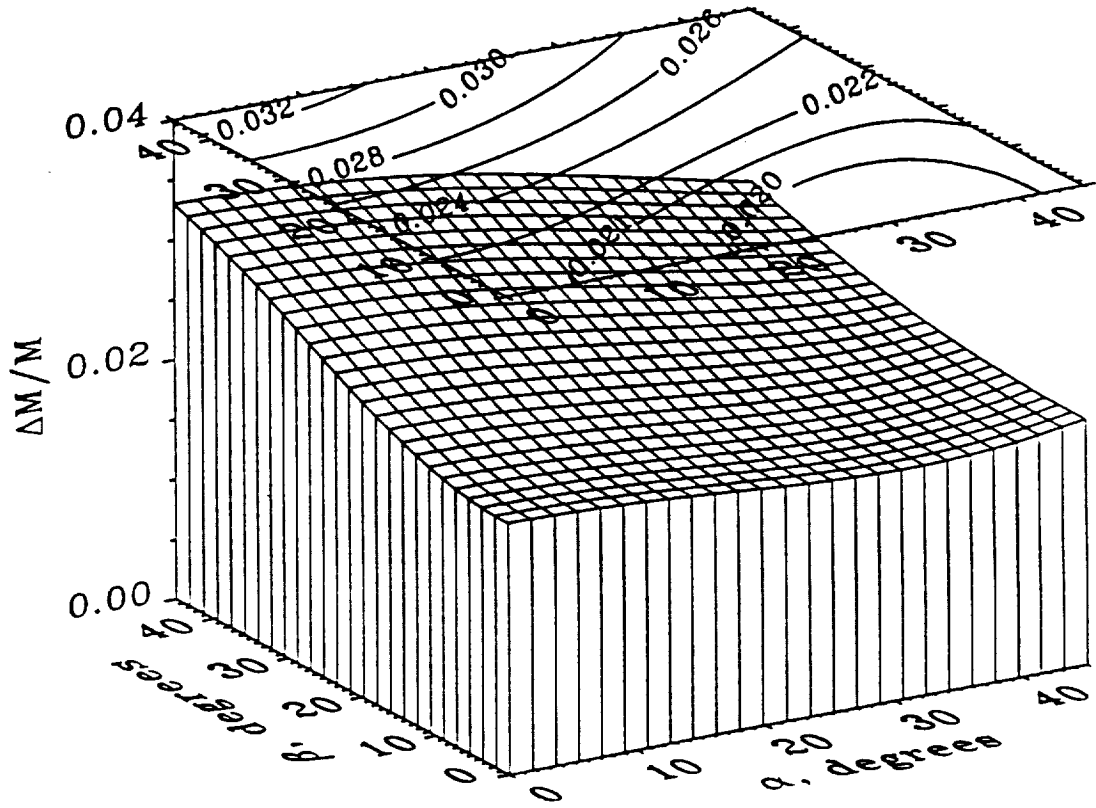
Figure 17: Uncertainty in Mach Number ($\theta = 30°$, $\phi = 29°$, $\Delta v_i/v_i = 1.3\%$ and 1.7%, $\Delta\theta/\theta = 1/60$, $\Delta\phi/\phi = 1/60$, and $\Delta T/T = 1/100$).
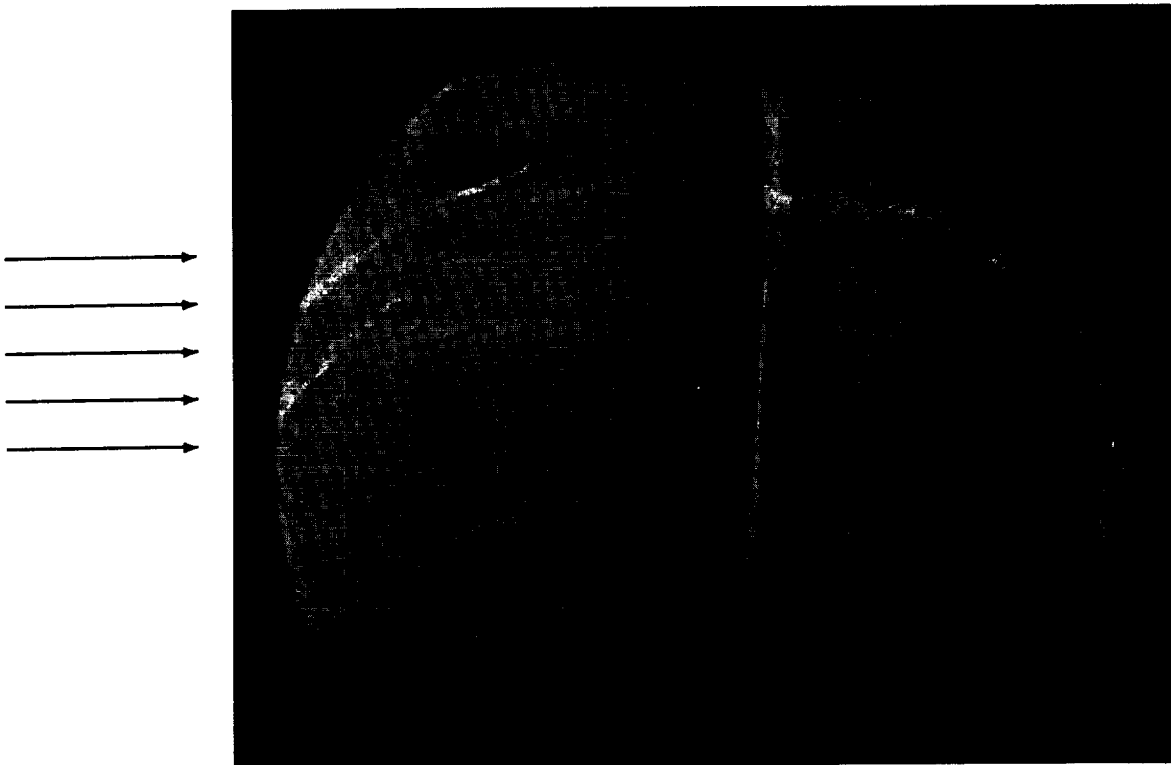
Figure 18: Schlieren Photograph; Mach 1.28. Flow left to right.
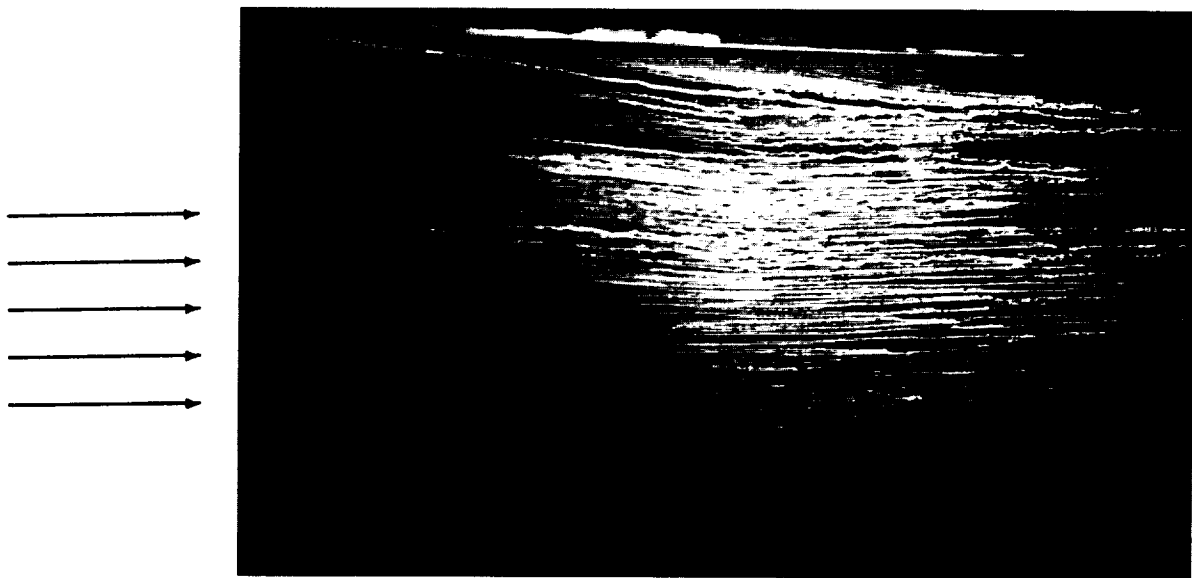
Figure 19: Surface Oil Flow Visualization Photograph; Mach 1.28.
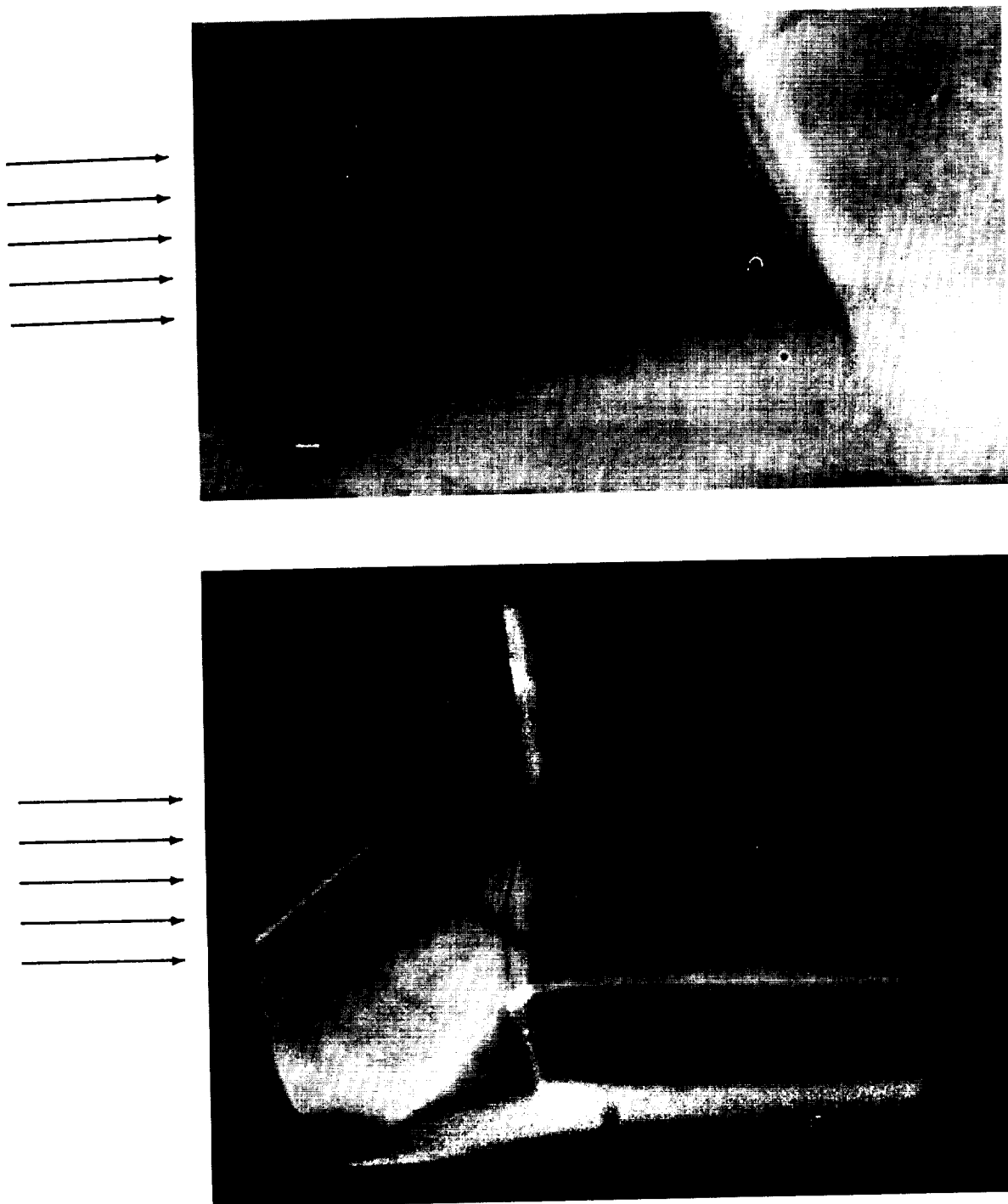
Figure 20: Schlieren Photographs; Overall and Closeup Views; Mach 1.59.
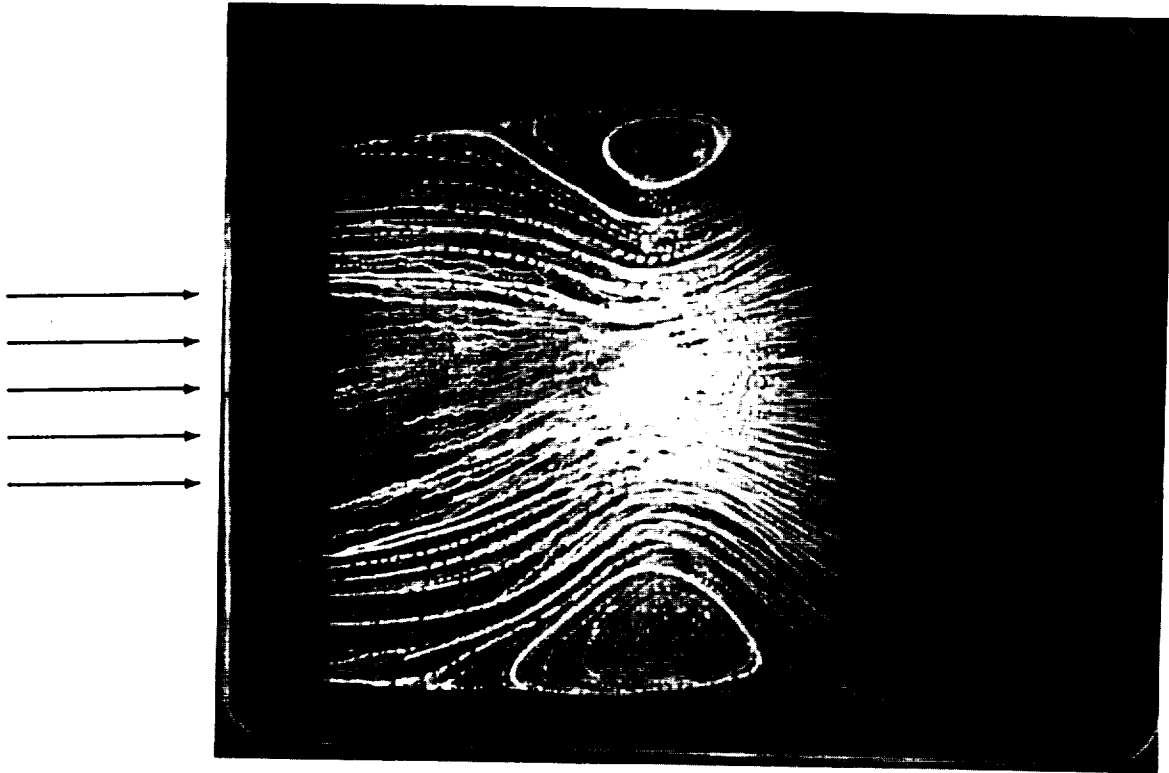
Figure 21: Surface Oil Flow Visualization Photograph; Mach 1.59.
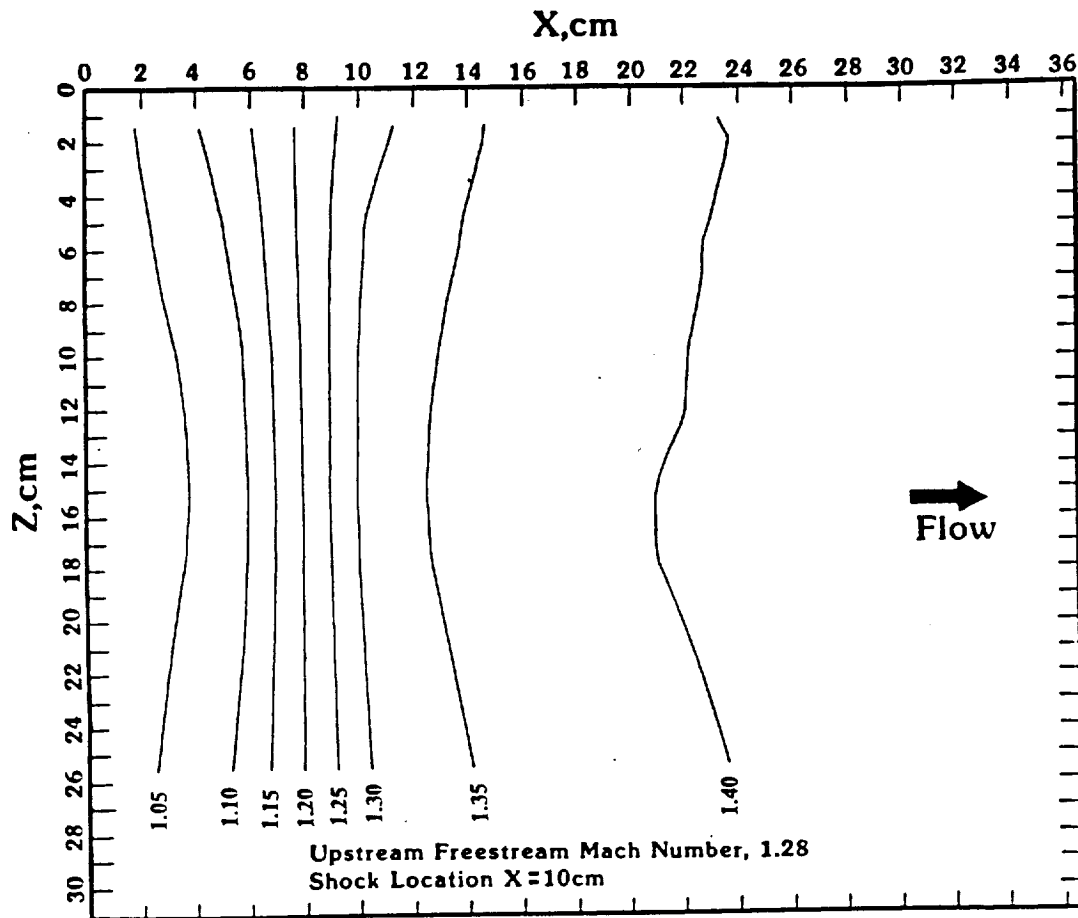
Figure 22: The Floor Static Pressure Distribution Normalized by the Upstream Static Pressure: Mach 1.28.
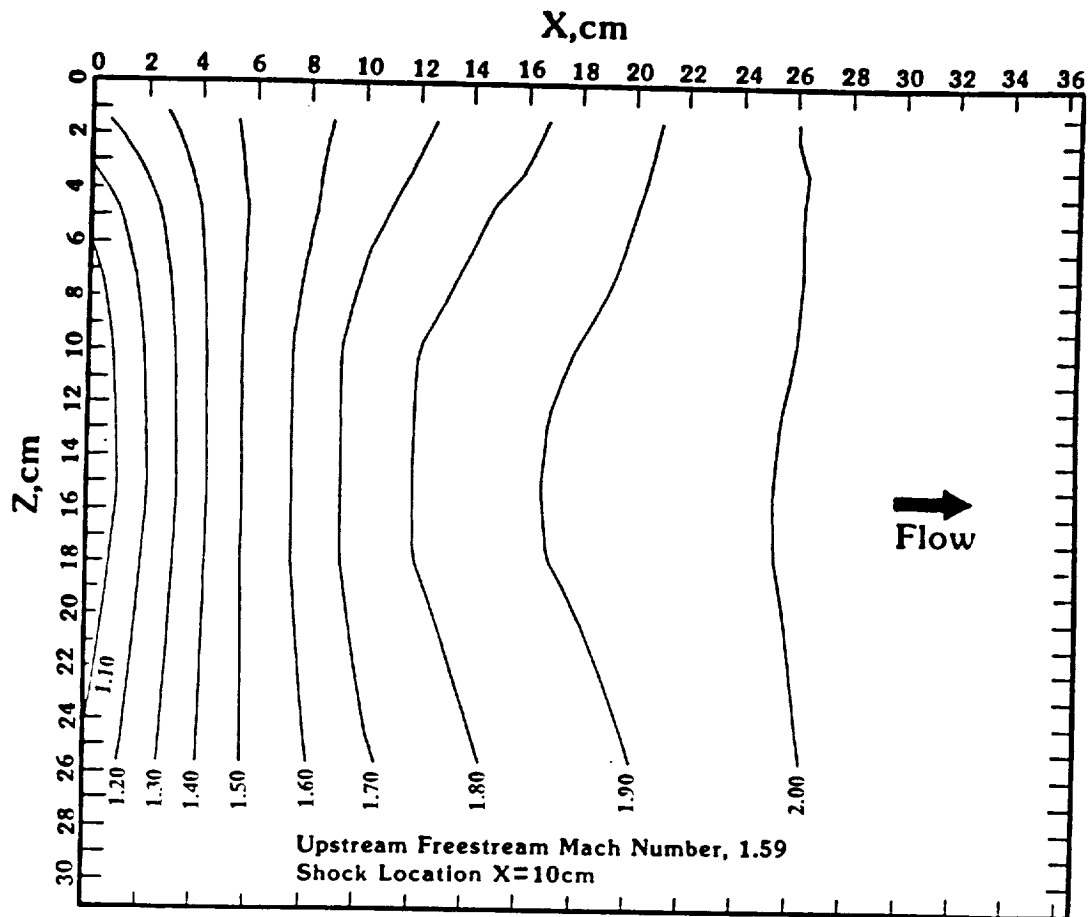
Figure 23: The Floor Static Pressure Distribution Normalized by the Upstream Static Pressure: Mach 1.59.
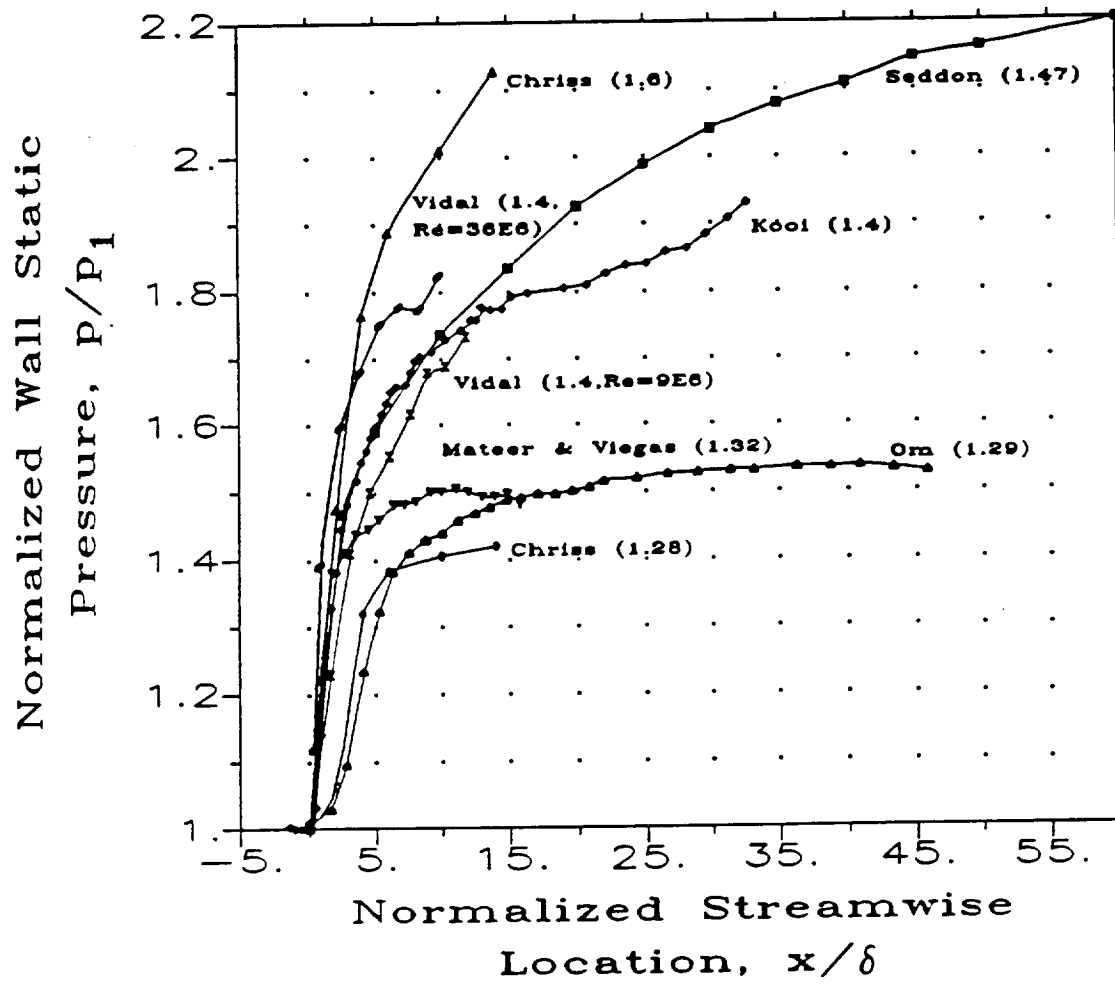
Figure 24: Comparison of Normalized Floor Static Pressure Distributions.
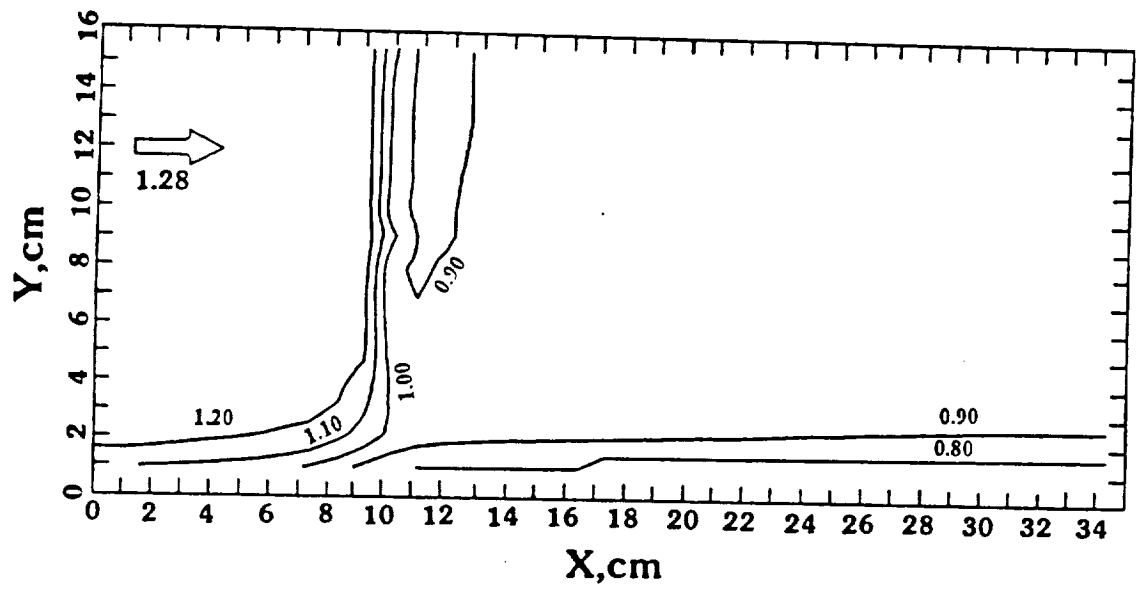
Figure 25: Mid-Span Mach Contour Plot; Mach 1.28.
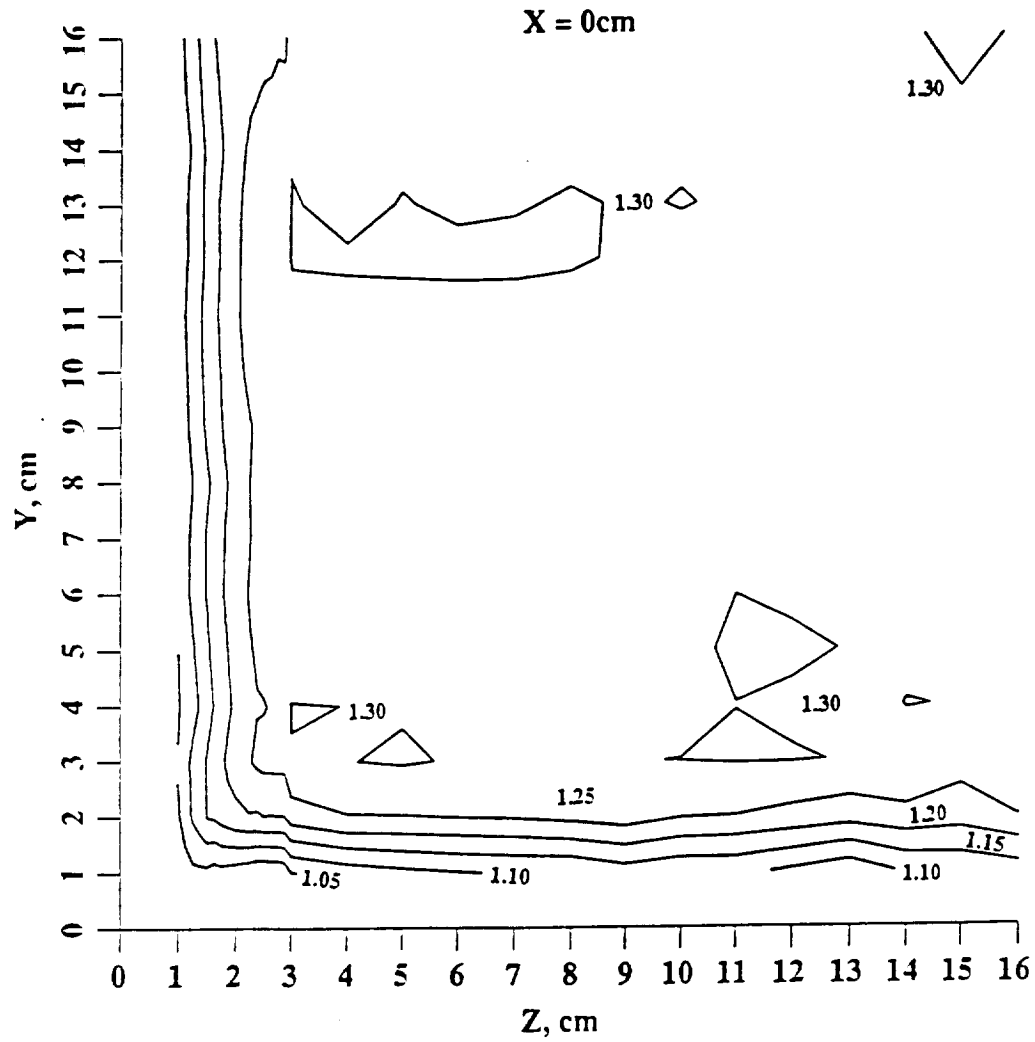
Figure 26: Cross Section Mach Contour Plot at X = 0; Mach 1.28.
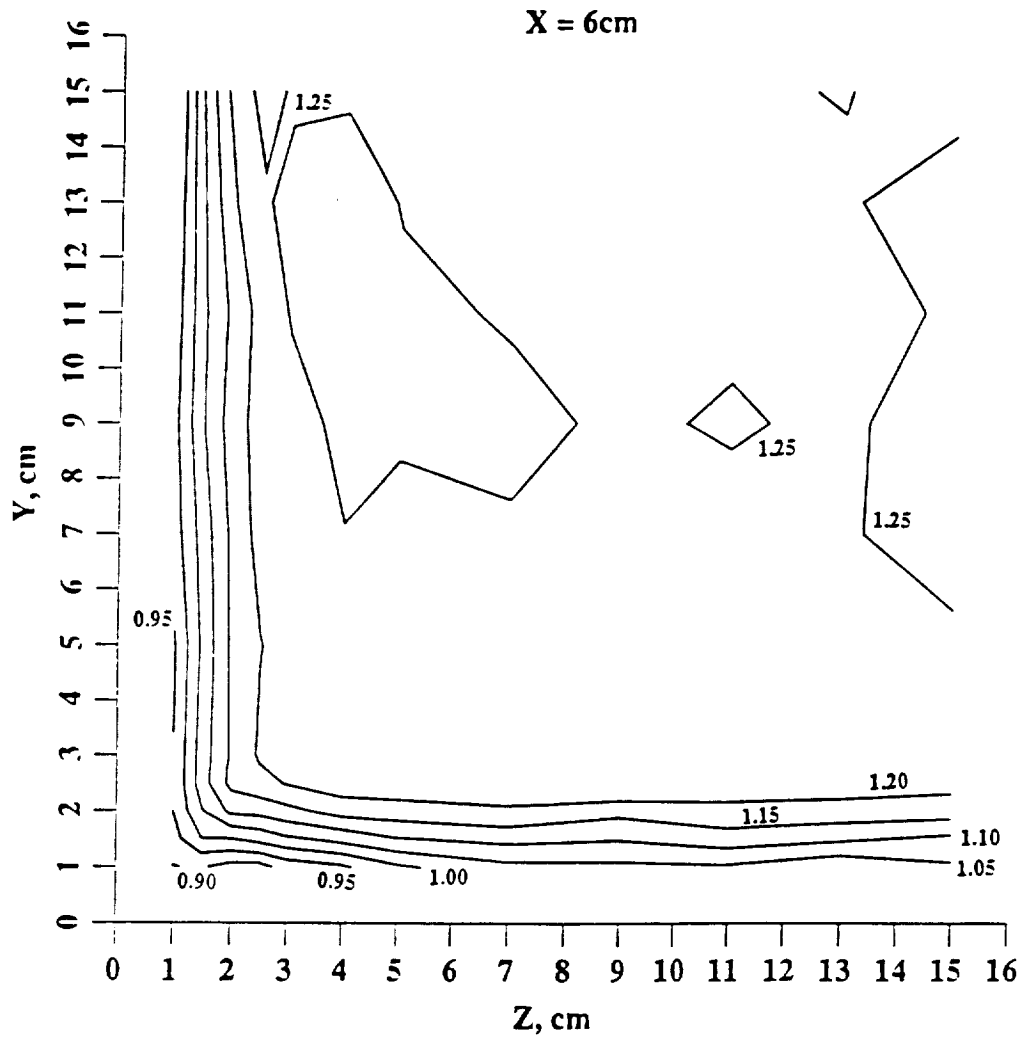
Figure 27: Cross Section Mach Contour Plot at X = 6 cm: Mach 1.28.
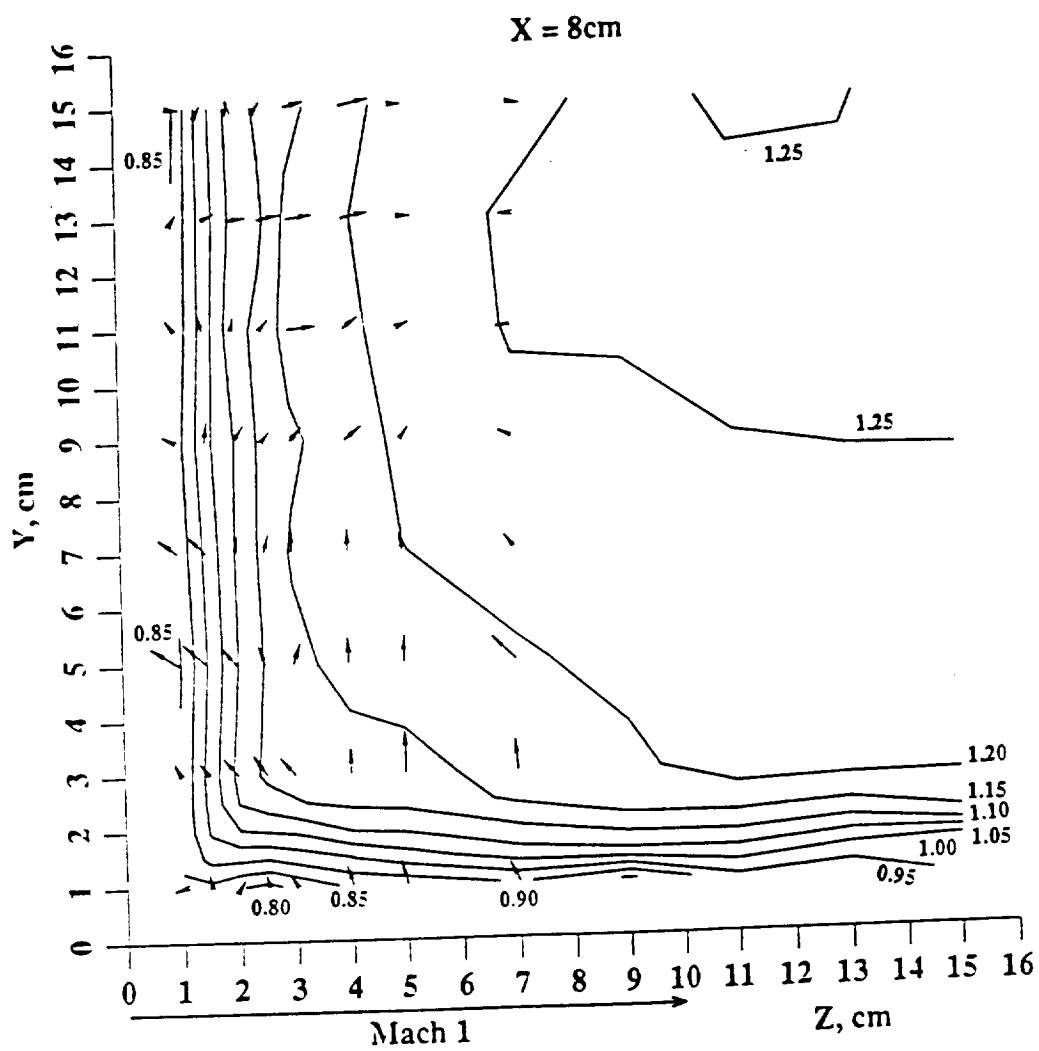
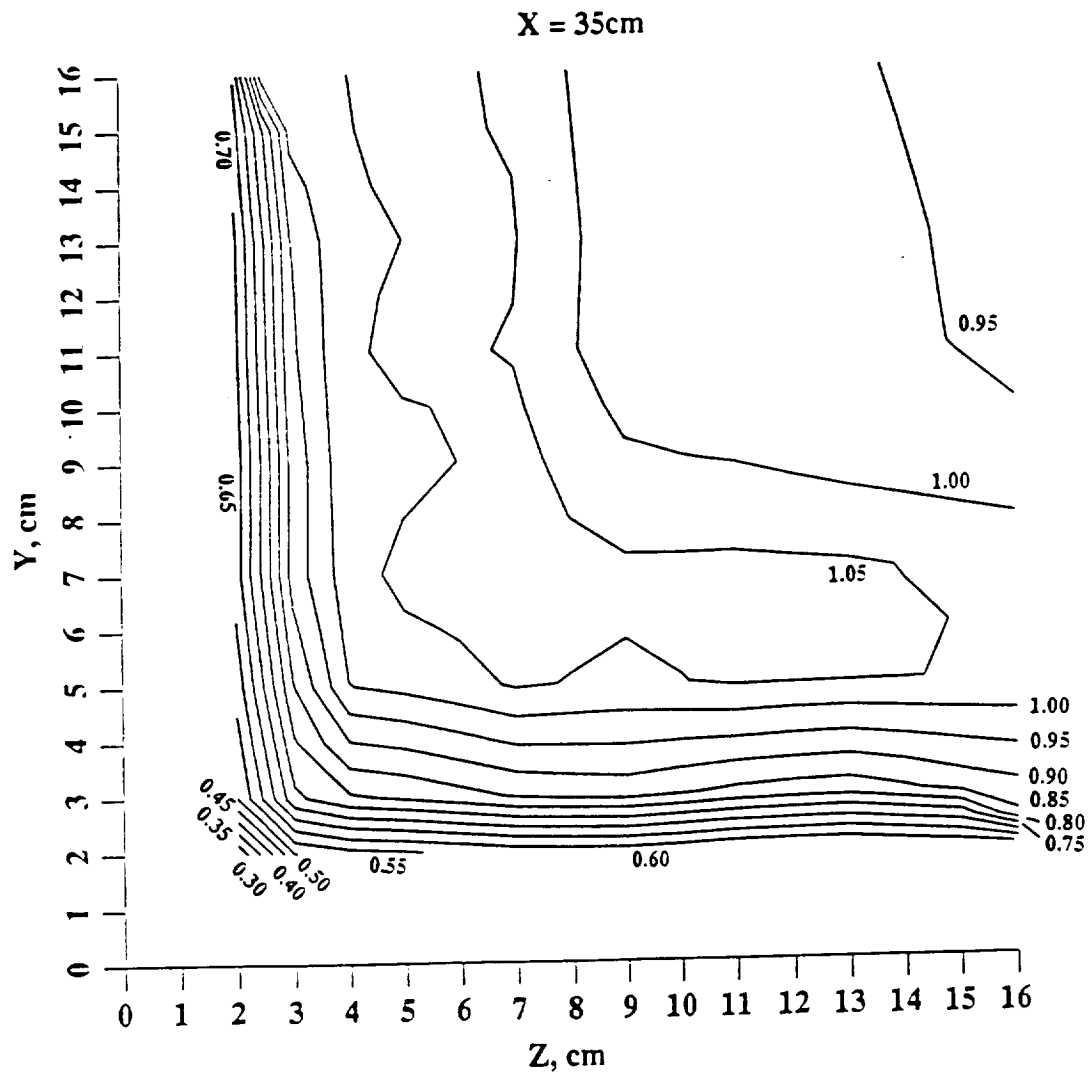Figure 28: Cross Section Mach Contour Plot at X = 8 cm; Mach 1.28.
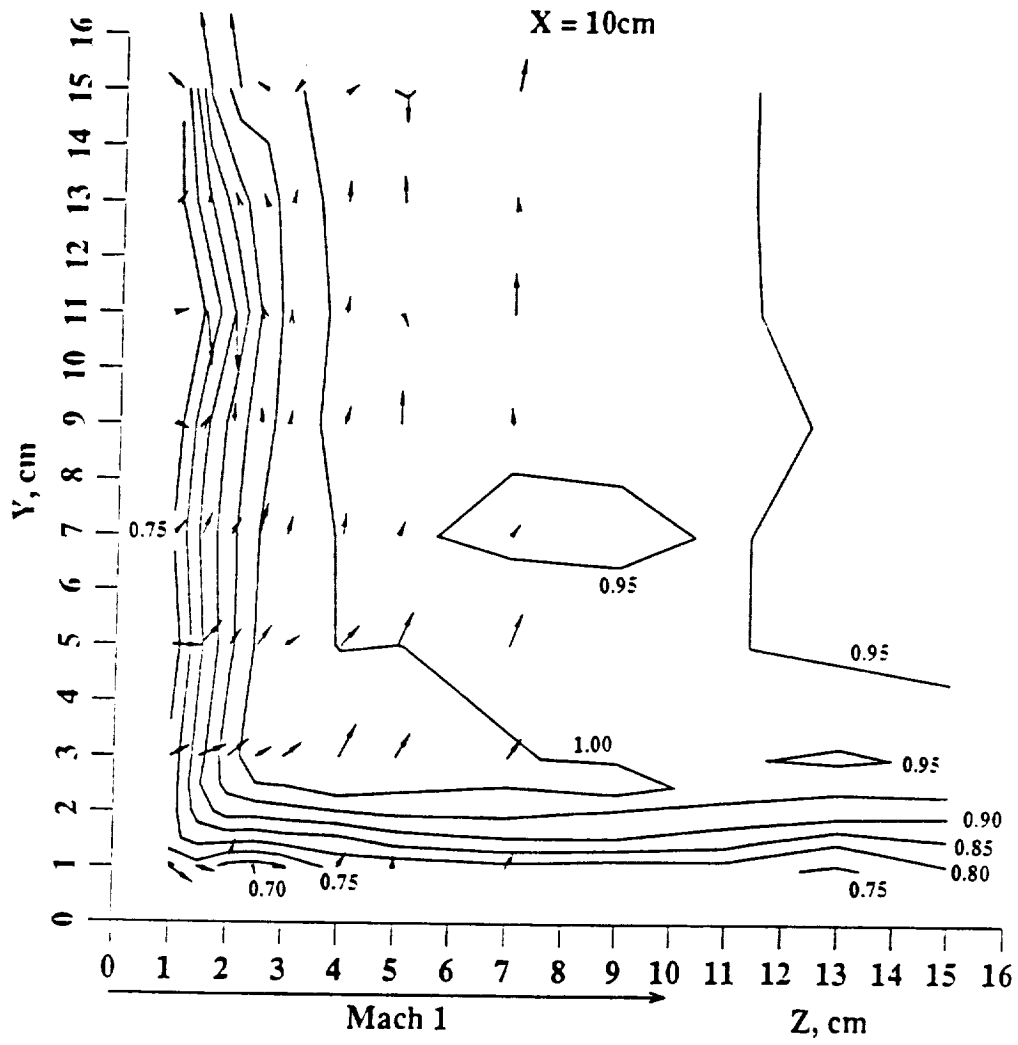
Figure 29: Cross Section Mach Contour Plot at X = 10 cm; Mach 1.28.
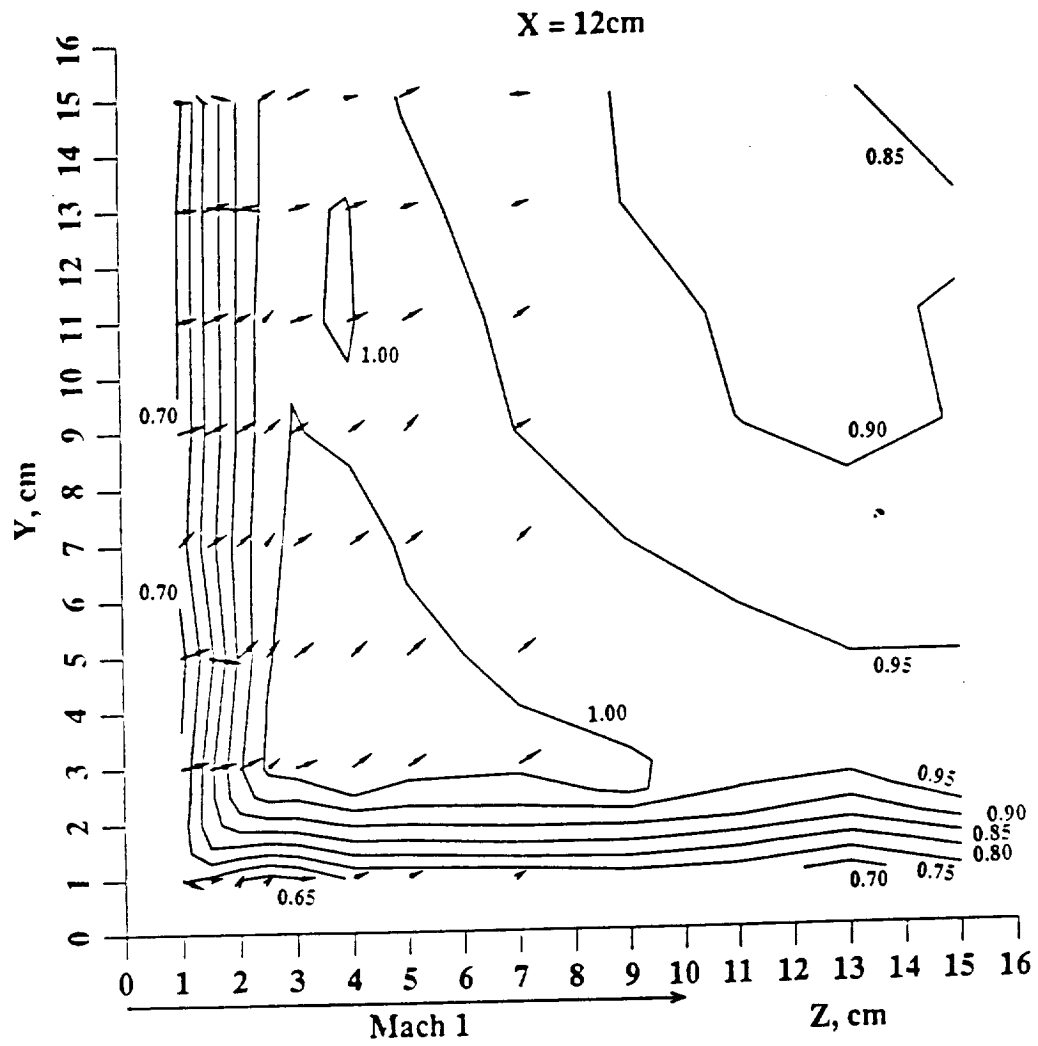
Figure 30: Cross Section Mach Contour Plot at X = 12 cm; Mach 1.28.
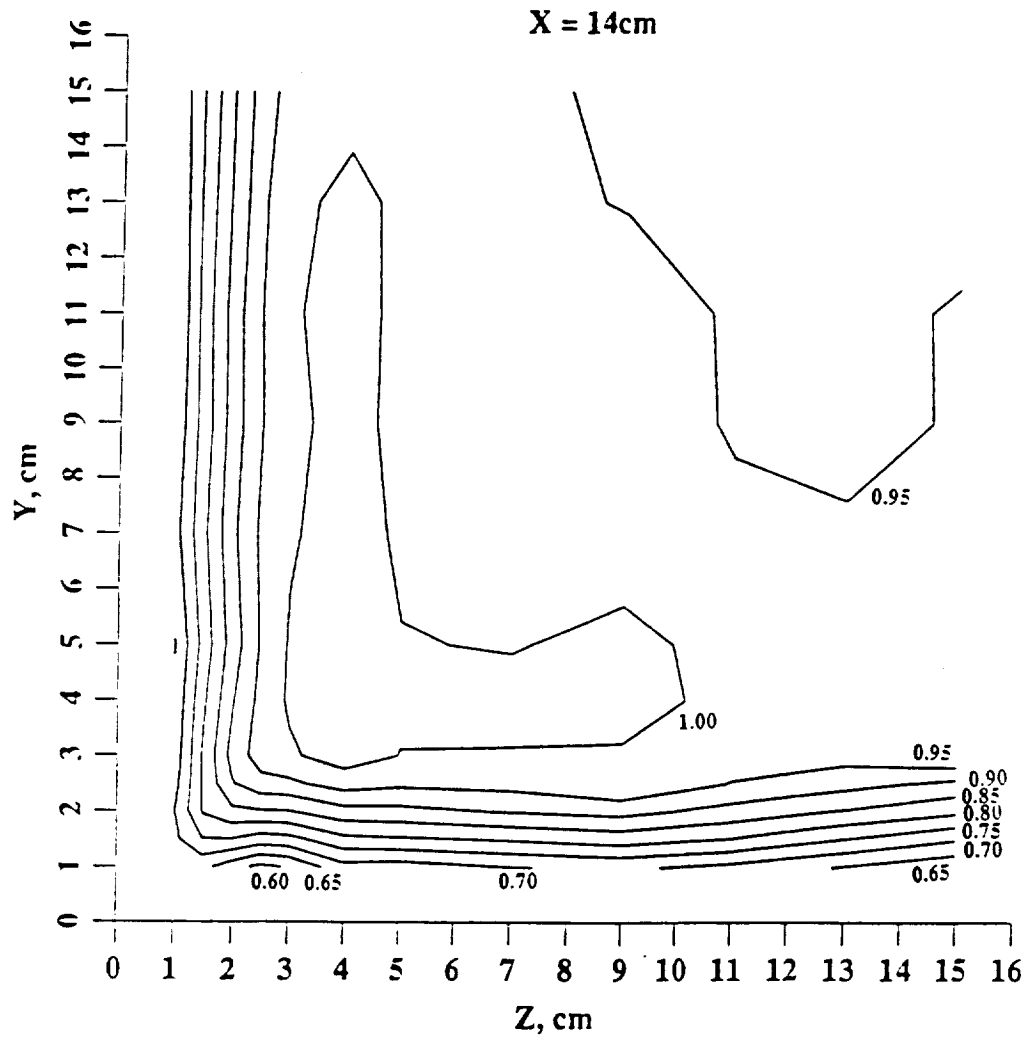
Figure 31: Cross Section Mach Contour Plot at $X = 14$ cm: Mach 1.28.
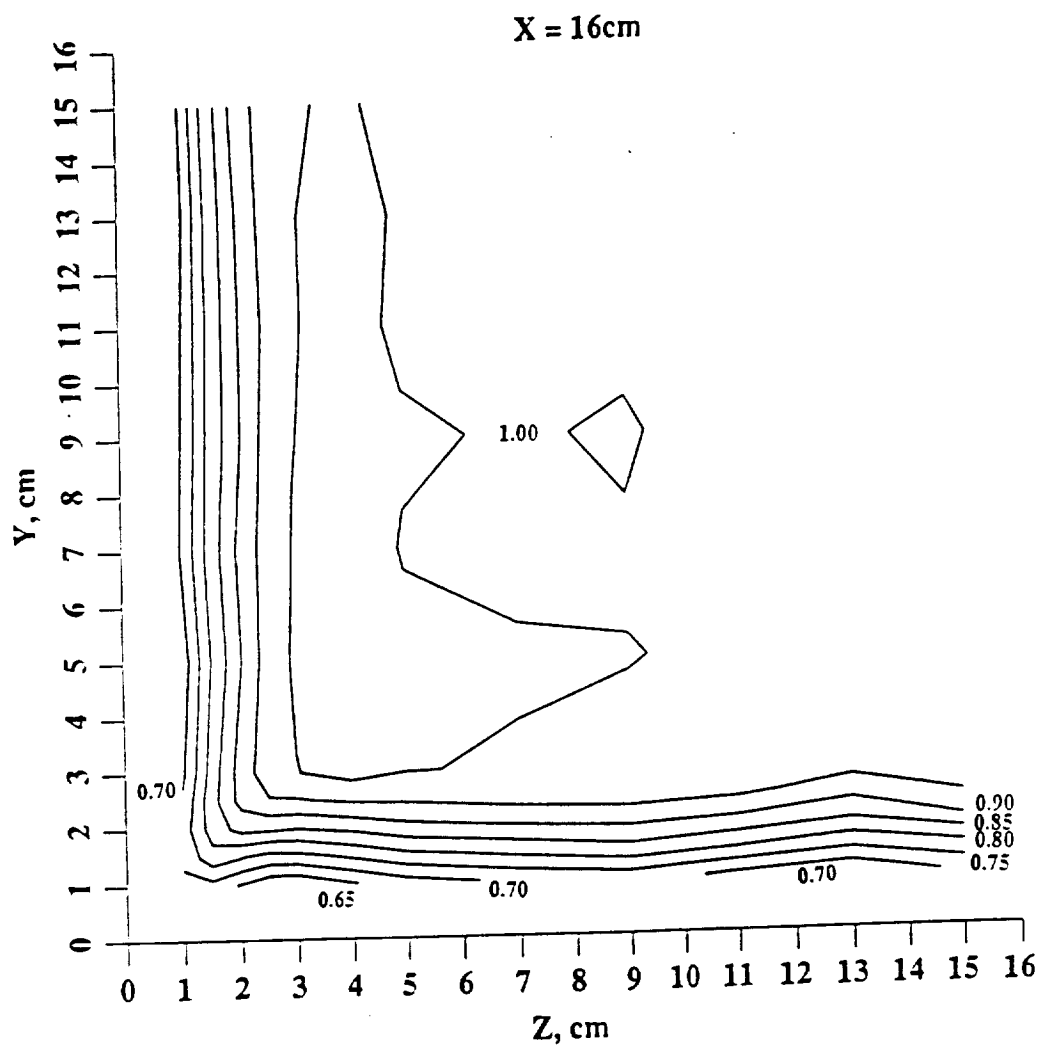
Figure 32: Cross Section Mach Contour Plot at X = 16 cm; Mach 1.28.
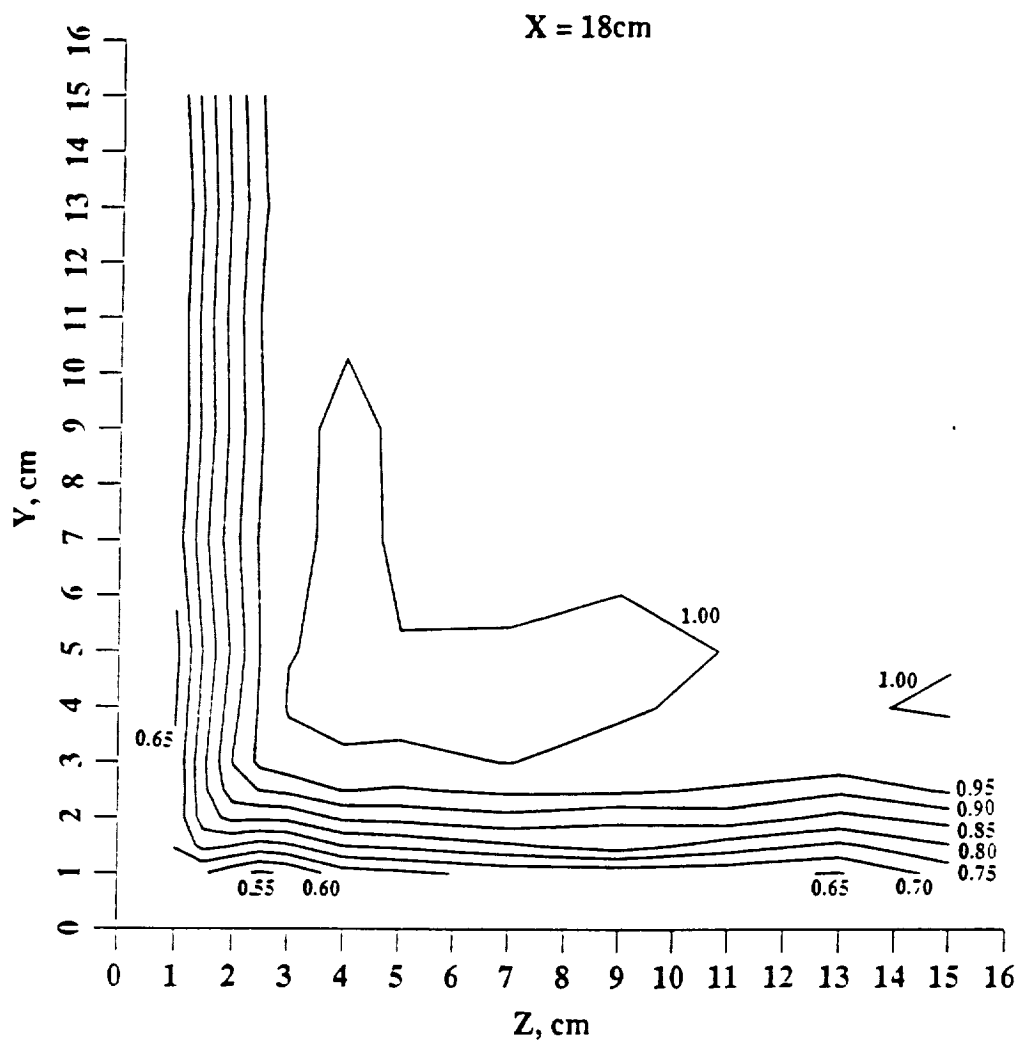
Figure 33: Cross Section Mach Contour Plot at X = 18 cm; Mach 1.28.
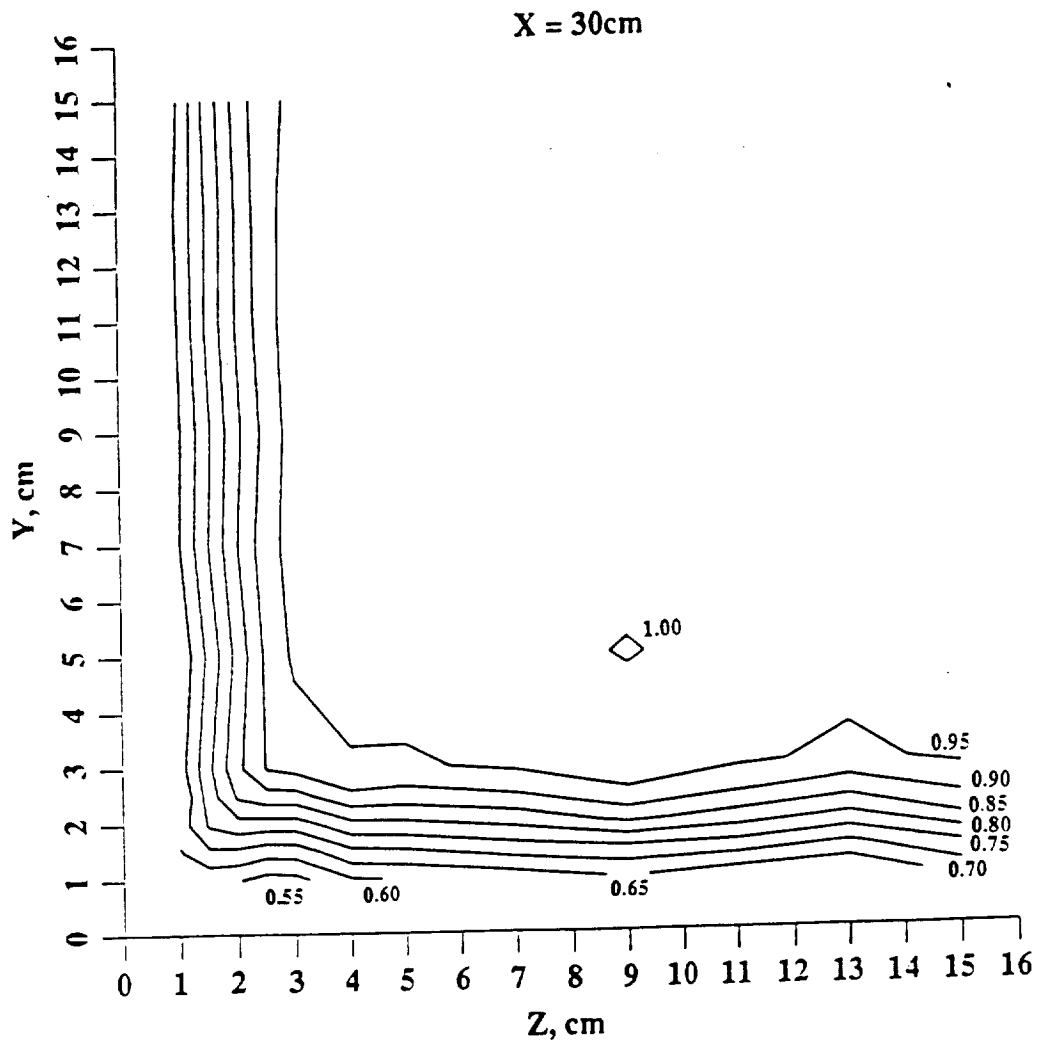
Figure 34: Cross Section Mach Contour Plot at X = 30 cm; Mach 1.28.
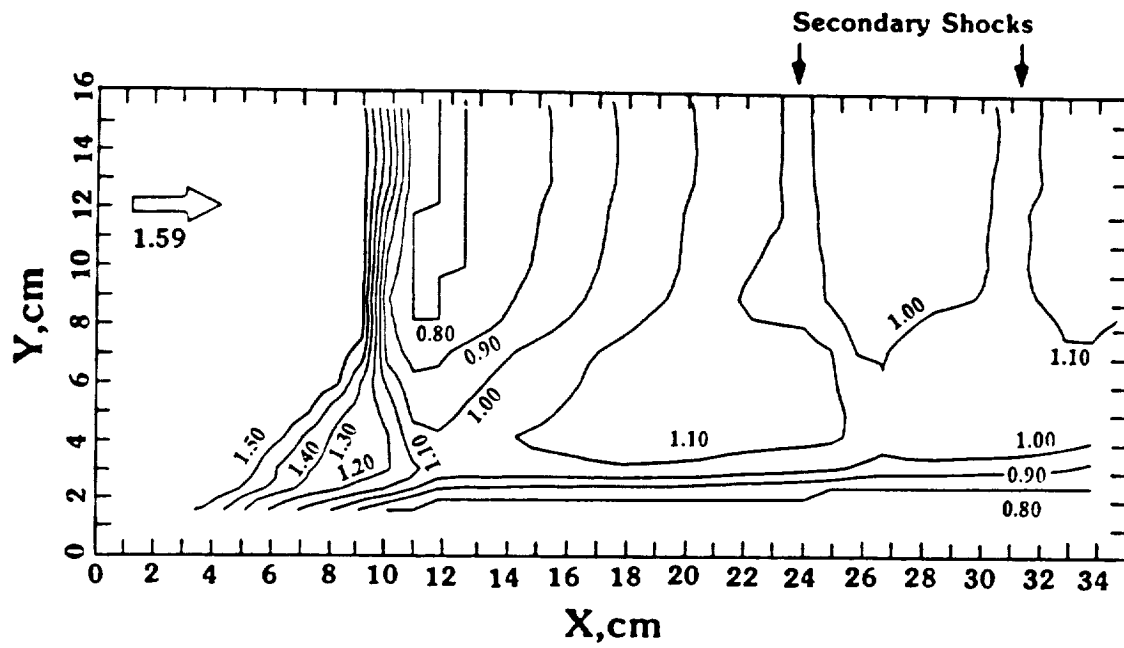
Figure 35: Mid-Span Mach Contour Plot; Mach 1.59.

Figure 36: Cross Section Mach Contour Plot at X = 0; Mach 1.59.
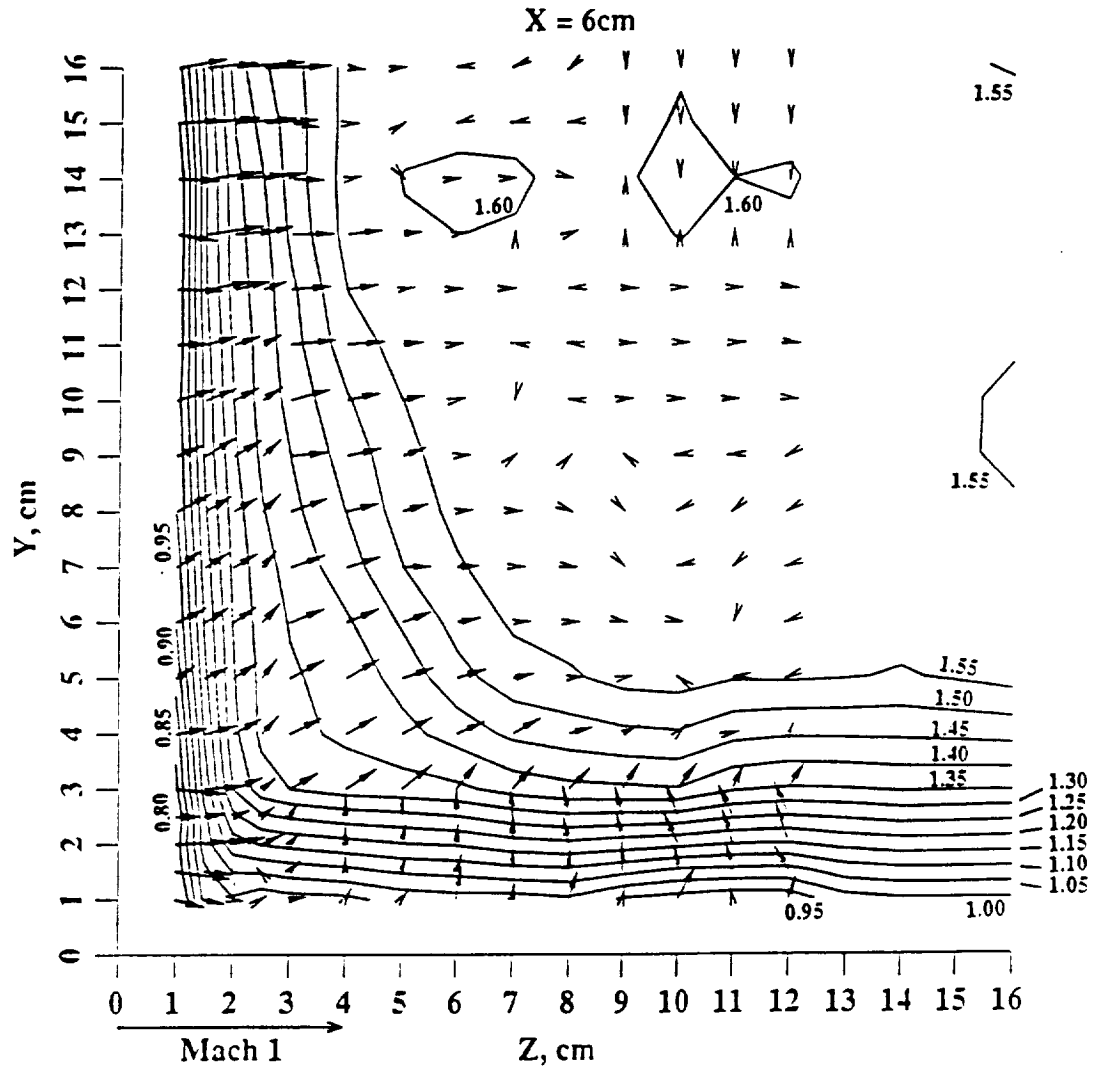
Figure 37: Cross Section Mach Contour Plot at X = 6 cm; Mach 1.59.
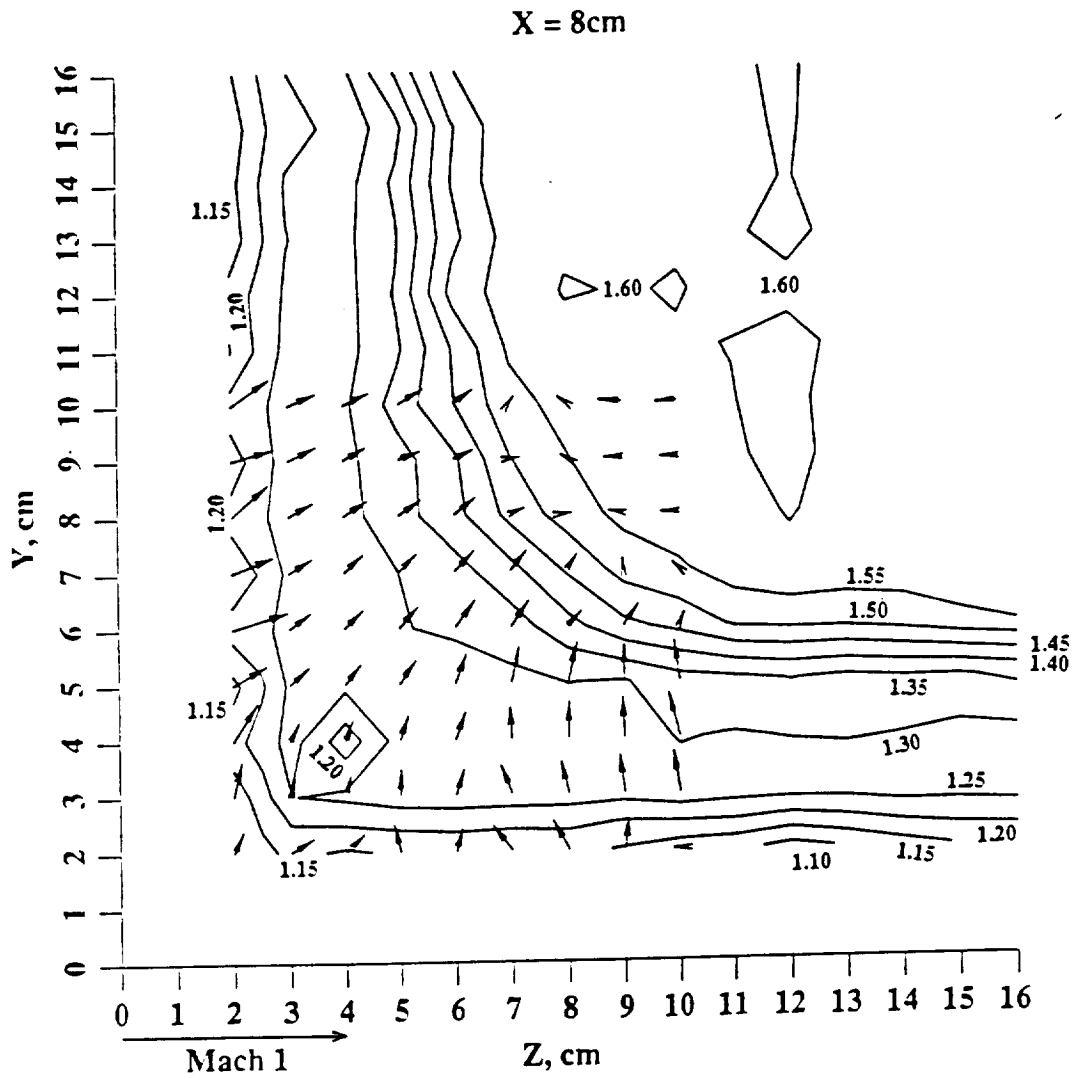
Figure 38: Cross Section Mach Contour Plot at X = 8 cm; Mach 1.59.
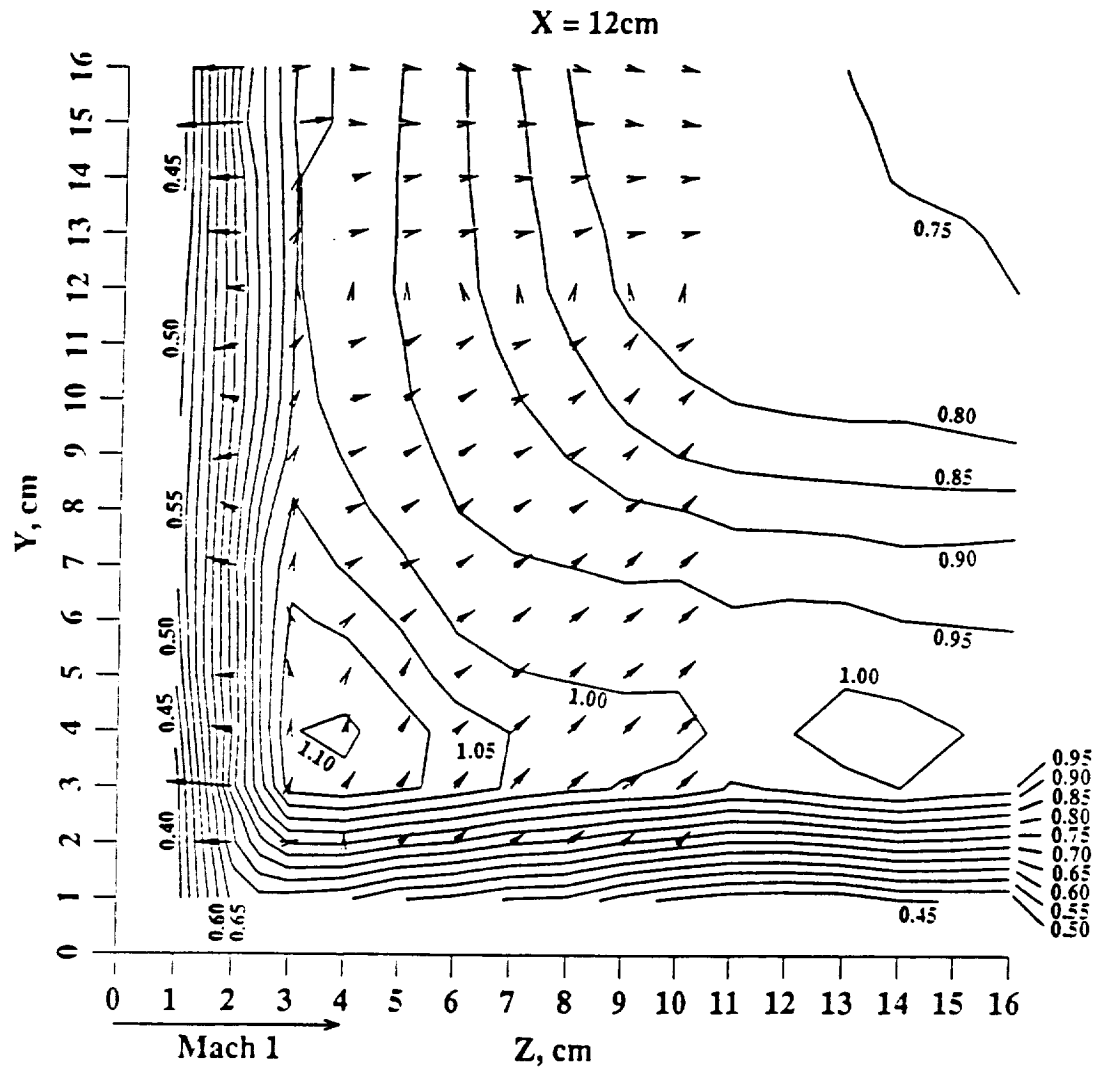
Figure 39: Cross Section Mach Contour Plot at X = 12 cm; Mach 1.59.
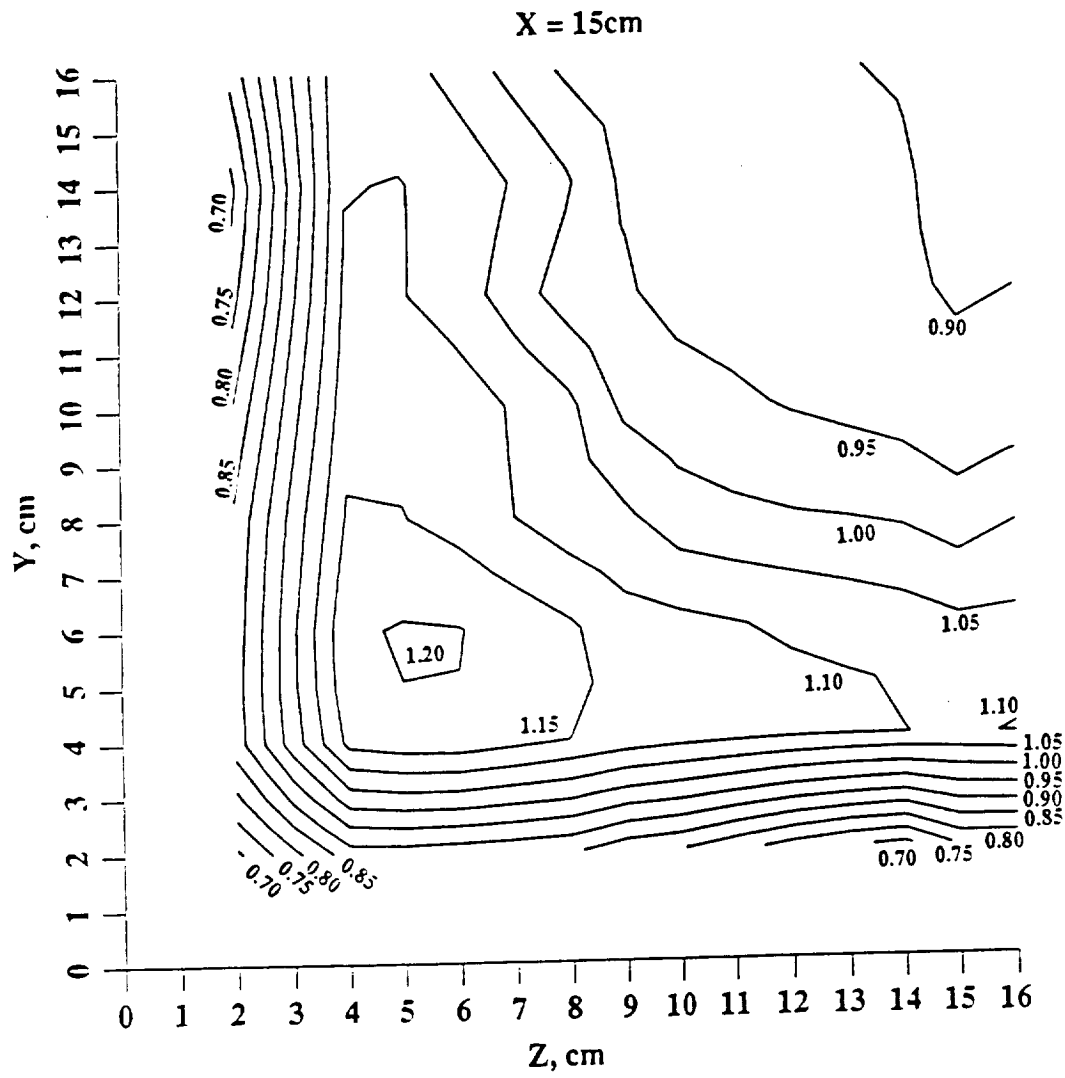
Figure 40: Cross Section Mach Contour Plot at X = 15 cm; Mach 1.59.
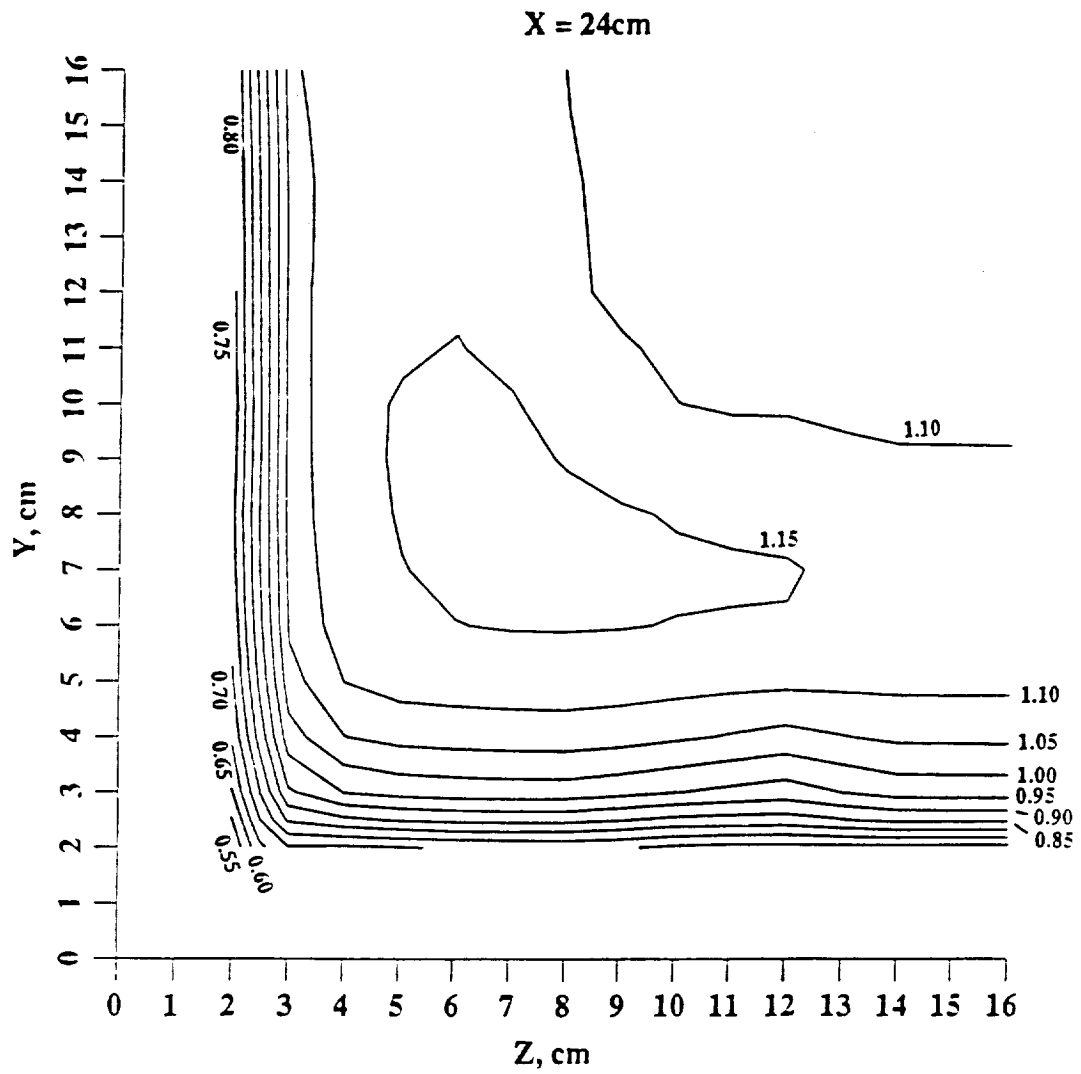
Figure 41: Cross Section Mach Contour Plot at X = 24 cm: Mach 1.59.
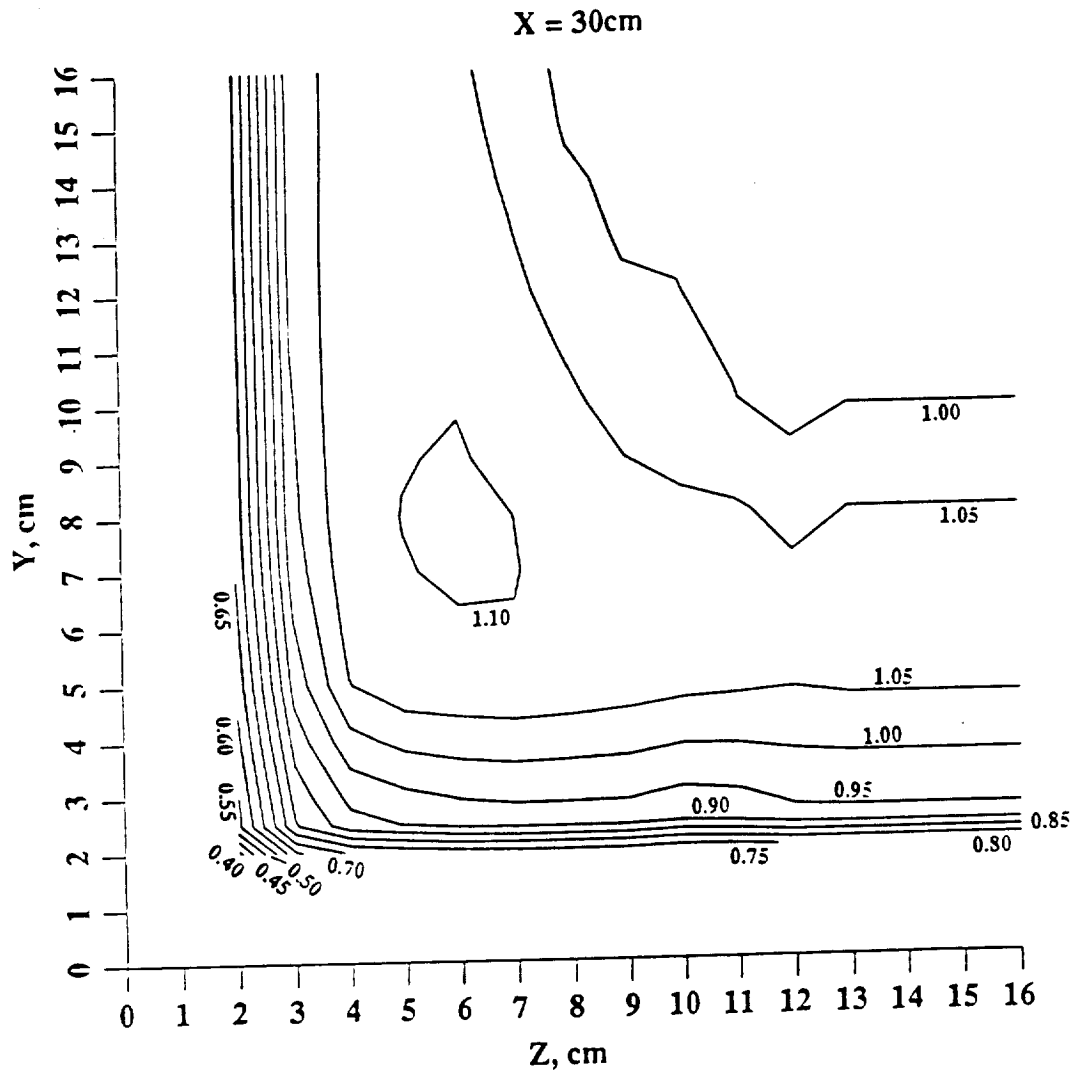
Figure 42: Cross Section Mach Contour Plot at X = 30 cm: Mach 1.59.
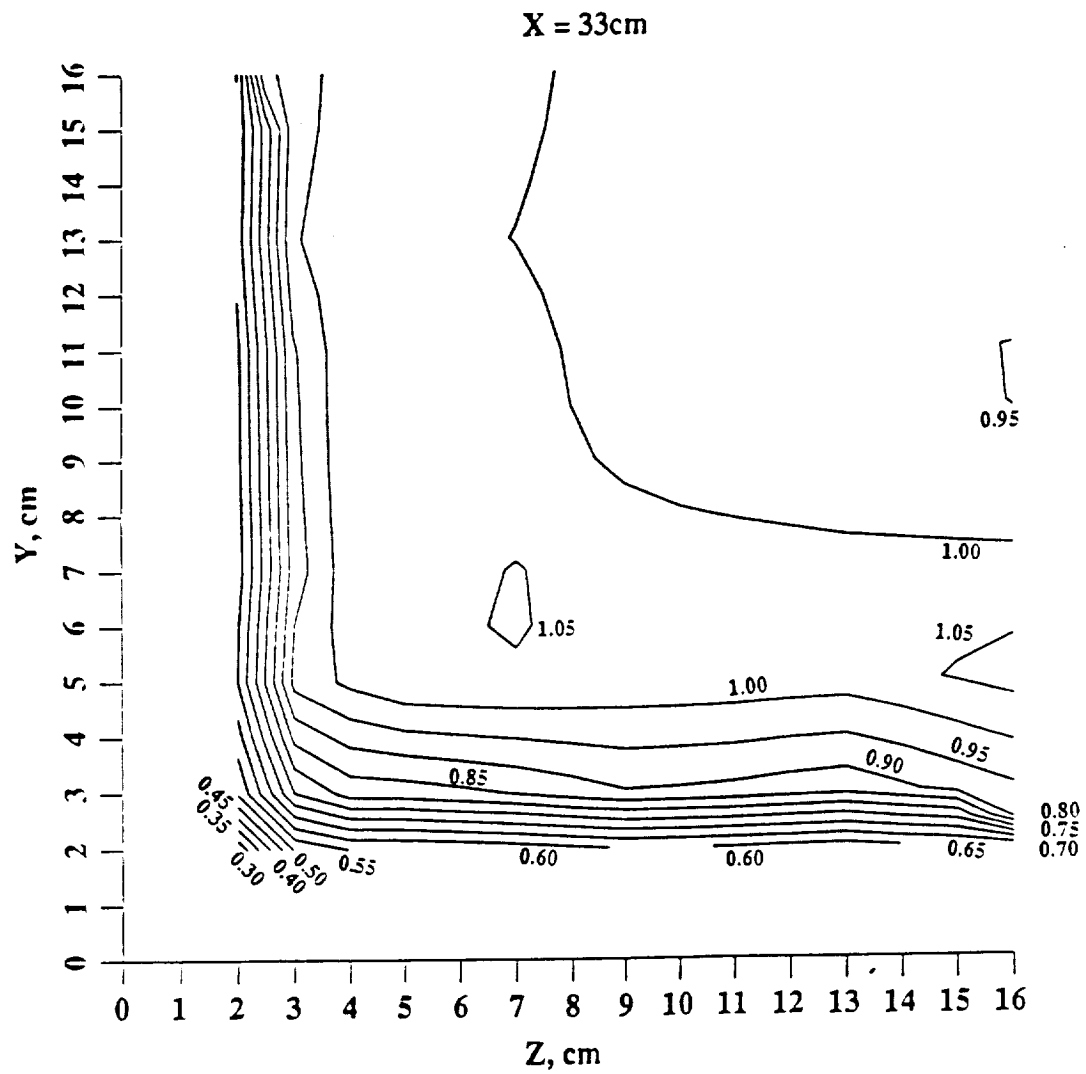
Figure 43: Cross Section Mach Contour Plot at X = 33 cm; Mach 1.59.

Figure 44: Cross Section Mach Contour Plot at X = 35 cm: Mach 1.59.
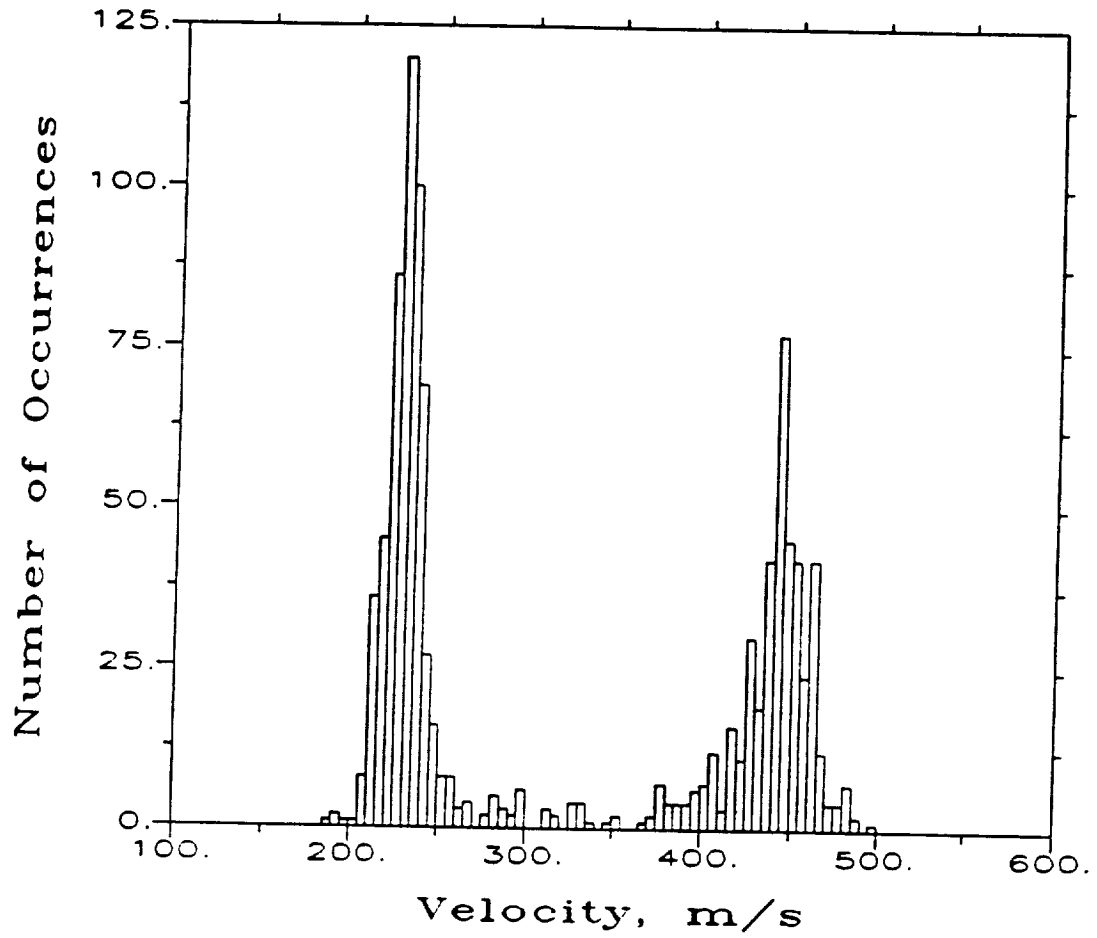
Figure 45: Histogram of LV Ensemble Near Shock Front, x = 9.6 cm, y = 15.0 cm, z = 14.0 cm; Mach 1.6.
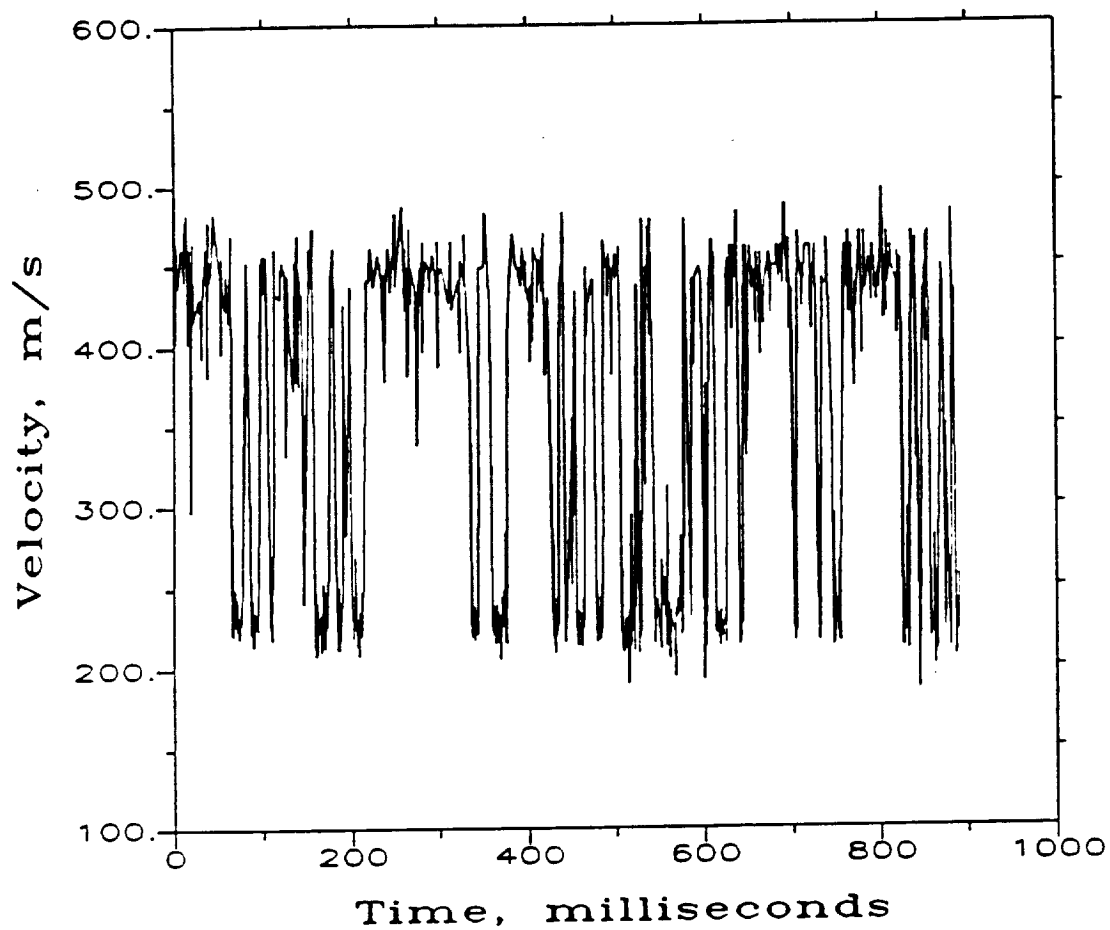
Figure 46: Time History of LV Ensemble Near Shock Front, x = 9.6 cm, y = 15.0 cm, z = 14.0 cm: Mach 1.6.
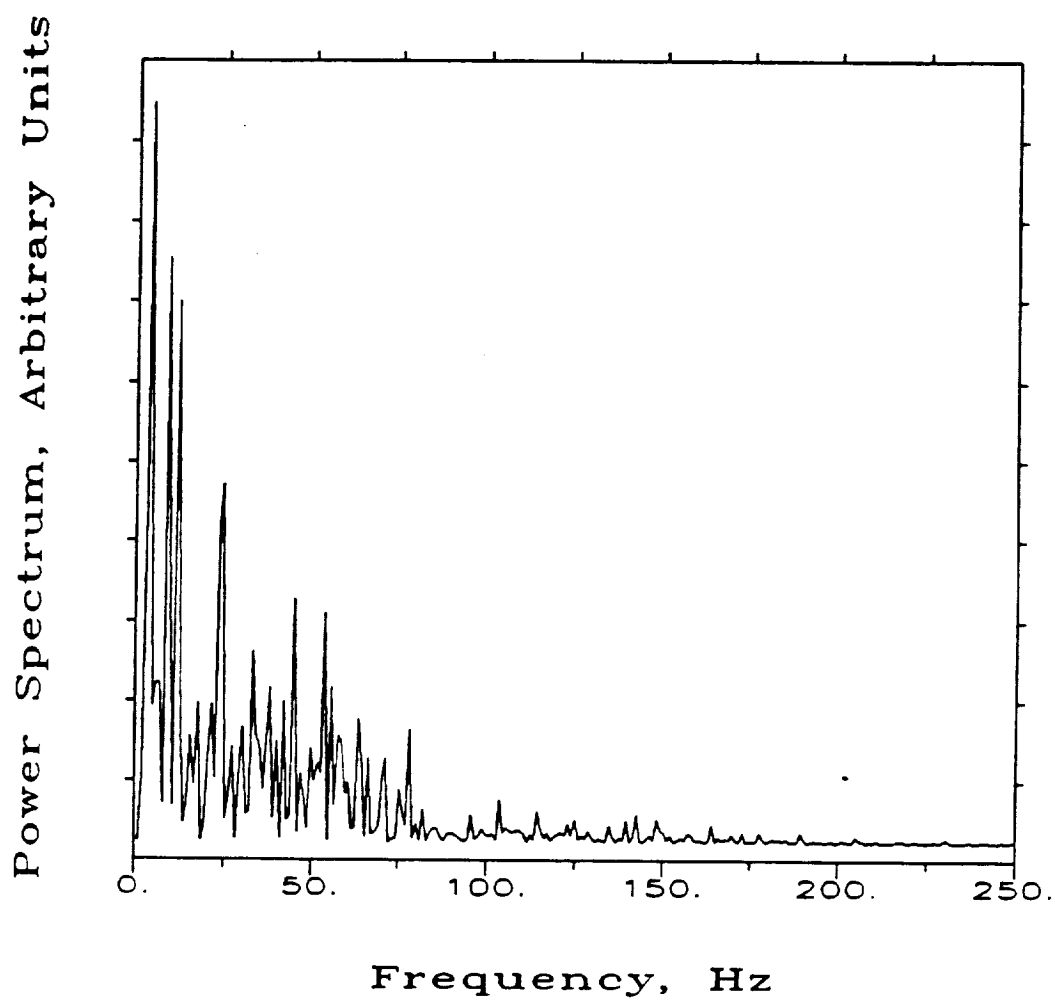
Figure 47: Spectral Analysis of LV Ensemble Near Shock Front, x = 9.6 cm, y = 15.0 cm, z = 14.0 cm: Mach 1.6.
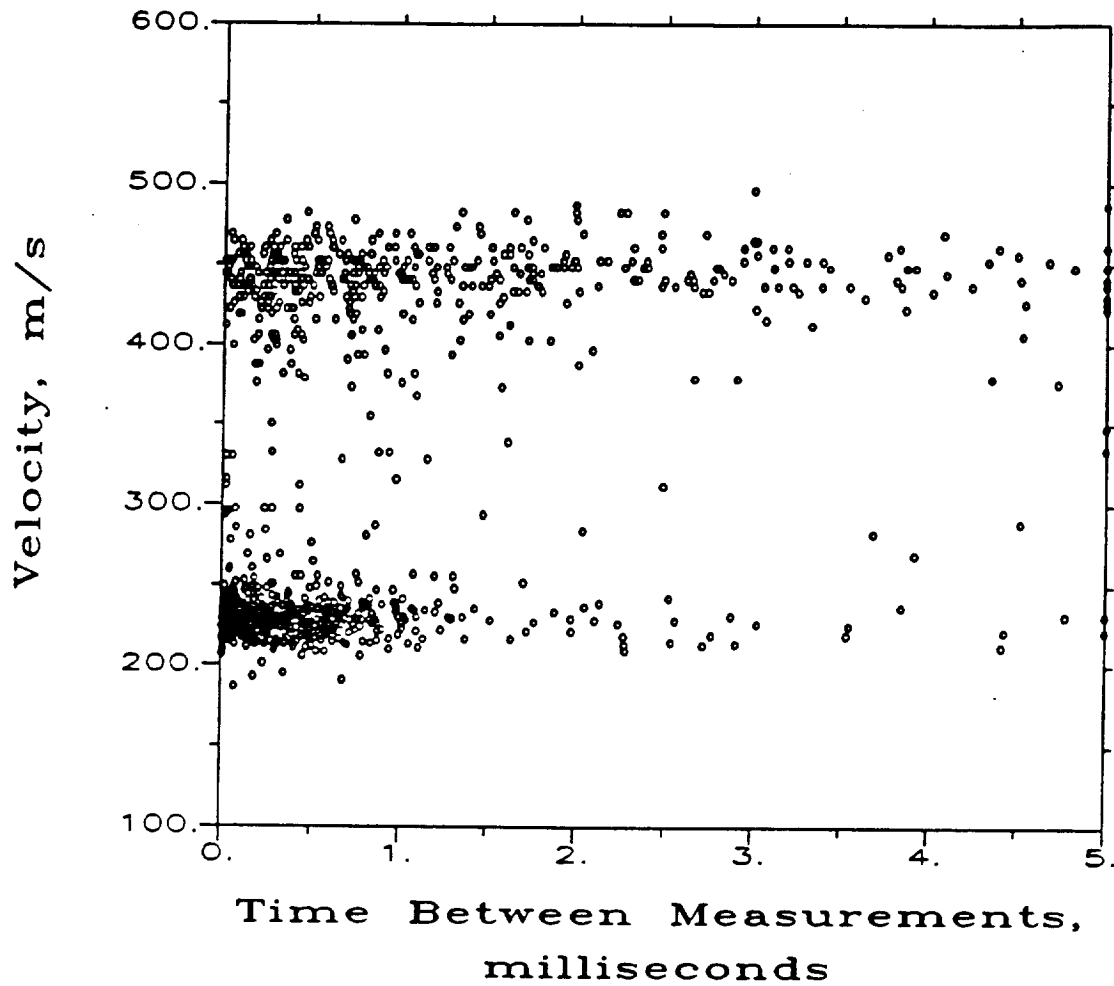
Figure 48: Time Between Realizations of LV Ensemble Near Shock Front, x = 9.6 cm, y = 15.0 cm, z = 14.0 cm: Mach 1.6.

REPORT DOCUMENTATION PAGE

1. AGENCY USE ONLY (Leave blank)	2. REPORT DATE	3. REPORT TYPE AND DATES COVERED
	September 1991	Technical Memorandum

4. TITLE AND SUBTITLE

A Laser Velocimeter Investigation of the Normal Shock-Wave Boundary Layer Interaction

5. FUNDING NUMBERS

WU - 505 - 62 - 52

6. AUTHOR(S)

Randall M. Chriss

7. PERFORMING ORGANIZATION NAME(S) AND ADDRESS(ES)

National Aeronautics and Space Administration
Lewis Research Center
Cleveland, Ohio 44135 - 3191

8. PERFORMING ORGANIZATION REPORT NUMBER

E - 6504

9. SPONSORING/MONITORING AGENCY NAMES(S) AND ADDRESS(ES)

National Aeronautics and Space Administration
Washington, D.C. 20546 - 0001

10. SPONSORING/MONITORING AGENCY REPORT NUMBER

NASA TM - 105201

11. SUPPLEMENTARY NOTES

12a. DISTRIBUTION/AVAILABILITY STATEMENT

Unclassified - Unlimited
Subject Category 34

12b. DISTRIBUTION CODE

13. ABSTRACT (Maximum 200 words)

Nonintrusive three-dimensional measurements have been made of a normal shock wave/turbulent boundary layer interaction. The measurements were made throughout a quadrant of a square test section of a continuous flow supersonic wind tunnel in which a normal shock wave had been stabilized. Two-dimensional measurements were made throughout the interaction region while three-dimensional measurements were made near the corner in the vicinity of the shock where three-dimensional flow effects were expected to be significant. Laser Doppler velocimetry, surface static pressure measurements and flow visualization techniques were employed for two freestream nominal Mach number test cases: 1.6 and 1.3. No turbulence information was obtained. The mean velocity measurements were converted to Mach number by recording the wind tunnel total temperature. Some shock oscillation was present during both of the test cases. After startup of the wind tunnel the shock oscillated with an amplitude of approximately ±1 cm, however, after reaching steady condition the shock oscillation amplitude was greatly reduced, as evidenced by the laser velocimeter results. The Mach 1.3 test case resulted in a nearly uniform flow without secondary shock waves and with no or very isolated corner separation. The Mach 1.6 test case contained separated flow regions and a system of secondary shock waves. The reported results are believed to accurately describe the flowfield of each case and may find use in the verification of numerical simulations.

14. SUBJECT TERMS

Normal shock wave; Laser velocimeter; Boundary layer

15. NUMBER OF PAGES
124

16. PRICE CODE
A06

17. SECURITY CLASSIFICATION OF REPORT	18. SECURITY CLASSIFICATION OF THIS PAGE	19. SECURITY CLASSIFICATION OF ABSTRACT	20. LIMITATION OF ABSTRACT
Unclassified	Unclassified	Unclassified	

National Aeronautics and
Space Administration

Lewis Research Center
Cleveland, Ohio 44135

FOURTH CLASS MAIL

ADDRESS CORRECTION REQUESTED

U.S.MAIL

NASA